Science Advances
AAAS

Supplementary Materials for

Leveraging data mining, active learning, and domain adaptation for efficient discovery of advanced oxygen evolution electrocatalysts

Rui Ding *et al.*

Corresponding author: Junhong Chen, junhongchen@uchicago.edu; Yuxin Chen, chenyuxin@uchicago.edu

Sci. Adv. **11**, eadr9038 (2025)
DOI: 10.1126/sciadv.adr9038

This PDF file includes:

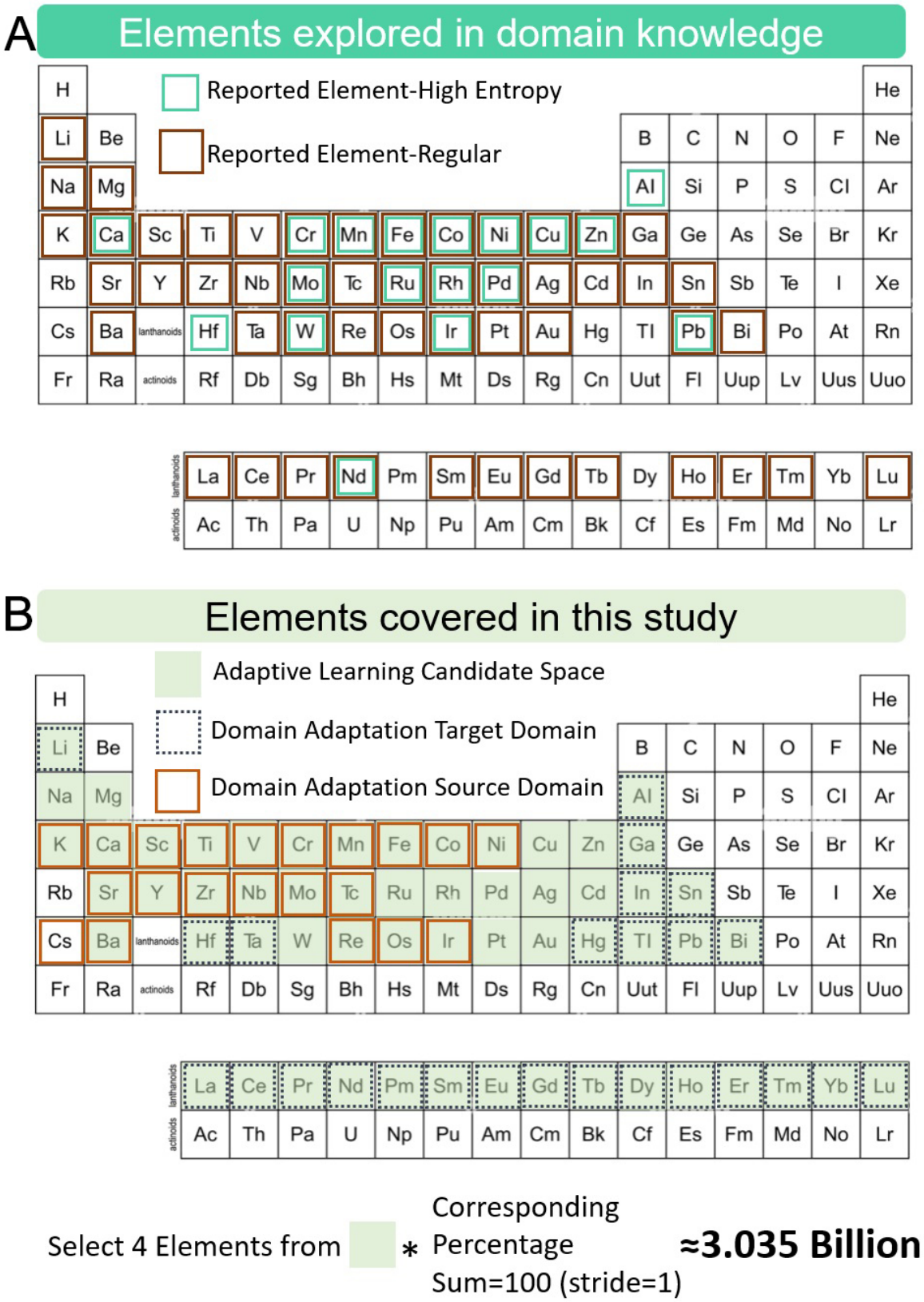

Fig. S1 Exploration of candidate metal element spaces for acidic OER electrocatalysts and corresponding combinatorial complexity. (A) The light blue highlighted elements represent

the metals involved in the precursor synthesis for acidic OER electrocatalysts in high-entropy or multi-metallic systems, as explored in recent publications (*18, 19, 111-120*) within the last two years. In these studies, the number of metal elements in the precursors would equal or exceed four. These studies typically do not investigate the elemental ratios, often defaulting to equimolar proportions in high-entropy systems. In contrast, the brown highlighted elements denote metals explored over the past 20 years in conventional research for acidic OER catalyst systems, used for doping or as base materials, as identified in the domain knowledge dataset used during the data-mining stage of this work (see **fig. S2**). In these studies, the metal element numbers in the precursors are predominantly lower than four, usually less than three. (B) The candidate metal element space explored in this study is highlighted in light green, representing the candidate elements involved in the DASH loop search within the active-learning module, expanded from the elements covered in the current domain as shown in (A) (including the remaining lanthanides and additions of Hg, Tl). The orange solid box highlights the candidate doping elements in the source domain for the domain adaptation module related to DFT theoretical simulations, while the blue dashed box outlines the corresponding target domain elements.

Note: To estimate the total number of combinations for designing a quaternary oxide with four elements selected from 58 possible elements and having their proportions sum up to 100% (with each proportion being an integer), the following steps were performed:

(1) Element Selection: Four elements are chosen from a pool of 58 candidates.

(2) Percentage Assignment: For each selected element, a percentage value is assigned between 1 and 100, inclusive, with a step size of 1.

(3) Constraint Application: The sum of the four percentage values must be equal to 100. This introduces a constraint on the percentage combinations, ensuring that the sum of the assigned percentages for the four elements equals 100.

(4) Duplication Removal: Duplicate combinations are removed to retain only unique combinations. This step ensures that permutations of the same combination are counted as one unique combination.

The result shows that the total possibilities would reach a huge number of 3.035 billion (3,034,803,310). This calculation encompasses both the distribution of percentages to the elements and the selection of the elements themselves. Corresponding script is available at the online repository's "./ML Databases and Scripts/Number of Possibilities Calculation" directory.

In conclusion, considering all possible combinations of the candidate metal elements highlighted in light green, assuming the sum of proportions equals 100% with a stride of 1%, the total possible formulations approach over three billion, even with only four precursor metals. This calculation excludes other synthesis parameters, such as annealing duration and temperature, post-treatment steps, and electrochemical factors, thus underscoring the "expansive array of constituent elements and synthesis parameters." If we further, consider synthesis parameters like what we have defined in the GA search part "/Machine Learning Databases and Script/Adaptive_Active Learning Loop&GA Prediction/Model Retraining and GA Prediction of Highest Variance and Lowest Overpotential (Weighted Committee Ensemble)" then there would be additional of 36*133*8 = 38,304 possibilities in synthesis parameters combination. Therefore, a total candidate space for our active learning stage with experimental exploitation and exploration is 116,245,105,986,240, which is over 116 trillion.

This vast candidate space highlights the complexity of optimizing such a system, necessitating a multi-stage strategy that employs various ML techniques for decision-making at different stages.

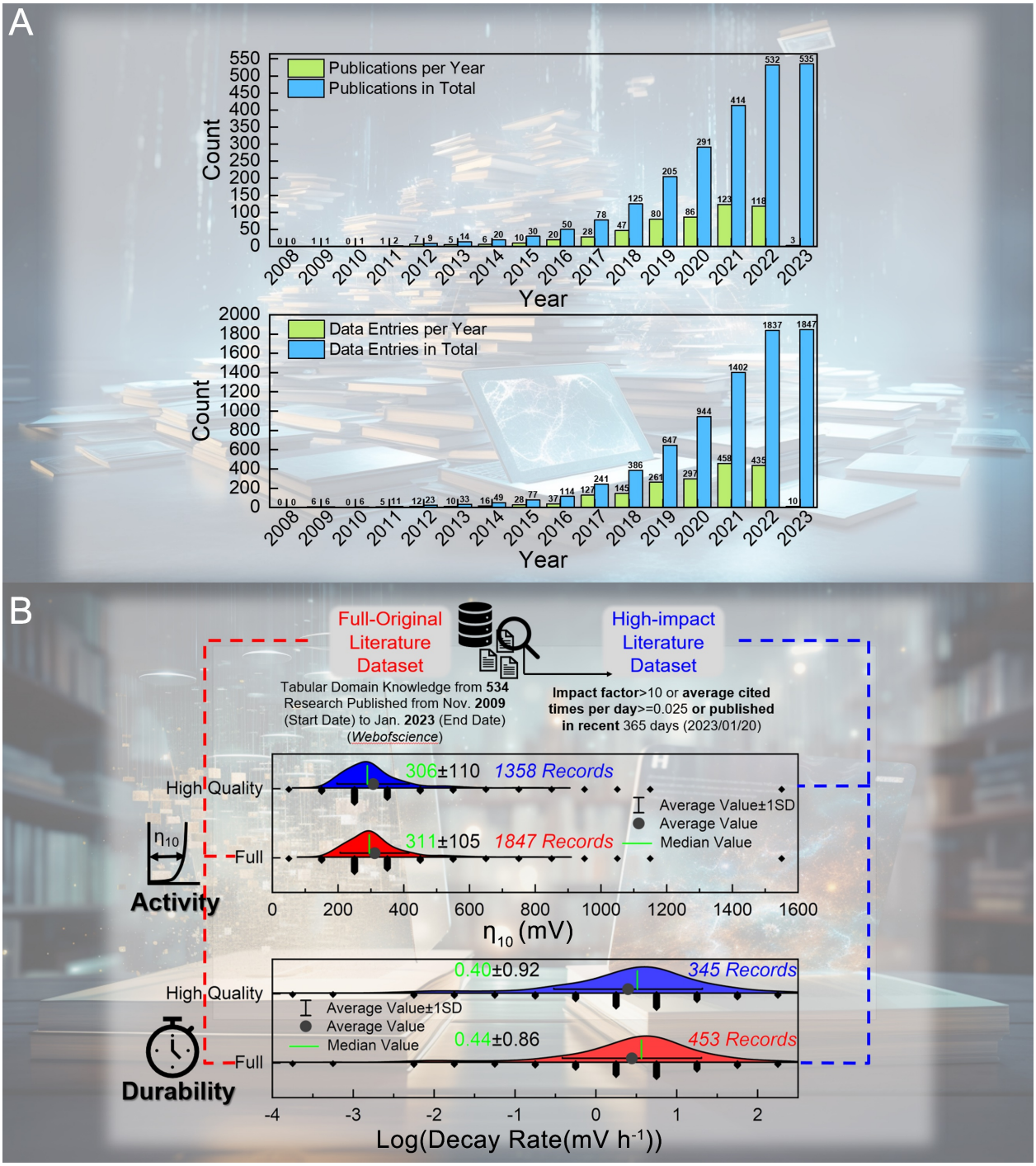

Fig. S2 Trends and distribution patterns in the domain knowledge datasets for acidic OER electrocatalysts. (A) Publication and data entries (number per year vs. total) in the full initial domain knowledge dataset. (B) Half-violin plots that reflect the distribution patterns of the domain knowledge datasets.

Table S1 The features in the domain knowledge dataset (full dataset, 1,847 entries) for catalytic activity and corresponding variable range.

Feature Name (Unit)	Variable Range
Metal_Dopant_1[a]（1~4 represent the proportion in precursor from high to low）	49 different metal elements[a,b]
Metal_Dopant_2	55 different metal elements or none
Metal_Dopant_3	39 different metal elements or none
Metal_Dopant_4	7 different metal elements or none
Metal_Dopant_1 Proportion in Precursor（at. %; refers to that in total of four types of metal）	28.57~100
Metal_Dopant_2 Proportion in Precursor（at. %）	0~50
Metal_Dopant_3 Proportion in Precursor（at. %）	0~33.33
Metal_Dopant_4 Proportion in Precursor（at. %）	0~17.67
Hydrothermal Temperature (℃) (or precursor mixing)	-196~320
Hydrothermal Time (min) (or precursor mixing)	0 ~86,400
Hydrothermal Still/Stirring (0/1) (or precursor mixing)	0: still incubation; 1: stirring or sonication
Hydrothermal Strong Reductant in Liquid (0/1) (or precursor mixing)	0: False; 1: True
Hydrothermal Weak Reductant in Liquid (0/1) (or precursor mixing)	0: False; 1: True
Mixed in Solid or Liquid (0/1)	0: False (liquid mixing or hydrothermal); 1: True (ball milling)
Annealing Temperature (℃)	25~1,400
Annealing Time (min)	0~20,160
Annealing Still/Stirring (0/1)	0: False; 1: True
Annealing Atmosphere Inert (0/1)	0: False; 1: True
Annealing Atmosphere Reducing (0/1)	0: False; 1: True
Post-processing Acid Wash, etc. (after annealing; 0/1)	0: False; 1: True
Catalyst Loading (mg cm^{-2})	0.000714~490
Support Material Loading (mg cm^{-2})	0~18
Support Material is Not Carbon (support material, TiO_x, etc.; 0/1)	0: False; 1: True
Electrode Type_Glassy Carbon/Carbon Paper or Ti Mesh (0/1)	0: Glassy Carbon;1: Carbon Paper or Ti Mesh
LSV Scanning Speed (mV s^{-1})	0.1~100
Electrolyte Proton Concentration (M)	0.01~6

Note:
a) For clarity and consistency in terminology, all metal elements in the precursor are referred to as “dopants”, even though the first “dopant” is actually the primary metal. These are arranged in descending order of their proportions, from the first to the fourth.
b) When conducting non-ML method data mining, the dataset directly treats elements as frequent items. However, for ML modeling and fitting, the elemental information is digitized and represented by properties such as relative atomic mass, atomic number, period, group, ionization energy, electronegativity, number of outermost d electrons, and atomic radius, as we have illustrated in detail in **Supplementary Note 1**, **Fig. SN 1-1**.
c) Additionally, in some studies, such as those using TiN or TiC as catalyst supports, the elements N and C do not exist in the final mixed oxide product in the same way as they do in the precursor organic compounds. Therefore, despite the term “metal elements” used in this paper, a few records in the dataset will include N and C. This is in consideration of their stable presence during the catalytic process and to account for their potential synergistic effects in catalysis.

Table S2 The features in the domain knowledge dataset (full dataset, 453 entries) for stability and corresponding variable range.

Feature Name (Unit)	Variable Range
Metal_Dopant_1（1~4 represent the proportion in precursor from high to low）	41 different metal elements
Metal_Dopant_2	53 different metal elements or none
Metal_Dopant_3	32 different metal elements or none
Metal_Dopant_4	3 different metal elements or none
Metal_Dopant_1 Proportion in Precursor（at. %; refers to that in total four types of metal）	28.57~100
Metal_Dopant_2 Proportion in Precursor（at. %）	0~50
Metal_Dopant_3 Proportion in Precursor（at. %）	0~32.34
Metal_Dopant_4 Proportion in Precursor（at. %）	0~2.06
Hydrothermal Temperature (℃) (or precursor mixing)	-77~320
Hydrothermal Time (min) (or precursor mixing)	0 ~10,080
Hydrothermal Still/Stirring (0/1) (or precursor mixing)	0: still incubation; 1: stirring or sonication
Hydrothermal Strong Reductant in Liquid (0/1) (or precursor mixing)	0: False; 1: True
Hydrothermal Weak Reductant in Liquid (0/1) (or precursor mixing)	0: False; 1: True
Mixed in Solid or Liquid (0/1)	0: False (liquid mixing or hydrothermal); 1: True (ball milling)
Annealing Temperature (℃)	25~1,200
Annealing Time (min)	0~20160
Annealing Still/Stirring (0/1)	0: False; 1: True
Annealing Atmosphere Inert (0/1)	0: False; 1: True
Annealing Atmosphere Reducing (0/1)	0: False; 1: True
Post-processing Acid Wash, etc. (after annealing; 0/1)	0: False; 1: True
Catalyst Loading (mg cm^{-2})	0.000714~490
Support Material Loading (mg cm^{-2})	0~5.58
Support Material is Not Carbon (support material, TiO_x etc.; 0/1)	0: False; 1: True
Electrode Type_Glassy Carbon/Carbon Paper or Ti Mesh (0/1)	0: Glassy Carbon;1: Carbon Paper or Ti Mesh
Electrolyte Proton Concentration (M)	0.01~6
Stability Constant Current Density (mA cm^{-2})	0.1~1,000
Stability Test Time (h)	0.28~8,000

Note:
After integrating the fundamental intrinsic atomic properties information into the dataset, we further examined the correlation matrices for the initial dataset using the Kendall, Spearman, and Pearson methods. Interested readers can check the corresponding results in the online GitHub repository (https://github.com/ruiding-uchicago/DASH) ("/Online Repository Figures/"): Fig. OR1~OR12. While there is a high degree of inter-correlation among features that inevitably express fundamental intrinsic atomic properties information of elements, such as relative atomic mass, atomic number, period, group, ionization potential, electronegativity, number of d electrons, and atomic radius, the correlations are significantly lower among other features. Specifically, this lower correlation is observed both within features related to material synthesis and testing and between these features and the fundamental intrinsic atomic properties of elements (except for a reasonable correlation between annealing time and temperature). This finding is particularly encouraging for several reasons. First, the lower degree of correlation among these sets of features suggests a diverse and rich dataset, which is crucial for the robustness of ML models. This correlation indicates that our dataset encompasses a wide range of independent variables, thus enhancing the potential for our models to capture and learn from a broad spectrum of material behaviors and properties. Second, the low correlation between material synthesis/testing features and elemental fundamental intrinsic atomic properties implies that our dataset is not dominated by any single type of information. This diversity ensures that our ML models are not biased towards fundamental intrinsic atomic properties features alone but are also informed by practical, experimental data. In summary, this characteristic of our dataset is advantageous for developing nuanced and comprehensive ML models, as it allows for the exploration of complex interactions within materials, potentially leading to novel insights and breakthroughs in the field of electrocatalysis.
The corresponding unprocessed domain knowledge dataset .csv file (that is readable in Excel software), Python script files, and generated pkl dataset files (for supervised learning and training first-iteration ML committees based on the previously mentioned domain knowledge dataset) are stored and publicly available in the: "/ML Databases and Scripts/Domain Knowledge Database Preprocessing" directory of the DASH online repository.
More secondary implementation details and discussions are available in **Supplementary Note 1**.

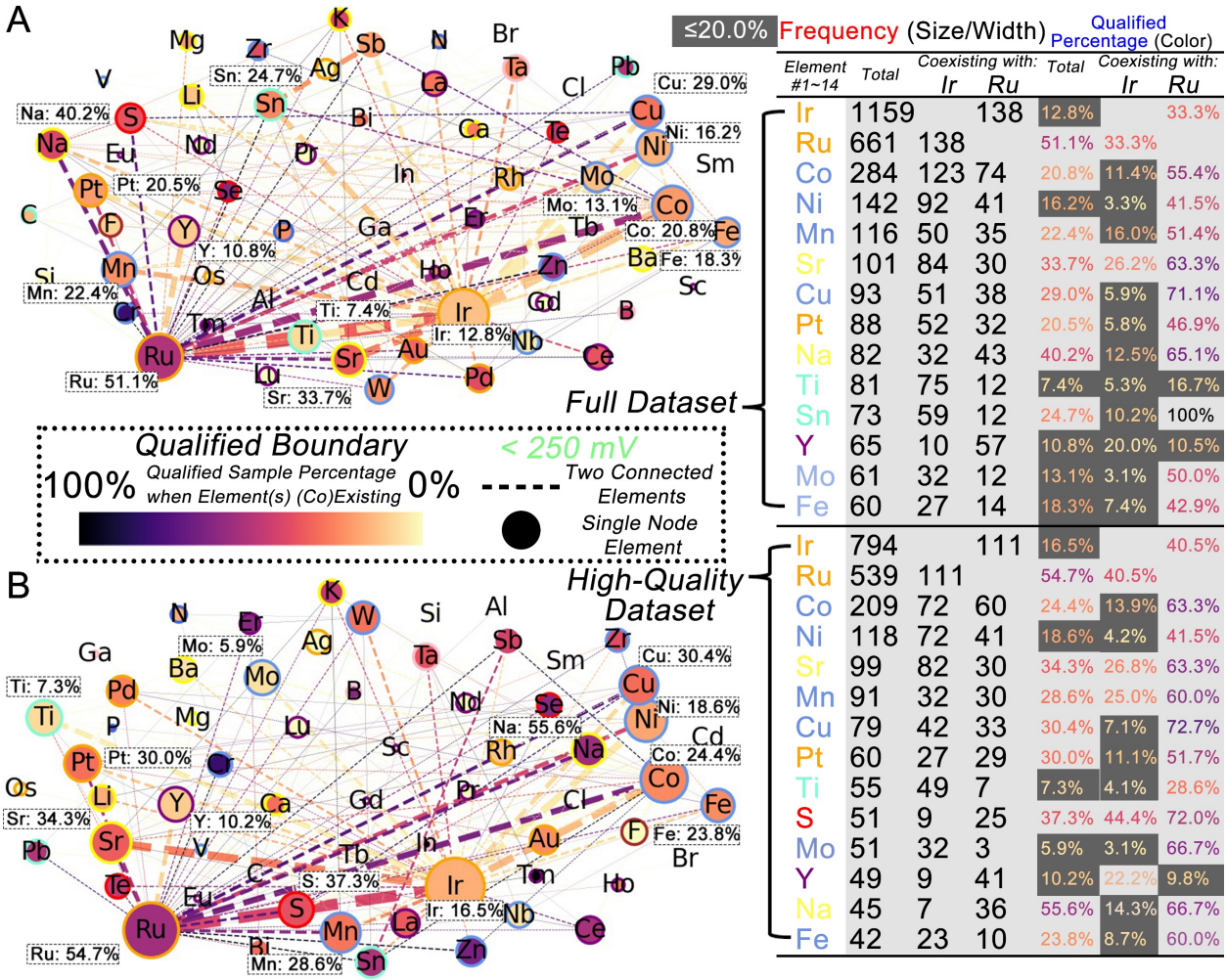

Fig. S3 Network graphs and summary of chemical elements based on overpotential thresholds for acidic OER electrocatalysts. (A) Network graph based on the full dataset of chemical elements with a qualified overpotential boundary set at 250 mV. (B) Network graph based only on the high-quality dataset of chemical elements with a qualified overpotential boundary set at 250 mV (for network graphs herein, different colors at the edges of nodes represent different groups of elements. Aquamarine: C group; royal blue: N group; red: O group; pink: B group; brown: halogen; cornflower blue: earth abundant–transition metal; purple: rare earth metal; yellow: first/second group metal; and orange: noble metal.). The right-side table summarizes the frequencies of elements by themselves, or coexisting with Ir/Ru, as well as the corresponding qualified percentages (η_{10} <250 mV). A detailed discussion is provided in **Supplementary Note 2** (https://github.com/ruiding-uchicago/DASH).

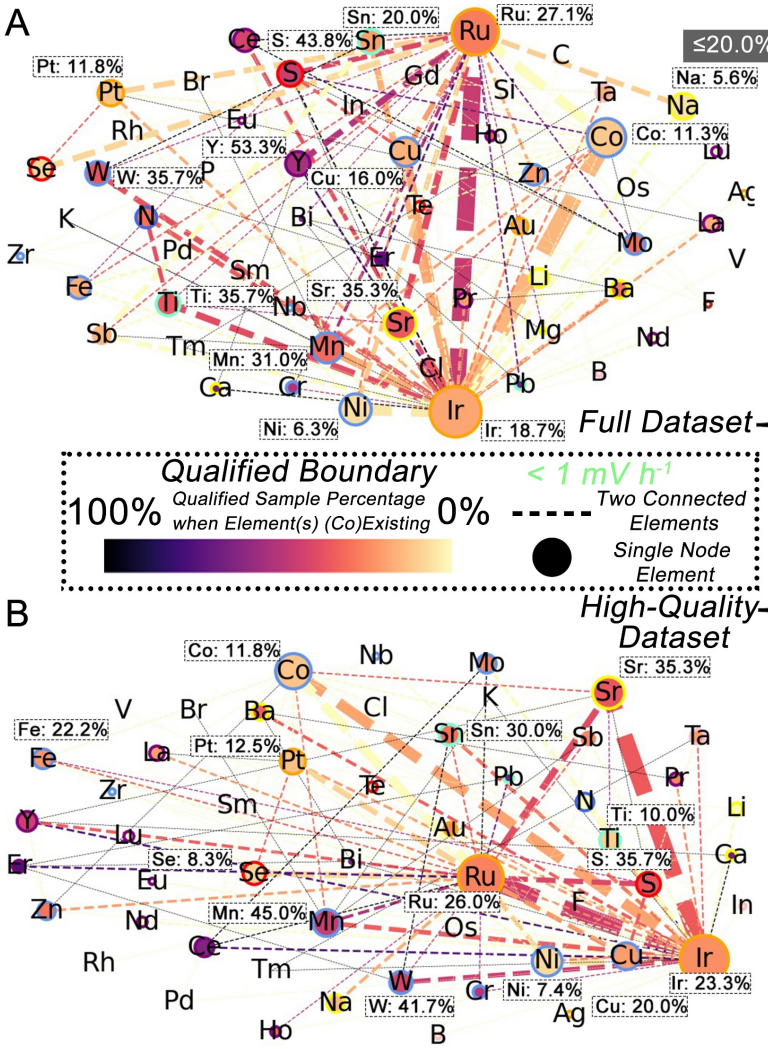

Element #1~14	Total	Coexisting with: Ir	Coexisting with: Ru	Qualified Percentage: Total	Qualified Percentage: Coexisting with: Ir	Qualified Percentage: Coexisting with: Ru
Ir	284		33	18.7%		45.5%
Ru	170	33		27.1%	45.5%	
Co	71	33	19	11.3%	15.2%	0%
Sr	34	32	13	35.3%	34.4%	38.5%
Ni	32	23	9	6.3%	4.3%	11.1%
Mn	29	18	6	31.0%	16.7%	50.0%
Cu	25	16	10	16.0%	18.8%	20.0%
Na	18	8	10	5.6%	0%	10.0%
Pt	17	6	11	11.8%	16.7%	9.1%
S	16	3	10	43.8%	100%	40.0%
Sn	15	12	3	20.0%	16.7%	33.3%
Y	15	4	12	53.3%	75.0%	50.0%
W	14	11	2	35.7%	36.4%	50.0%
Ti	14	13	2	35.7%	38.5%	50.0%
Ir	206		32	23.3%		43.8%
Ru	146	32		26.0%	43.8%	
Co	51	21	18	11.8%	19.0%	0%
Sr	34	32	13	35.3%	34.4%	38.5%
Ni	27	18	9	7.4%	5.6%	11.1%
Cu	20	12	9	20.0%	25.0%	22.2%
Mn	20	9	6	45.0%	33.3%	50.0%
Pt	16	5	11	12.5%	20.0%	9.1%
S	14	2	10	35.7%	100%	40.0%
W	12	9	2	41.7%	44.4%	50.0%
Se	12	0	12	8.3%	0%	8.3%
Ti	10	9	1	10.0%	11.1%	0%
Sn	10	7	3	30.0%	28.6%	33.3%
Fe	9	3	3	22.2%	0%	33.3%

Fig. S4 Network graphs and summary of chemical elements based on decay rate thresholds for acidic OER electrocatalysts. (A) Network graph based on the full dataset of chemical elements with a qualified decay rate boundary set at 1 mV h^{-1}. (B) Network graph based only on the high-quality dataset of chemical elements with a qualified decay rate boundary set at 1 mV h^{-1} (for network graphs herein, different colors at the edges of nodes represent different groups of elements. Aquamarine: C group; royal blue: N group; red: O group; pink: B group; brown: halogen; cornflower blue: earth abundant–transition metal; purple: rare earth metal; yellow: first/second group metal; and orange: noble metal.). The right-side table summarizes the frequencies of elements by themselves, or coexisting with Ir/Ru, as well as the corresponding qualified percentages (decay rate <1 mV h^{-1}). A detailed discussion is provided in **Supplementary Note 2**.

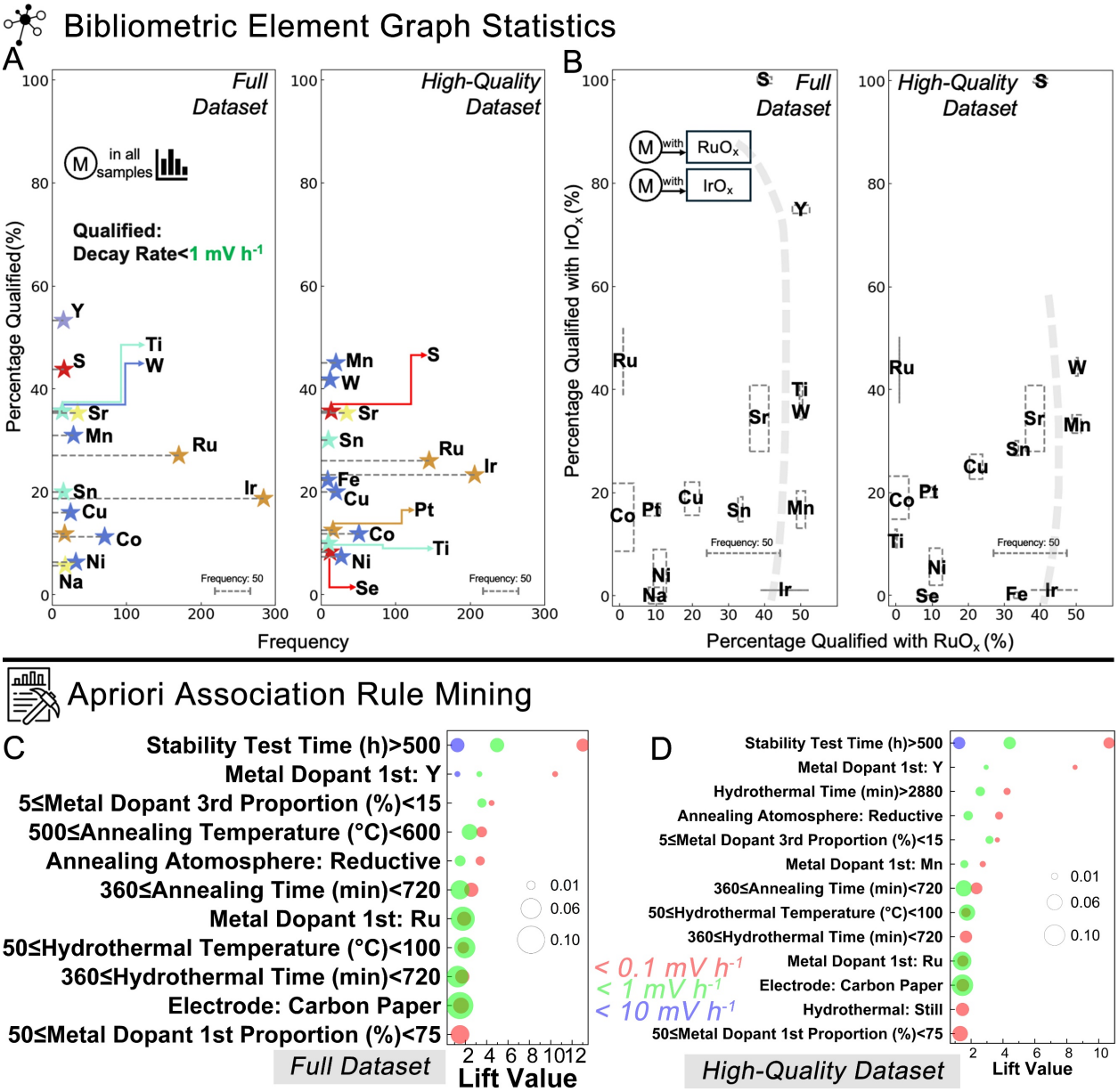

Fig. S5 Key results derived from unsupervised data mining focused on OER stability. Key results derived from unsupervised data mining focused on OER stability. (A) Frequencies and qualified percentages of different most frequently reported chemical elements in the full dataset and the high-quality dataset, with a qualified decay rate boundary set at 1 mV h^{-1}. (B) Frequencies and qualified percentages of different most frequently reported chemical elements coexisting with either Ru or Ir in metal oxides in the full dataset and the high-quality dataset with the same decay rate boundary. The dashed line represents the predicted frontier based on the promising elements in the figure that exhibit superior performance (i.e., higher frequencies) and simultaneously have larger *x*- and *y*-coordinate values. ((A) and (B) are derived from the original graph **fig. S4**.) (C) Results of high lift values in Apriori associate rule mining based on the full domain knowledge dataset with a frequent itemset length of two for stability-related insights; (D) Results of high lift values in Apriori associate rule mining based on a high-quality domain knowledge dataset with the frequent itemset length of two for stability-related insights.

Supplementary Discussion S1

In the supervised data-mining process, we adopt a robust and comprehensive approach to hyperparameter optimization in our regression ML models in the committees, a process that is instrumental in maximizing model performance and ensuring the validity of our results.

Hyperparameter Optimization Strategy

Our strategy involves a meticulous application of five-fold cross-validation (CV) exclusively on the training data set. This process segregates the training data into five distinct subsets. In each iteration of the CV, four subsets are used for training the model, while the remaining subset serves as the validation set. This cycle is repeated five times, ensuring that each subset is used for validation once. This approach allows each model to be trained and validated on different data segments, thus effectively honing its hyperparameters. By confining this process within the training data, we eliminate the risk of data leakage and ensure that the test data remains an unbiased arbitrator of model performance.

The absence of test data involvement in this stage is crucial for maintaining the integrity of our evaluation process. It guarantees that the model's hyperparameters are optimized without any foreknowledge of the test data, thus ensuring that the final evaluation on the test set is conducted under fair and unbiased conditions. This method not only enhances the reliability of our results, but also ensures that the models are evaluated based on their ability to generalize to new, unseen data.

Performance Metrics

To comprehensively assess the performance of our ML models, we employ a suite of statistical metrics, each providing unique insights into the model's accuracy and efficacy.

1. Mean Absolute Error (MAE): MAE measures the average magnitude of errors in a set of predictions without considering their direction. It is calculated using the Equation (S1):

$$\mathrm{MAE} = \frac{1}{n}\sum_{i=1}^{n}|y_i - \hat{y}_i| \ (Equation\ S1)$$

where $\hat{y}_i$ represents the actual value and y_i represents the predicted value. MAE is particularly useful because it provides a straightforward interpretation of the average error magnitude.

2. Mean Squared Error (MSE): MSE provides a measure of the quality of an estimator—it is always non-negative, and values closer to zero are better. It is given by Equation (S2):

$$\mathrm{MSE} = \frac{1}{n}\sum_{i=1}^{n}(y_i - \hat{y}_i)^2 \ \ (Equation\ S2)$$

MSE penalizes larger errors more severely than smaller ones, making it sensitive to outliers in the data.

3. Root Mean Squared Error (RMSE): RMSE is the square root of the MSE and is used to measure the difference between values predicted by a model and the values observed. The formula is Equation (S3):

$$\mathrm{RMSE} = \sqrt{\frac{1}{n}\sum_{i=1}^{n}(y_i - \hat{y}_i)^2} \ \ (Equation\ S3)$$

RMSE is in the same units as the response variable and is particularly useful for understanding the error magnitude in the context of the measured data.

4. Coefficient of Determination (R^2): R^2 quantifies how well future outcomes are likely to be predicted by the model. It is defined as Equation (S4):

$$R^2 = 1 - \frac{\sum_{i=1}^{n}(y_i - \hat{y}_i)^2}{\sum_{i=1}^{n}(y_i - \bar{y})^2} \ (Equation\ S4)$$

where $\bar{y}$ is the mean of the observed data. R^2 provides a scale for model comparison, indicating the proportion of variance in the dependent variable that can be explained by the independent variables in the model.

Regression Performance Discussion

As we briefly discussed in the main text, most of the regression models in the four committees, either based on full or high-quality datasets or focused on activity or stability, have shown comparatively good predicting abilities. In particular, the best-performing algorithms among the 11 models in our committee in terms of the R^2 values were identified as ensemble models, such as CatBoost, Random Forest, and Gradient Boosting, thus highlighting their effectiveness and the value of their SHAP matrices as representative for deeper materials science insights. Our domain knowledge dataset, rooted in experimental research literature, inevitably contains significant experimental detail variations such as disparities in synthesis preparation and testing characterization methods among different laboratories and researchers. These variations may introduce unavoidable but non-negligible noise in the dataset. However, as demonstrated through the statistical analysis of four key metrics for different regression models in **figs. S6, S7, S10, S11**, it is evident that the top-performing ensemble algorithms often achieve R^2 values close to or exceeding 0.8 on the test set. The R^2 value, commonly regarded as highly significant due to its ability to quantify the proportion of variance in the dependent variable that is predictable from the independent variable, underscores the reliability of our domain knowledge dataset and the robust predictive power of the ML models derived from it.

These models exhibit substantial robustness against outliers in the dataset, effectively learning the overarching trends within the studied material system. Additionally, an intriguing observation from our study is that despite the high-quality dataset and the full dataset appearing to share a similar distribution pattern, as shown in **fig. S1B**, ML models trained on these datasets exhibited noteworthy differences in performance. As summarized in **Fig. 3A**, the top-performing algorithms demonstrated a lower MAE when using the high-quality dataset. This trend was further corroborated by the MSE and RMSE metrics. This finding aligns with our initial assumption that data entries sourced from varying levels of reliability may differentially impact model performance due to their respective outlier and noise levels.

Scripts in this part for activity or stability regression models can be retrieved in the directory "Domain Knowledge-Based Initial ML Committee and Blackbox Interpretation/ Regression/Activity/Initial ML Committee Training/" (for stability regression, find the folder named "Stability", which is a same-level directory of "Activity").

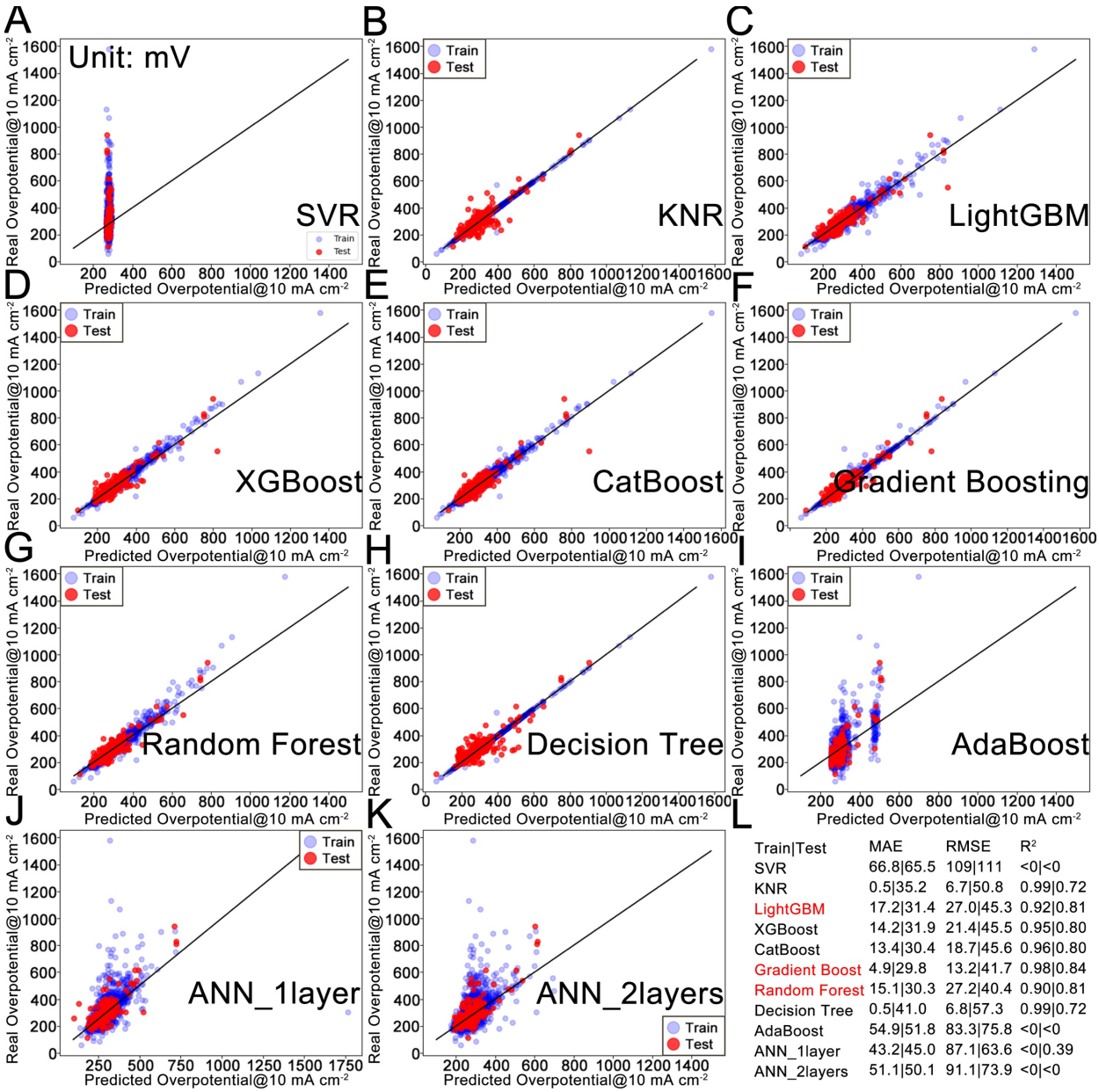

L

Train|Test	MAE	RMSE	R^2
SVR	66.8|65.5	109|111	<0|<0
KNR	0.5|35.2	6.7|50.8	0.99|0.72
LightGBM	17.2|31.4	27.0|45.3	0.92|0.81
XGBoost	14.2|31.9	21.4|45.5	0.95|0.80
CatBoost	13.4|30.4	18.7|45.6	0.96|0.80
Gradient Boost	4.9|29.8	13.2|41.7	0.98|0.84
Random Forest	15.1|30.3	27.2|40.4	0.90|0.81
Decision Tree	0.5|41.0	6.8|57.3	0.99|0.72
AdaBoost	54.9|51.8	83.3|75.8	<0|<0
ANN_1layer	43.2|45.0	87.1|63.6	<0|0.39
ANN_2layers	51.1|50.1	91.1|73.9	<0|<0

Fig. S6 Performance of ML models for predicting η_{10} using the full domain knowledge dataset. Scatter diagrams of the ML model committee members, namely different algorithms trained to predict η_{10} based on the full domain knowledge dataset. The red point's *x* axis value indicates the predicted outcome from the machine-learning model for a specific sample in the test set, whereas its *y* axis value reflects the actual recorded value in the dataset. Similarly, the blue points represent the results in the training set. The black line, represented by y=x, functions as a benchmark: the proximity of these red points to the y=x line is indicative of the model's prediction accuracy. Diagrams corresponding to the different hyperparameter-optimized algorithms: (A) SVR, (B) KNR, (C) LightGBM, (D) XGBoost, (E) CatBoost, (F) Gradient Boost, (G) Random Forest, (H) Decision Tree, (I) AdaBoost, (J) ANN with one hidden layer, (K) ANN with two hidden layers, and (L) summary of the key performance metrics for regression, with the top three in terms of R^2 highlighted in red font.

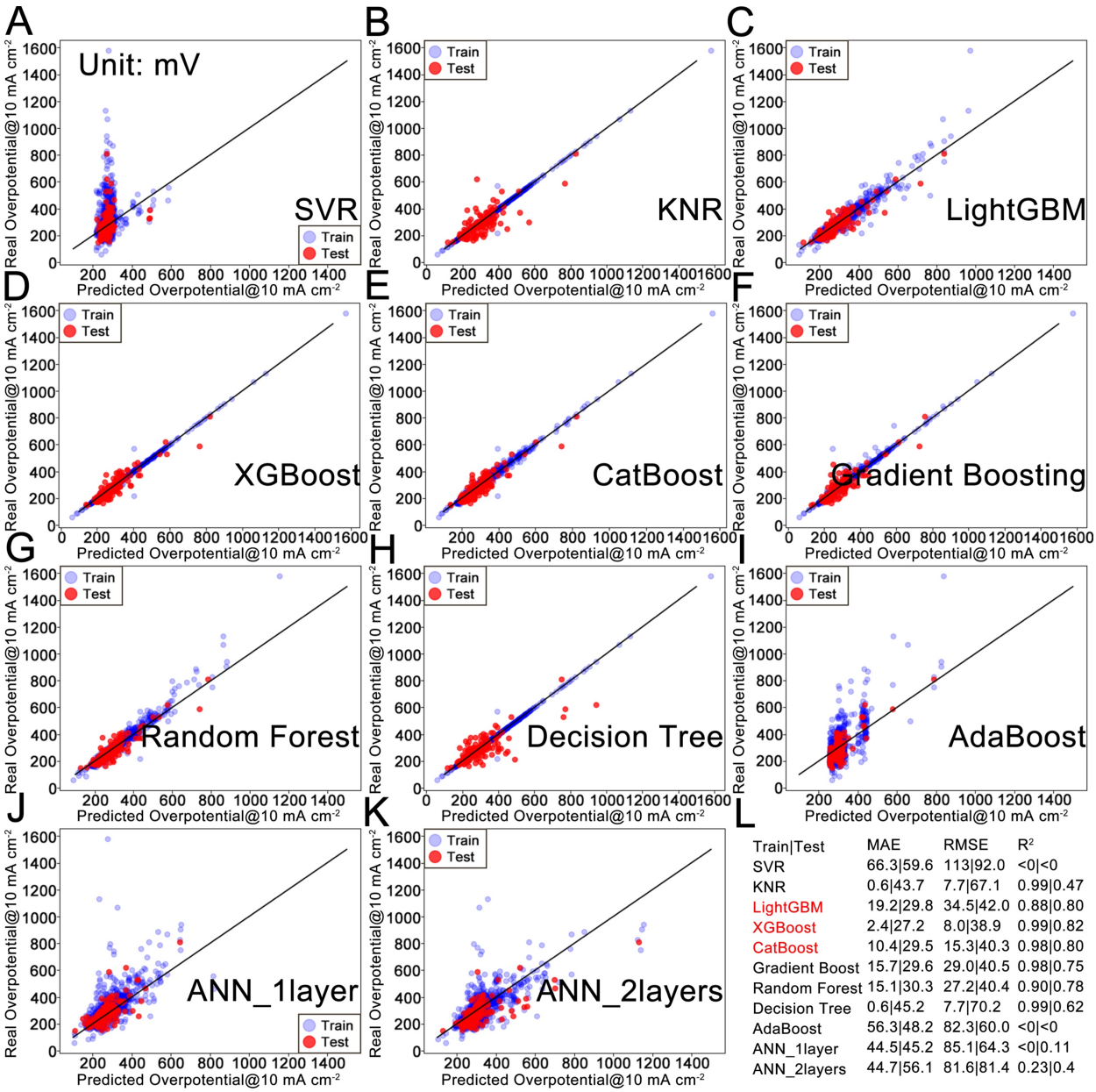

L

Train|Test	MAE	RMSE	R^2
SVR	66.3|59.6	113|92.0	<0|<0
KNR	0.6|43.7	7.7|67.1	0.99|0.47
LightGBM	19.2|29.8	34.5|42.0	0.88|0.80
XGBoost	2.4|27.2	8.0|38.9	0.99|0.82
CatBoost	10.4|29.5	15.3|40.3	0.98|0.80
Gradient Boost	15.7|29.6	29.0|40.5	0.98|0.75
Random Forest	15.1|30.3	27.2|40.4	0.90|0.78
Decision Tree	0.6|45.2	7.7|70.2	0.99|0.62
AdaBoost	56.3|48.2	82.3|60.0	<0|<0
ANN_1layer	44.5|45.2	85.1|64.3	<0|0.11
ANN_2layers	44.7|56.1	81.6|81.4	0.23|0.4

Fig. S7 Performance of ML models for predicting η_{10} using the full domain knowledge dataset. Similar to **Fig. S6**, scatter diagrams of the ML model committee members, namely different algorithms trained to predict η_{10} based on the high-quality domain knowledge dataset. Diagrams corresponding to the different hyperparameter optimized algorithms: (A) SVR, (B) KNR, (C) LightGBM, (D) XGBoost, (E) CatBoost, (F) Gradient Boost, (G) Random Forest, (H) Decision Tree, (I) AdaBoost, (J) ANN with one hidden layer, (K) ANN with two hidden layers, and (L) summary of the key performance metrics for regression, with the top three in terms of R^2 highlighted in red font.

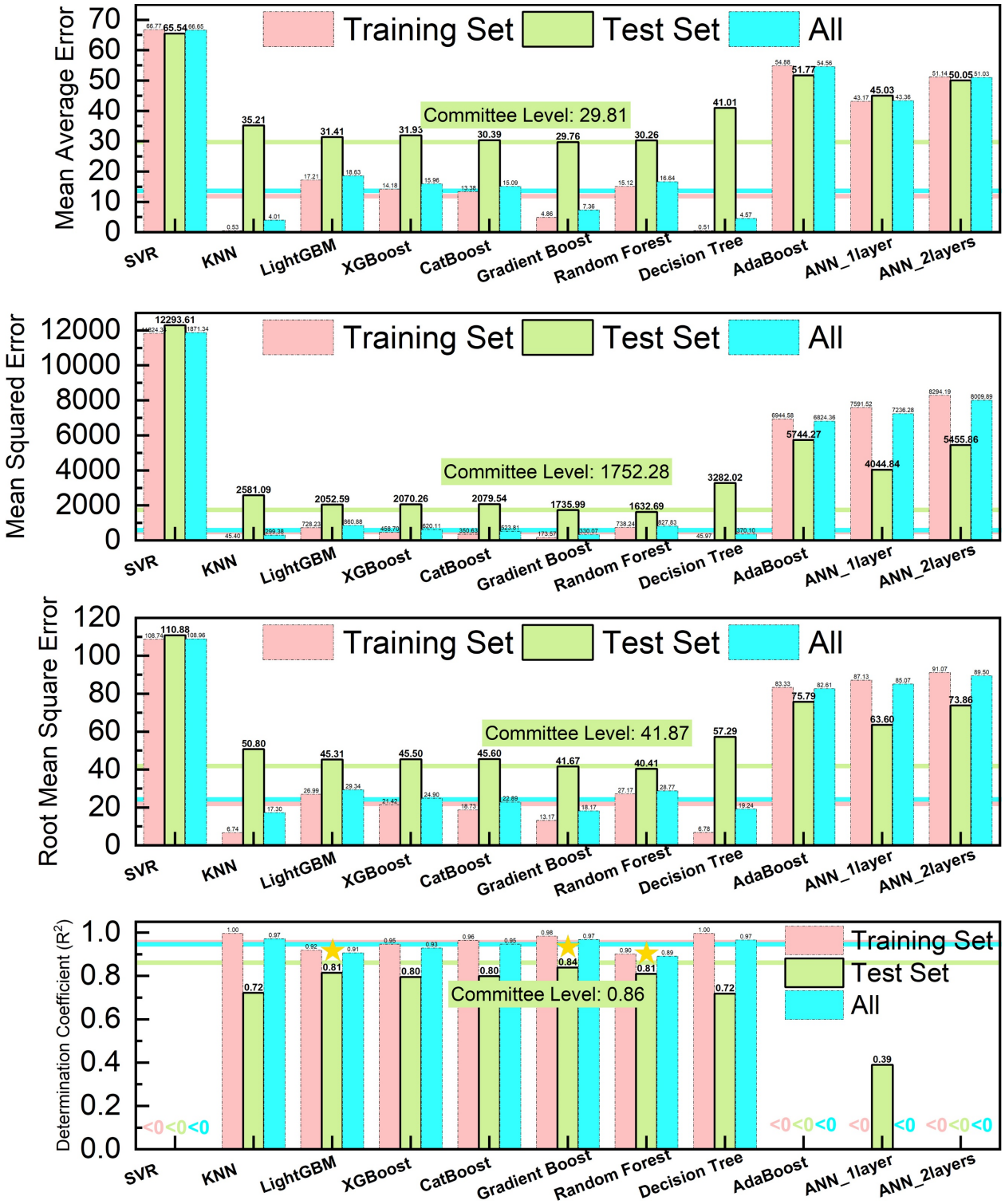

Fig. S8 Summary of regression performance for ML models predicting η_{10} in the full domain knowledge dataset. These histograms correspond to regression performance metrics on ML models illustrated in **Fig. S6**. (Please note that it is possible that the committee of models could get close or even outperform (e. g. R^2=0.86 for committee) its best-performing member (R^2=0.84) on the test set by leveraging the complementary strengths of individual models, reducing errors through ensemble averaging.)

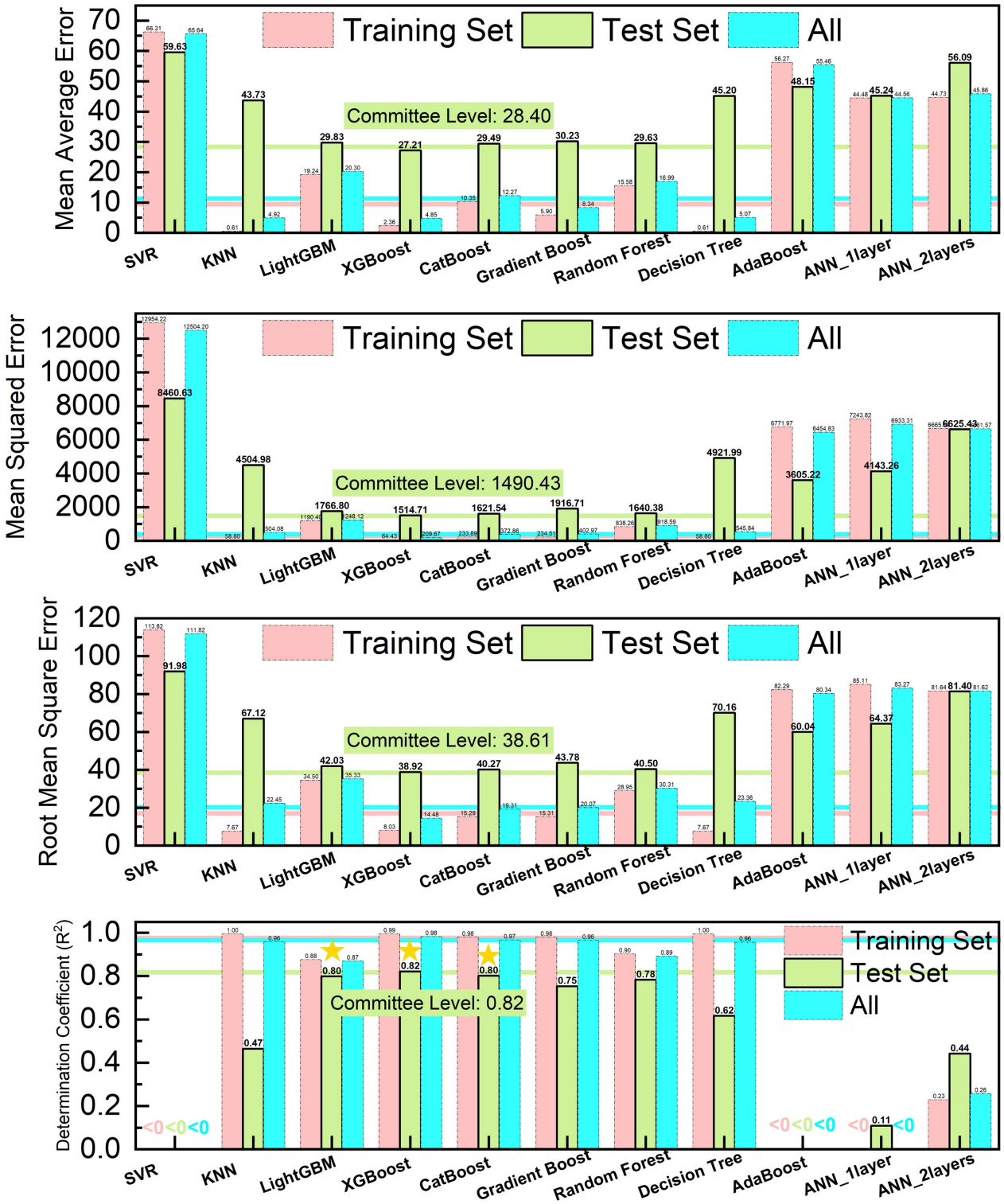

Fig. S9 Summary of regression performance for ML models predicting η_{10} in the full domain knowledge dataset. These histograms correspond to regression performance metrics on ML models illustrated in **Fig. S7**.

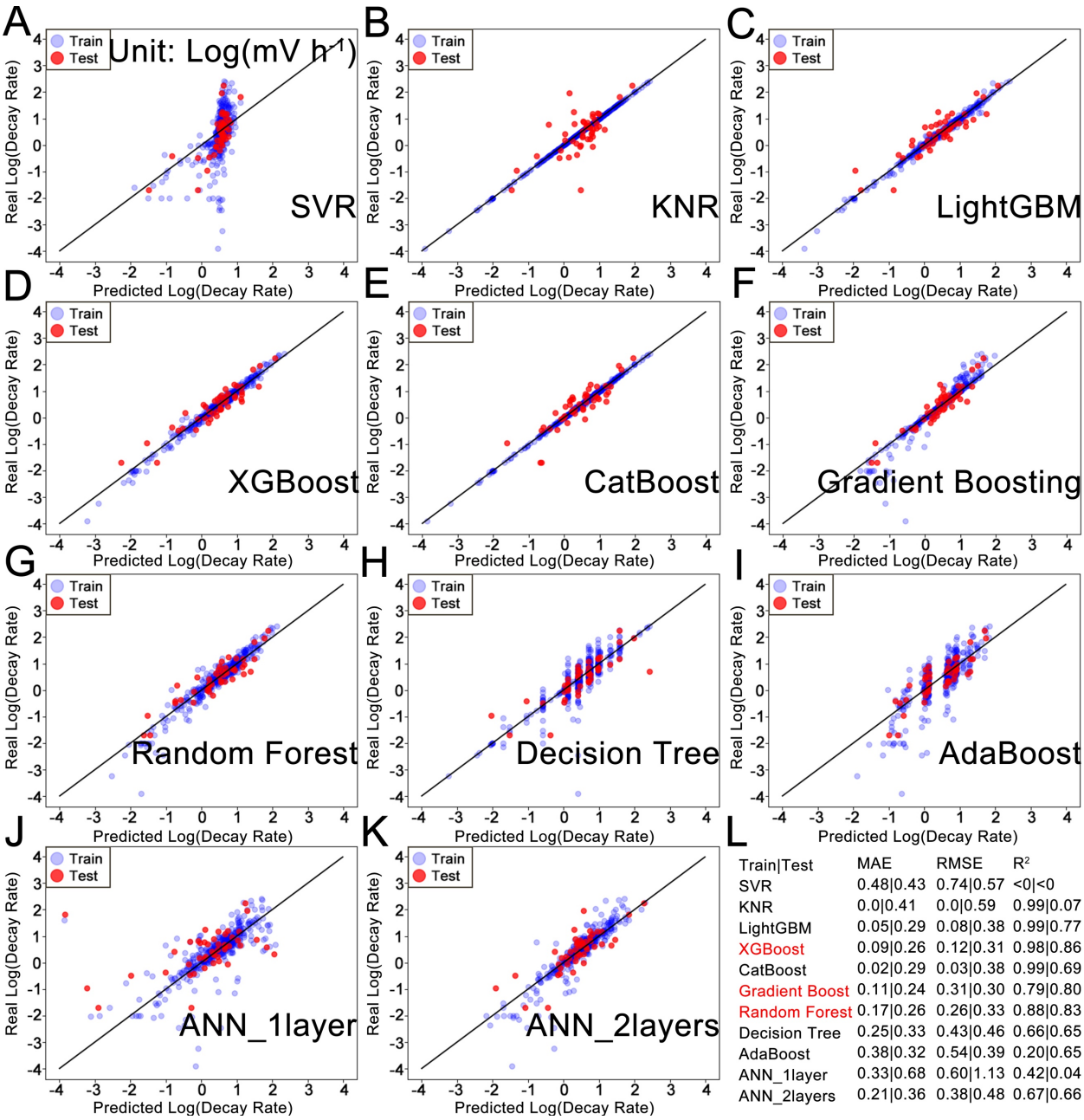

L

Train|Test	MAE	RMSE	R^2
SVR	0.48|0.43	0.74|0.57	<0|<0
KNR	0.0|0.41	0.0|0.59	0.99|0.07
LightGBM	0.05|0.29	0.08|0.38	0.99|0.77
XGBoost	0.09|0.26	0.12|0.31	0.98|0.86
CatBoost	0.02|0.29	0.03|0.38	0.99|0.69
Gradient Boost	0.11|0.24	0.31|0.30	0.79|0.80
Random Forest	0.17|0.26	0.26|0.33	0.88|0.83
Decision Tree	0.25|0.33	0.43|0.46	0.66|0.65
AdaBoost	0.38|0.32	0.54|0.39	0.20|0.65
ANN_1layer	0.33|0.68	0.60|1.13	0.42|0.04
ANN_2layers	0.21|0.36	0.38|0.48	0.67|0.66

Fig. S10 Performance of machine learning models for predicting decay rate using the full domain knowledge dataset. Scatter diagrams of the ML model committee members, namely different algorithms trained to predict the decay rate based on the full domain knowledge dataset. Diagrams corresponding to the different hyperparameter optimized algorithms: (A) SVR, (B) KNR, (C) LightGBM, (D) XGBoost, (E) CatBoost, (F) Gradient Boost, (G) Random Forest, (H) Decision Tree, (I) AdaBoost, (J) ANN with one hidden layer, (K) ANN with two hidden layers, and (L) summary of the key performance metrics for regression, with the top three in terms of R^2 highlighted in red font.

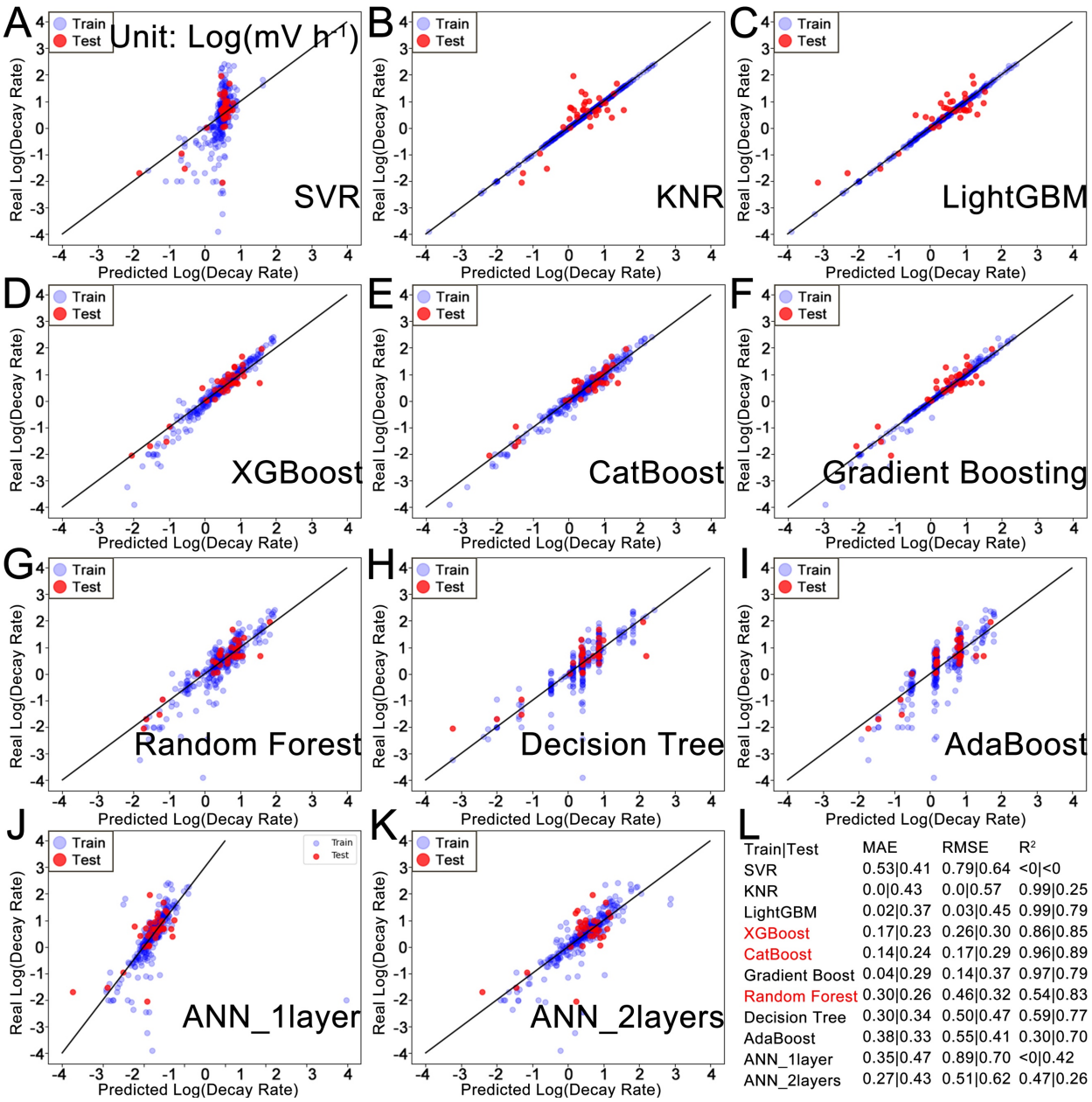

L

Train|Test	MAE	RMSE	R^2
SVR	0.53|0.41	0.79|0.64	<0|<0
KNR	0.0|0.43	0.0|0.57	0.99|0.25
LightGBM	0.02|0.37	0.03|0.45	0.99|0.79
XGBoost	0.17|0.23	0.26|0.30	0.86|0.85
CatBoost	0.14|0.24	0.17|0.29	0.96|0.89
Gradient Boost	0.04|0.29	0.14|0.37	0.97|0.79
Random Forest	0.30|0.26	0.46|0.32	0.54|0.83
Decision Tree	0.30|0.34	0.50|0.47	0.59|0.77
AdaBoost	0.38|0.33	0.55|0.41	0.30|0.70
ANN_1layer	0.35|0.47	0.89|0.70	<0|0.42
ANN_2layers	0.27|0.43	0.51|0.62	0.47|0.26

Fig. S11 Performance of machine learning models for predicting decay rate using the high-quality domain knowledge dataset. Scatter diagrams of the ML model committee members, namely different algorithms trained to predict the decay rate based on the high-quality domain knowledge dataset. Diagrams corresponding to the different hyperparameter optimized algorithms: (A) SVR, (B) KNR, (C) LightGBM, (D) XGBoost, (E) CatBoost, (F) Gradient Boost, (G) Random Forest, (H) Decision Tree, (I) AdaBoost, (J) ANN with one hidden layer, (K) ANN with two hidden layers, and (L) summary of the key performance metrics for regression, with the top three in terms of R^2 highlighted in red font.

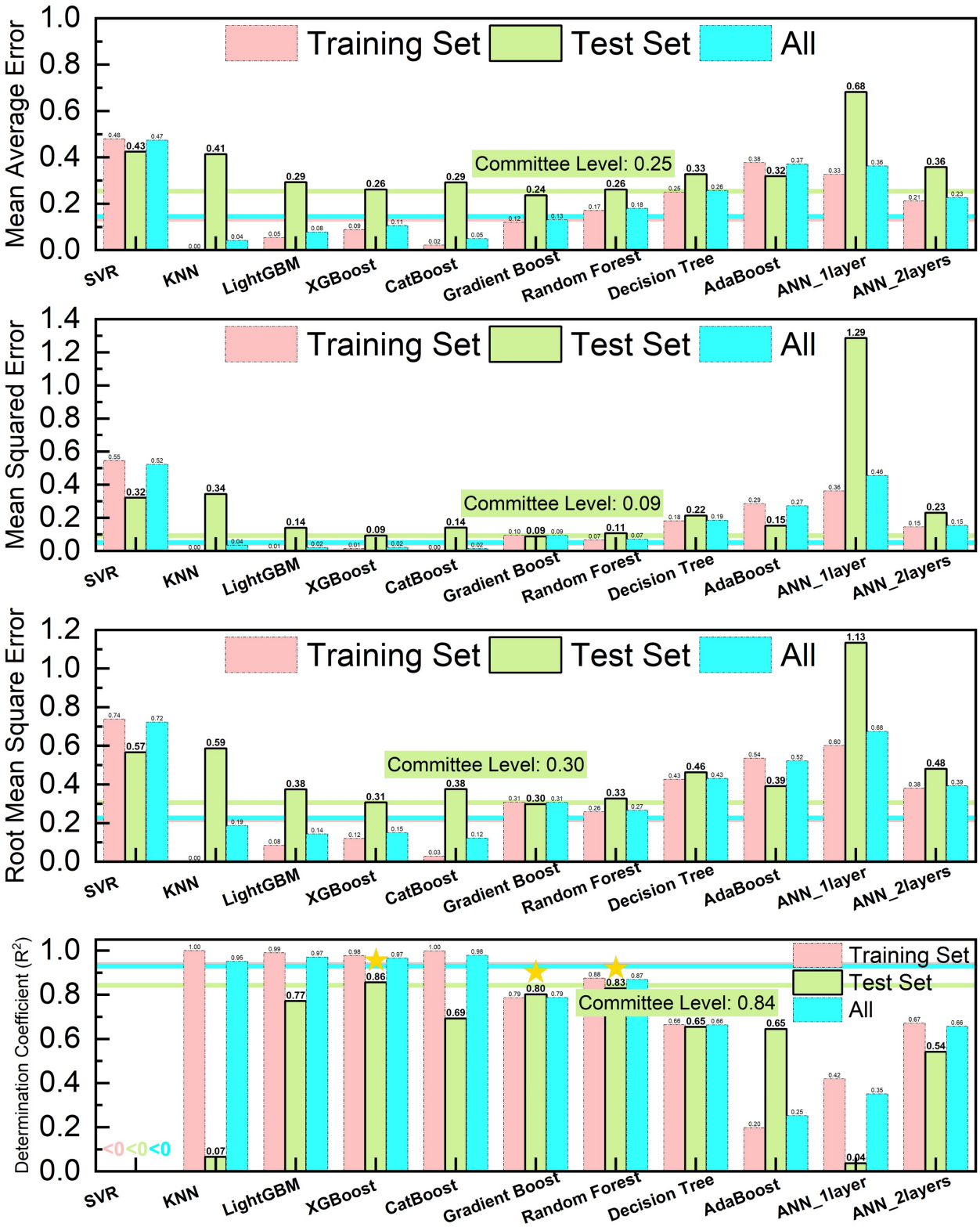

Fig. S12 Summary of regression performance for ML models predicting decay rate in the full domain knowledge dataset. These histograms correspond to regression performance metrics on ML models illustrated in **Fig. S10**.

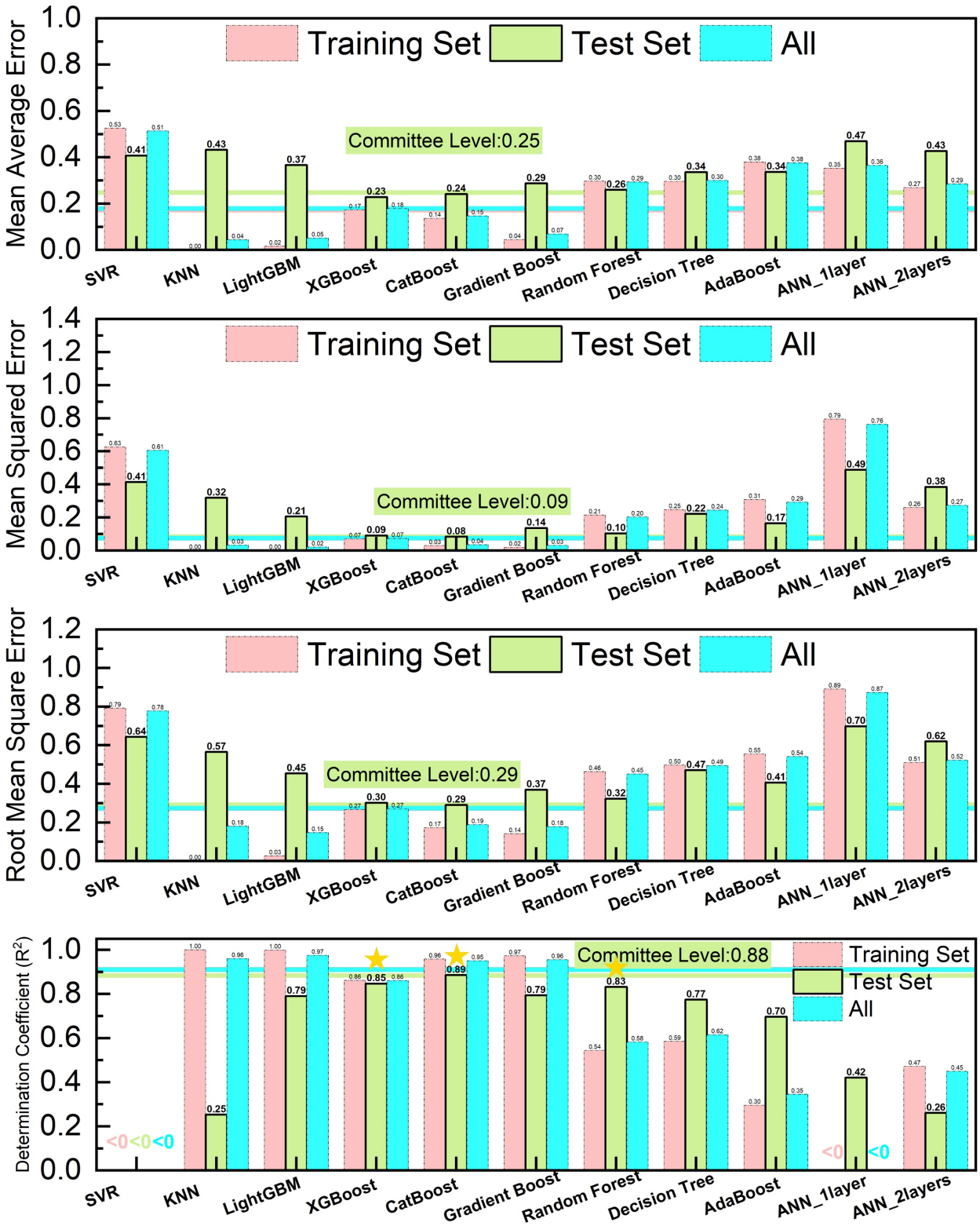

Fig. S13 Summary of regression performance for ML models predicting decay rate in the high-quality domain knowledge dataset. These histograms correspond to regression performance metrics on ML models illustrated in **Fig. S11**.

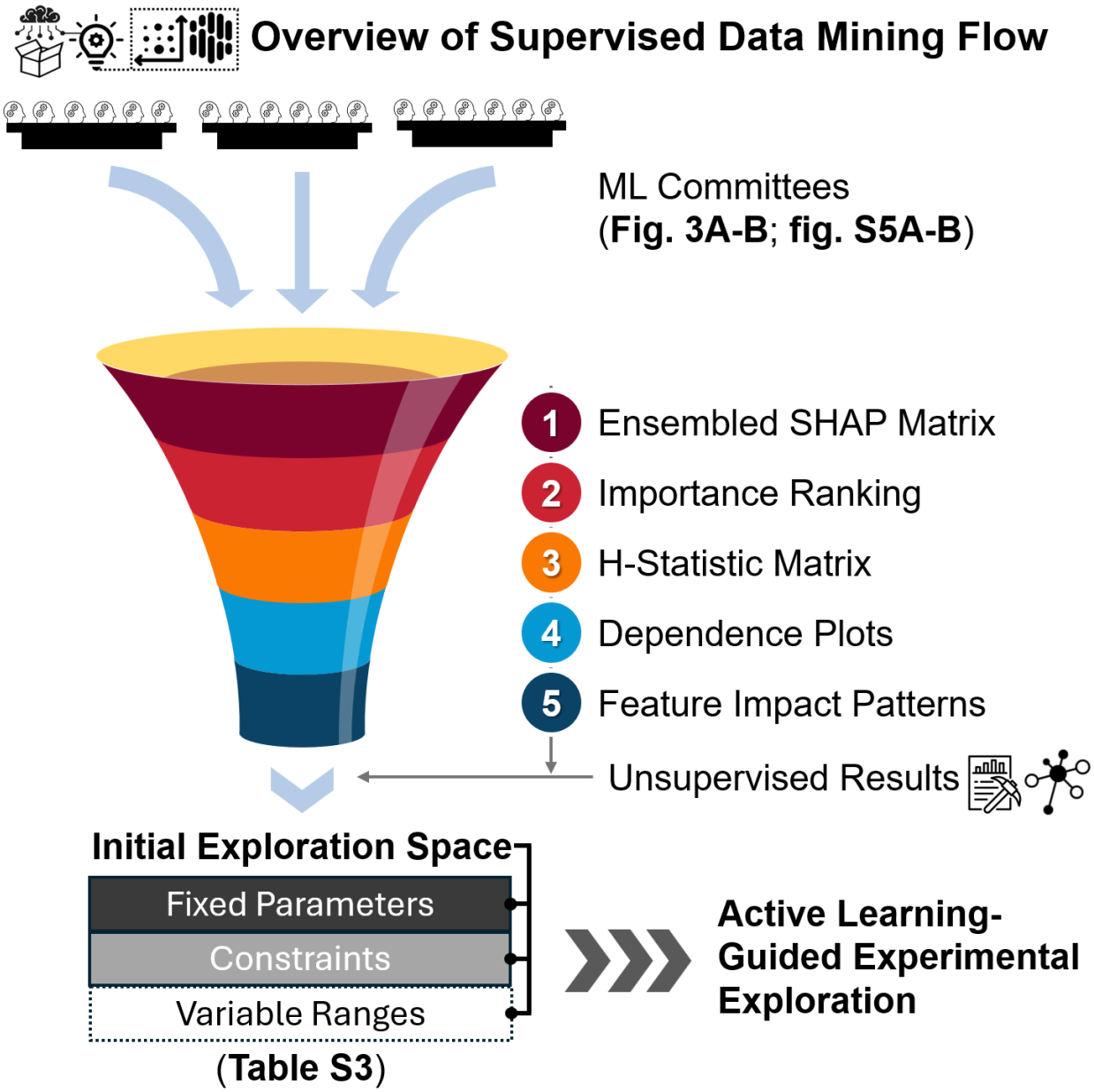

Fig. S14 Flowchart of black-box interpretation tools in supervised machine learning for data mining. The flowchart illustrates the integration of various black-box interpretation tools used in the supervised data-mining component of the ML models. A detailed discussion, including nuanced explanations and original results, can be found in **Supplementary Note 4** (https://github.com/ruiding-uchicago/DASH).

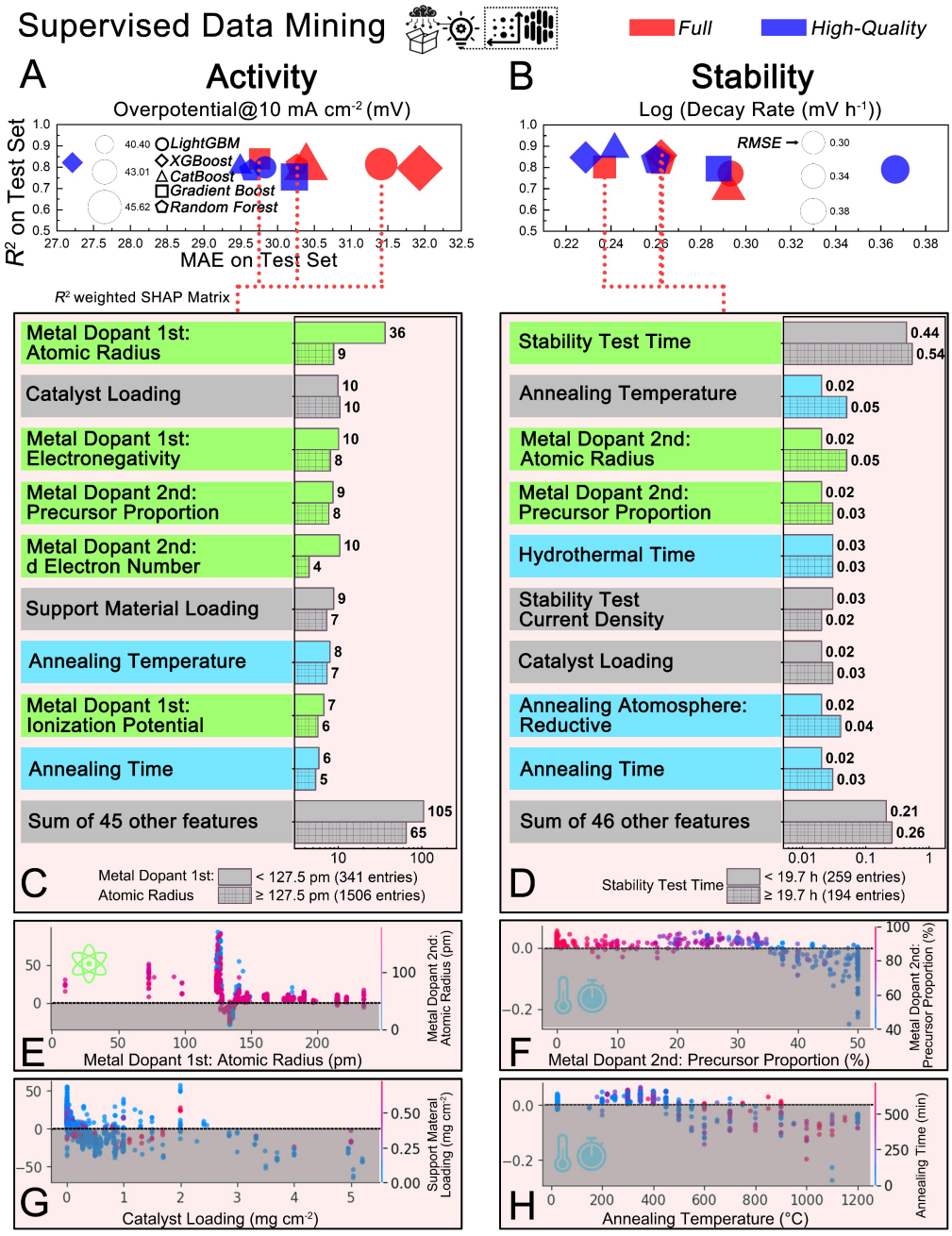

Fig. S15 Key results derived from supervised data mining on the high-quality domain knowledge dataset. (A) and (B): The top five ML models, as identified from committees trained on various domain knowledge datasets, are evaluated based on R^2 and MAE metrics on the test set. (C)-(D) SHAP cohort bar plots that highlight the important features with light green and blue frames highlighting the element-related features: atomic properties and synthesis condition parameters, respectively. (E)-(H) Selected SHAP two-dimensional interaction plots that feature an interaction of the primary studied feature on the *x* axis with a second feature, which is indicated by the color bars. The second features, also chosen from the top features with a similar type, are those with a high degree of interaction in the Friedman's H-statistic interaction matrix. Dashed lines at y=0 in each dependence plots split-grey areas that indicate the preferred value ranges.

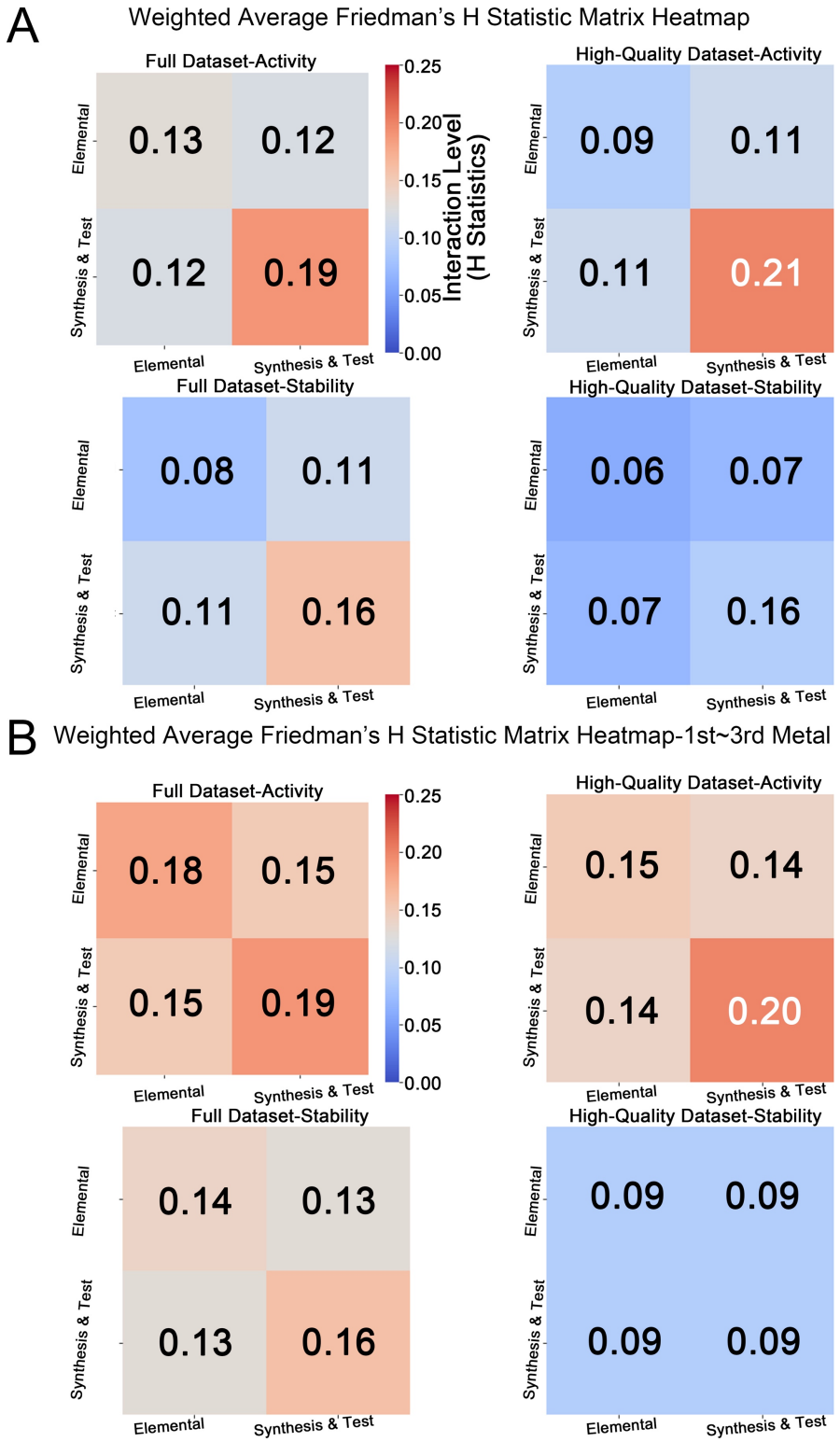

Fig. S16 Analysis of feature interaction strengths using Friedman's H statistic. (A) Friedman's H statistic of the weighted average matrix heatmap for illustration of the average interaction strength between different categories of features. The original heatmap could be found in Supplementary Note 4: Figure SN 4-1/4-2/4-19/4-20. (B) the version of (A) when elemental features of the major three metal elements only are considered.

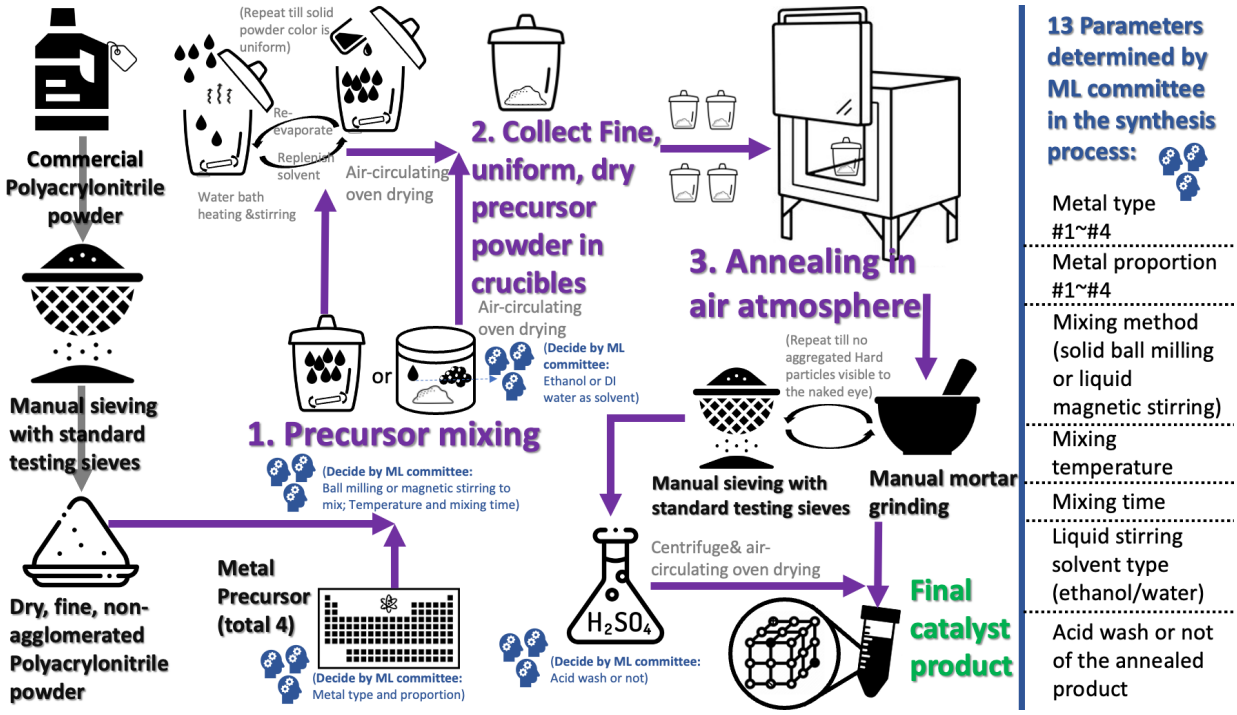

Fig. S17 Visualized synthesis process for OER electrocatalyst samples used in this study. Illustration of the synthesis process for OER electrocatalyst samples, featuring vivid icons and detailed steps to represent experimental procedures.

Supplementary Discussion S2

Details of the Experimental Synthesis and Electrochemical Evaluation Processes

Synthesis of Polymetallic Oxide Samples

The preparation of polyacrylonitrile powder began with commercial polyacrylonitrile, which underwent manual sieving using standard testing sieves to yield a dry, fine, non-agglomerated product weighing 150 mg. Concurrently, a solution of metal precursors, comprising a total of four types, was prepared in a water: ethanol (1:1) mixed solvent. These metal salt precursors were all dissolved in the 1:1 water: ethanol mixture for future use, with the specific molar amount determined based on the equivalent molar quantity to 50 mg of hydrated ruthenium chloride, per the ML committee's prediction in each iteration. This involved drawing the metal solution with a pipette to extract a certain amount.

The mixing method, either ball milling or magnetic stirring, was decided by the ML committee. For ball milling, constraints were applied during the ML algorithm prediction: when ball milling was selected, all solvents and reducing agents were set to zero in the GA computing processes, although the temperature was not constrained. The milling jar was preheated in an air-circulating oven to a specific temperature (if above room temperature) as predicted by the ML model before beginning the milling process. In the case of magnetic stirring, polyacrylonitrile powder and various metal solution precursors were dissolved in 20 mL of a specified solvent (ethanol or water). Since polyacrylonitrile powder has low solubility, the product was slurry-like. The mixture was then placed in a 30 mL crucible under water bath heating and stirring conditions at 90 °C. Magnetic stirring continued until the solvent completely evaporated, leaving a dry, non-clumpy powder. This solvent addition and evaporation process may be repeated multiple times as necessary.

Following this, the precursor powder from the previous step was transferred into a 30 mL crucible (the same one if the precursor was already in a liquid phase) and calcined in a muffle furnace at either 400 °C or 500 °C under air. The heating rate was maintained at 1.67 °C min^{-1} for six hours to obtain oxide samples. The resulting black mixed polymetallic oxide powder was then manually sieved using standard testing sieves and ground in a mortar until no aggregated hard particles were visible. This sieving and grinding process may be repeated as necessary. An optional acid washing step may be followed, as dictated by ML model predictions. If required, the product underwent acid washing in 0.5M H_2SO_4 at room temperature for eight hours. The acid-washed product was then collected by centrifugation, rinsed with DI water, and dried in an air-circulating oven to yield a fine powder. Ultimately, the final product, whether directly obtained from sieving and grinding or after undergoing acid washing, was ready for use as a catalyst for further OER electrochemical testing purposes.

Electrochemical Test in Half Cell

Half-cell tests for OER were conducted using a Rotating Disk Electrode (RDE). The experimental setup involved a typical standard three-electrode system, with a 5.00 mm-diameter RDE serving as the working electrode. A Reversible Hydrogen Electrode (RHE) was employed as the reference electrode after calibration, and a graphite rod was introduced as the counter electrode. The catalyst ink for the OER derived from oxide nanoparticles had a concentration of 11.78 mg mL^{-1}. The solvent for the ink was a mixture of isopropanol and Nafion perfluorinated resin solution (5 wt. % in isopropanol), with a volume ratio of 1:0.05. To prepare the ideal half-cell ink, the solid catalyst was pre-ground, as mentioned in Synthesis of polymetallic oxide samples, followed by ice-bath ultrasonication of the solid-liquid mixture until a uniform black suspension was obtained.

For electrochemical measurements, a specific amount of the ink was pipetted onto the glassy carbon of the RDE and naturally air-dried to achieve a smooth catalyst layer with a loading of 0.50 mg cm^{-2}. The evaluation of the OER catalytic performance was carried out in a 0.50 M H_2SO_4 aqueous solution (pH~0.3) (*121*) using Linear Sweep Voltammetry (LSV). The test temperature was maintained at 25 °C using a circulating water bath. During the LSV tests, the rotation speed was set at 1,600 rpm, with a scan rate of 10 mV s^{-1}.

The electrochemically-active surface area (ECSA) of the catalyst samples is calculated from the double-layer capacitance according to the Equation (S5) (*122*):

$$ECSA = C_{dl}/C_s \ (Equation\ S5)$$

Where C_s is the specific capacitance of the sample. Hence, we use general specific capacitances of $C_s = 0.03\ mF/cm^2$ based on typical reported value. The double-layer capacitance (C_{dl}) can be measured via cyclic voltammetric scan (CVs), a potential range in which no apparent Faradaic processes occurred. The range for CVs is 0.85-0.95 V. Scan rates are 20, 40, 60, 80, 100, and 120 mV/s, respectively.

ECSA-normalized activity at a given overpotential is another metric for evaluating the activity of a catalyst. The ECSA-normalized activity definition is based on the specific current density per ECSA ($J_{ECSA-200}$), which is calculated using the current density (J_{200}) at overpotential 200 mV and according to the Equation (S6):

$$J_{ECSA-200} = J_{200}/ECSA\ (Equation\ S6)$$

We conducted the half-cell stability test in the same standard three-electrode system, but used sintered titanium fiber felts (Bekipor, Bekaert) with a thickness of 250 μm (cleaned in an ultrasonic bath with ethanol and water) as the electrode with a size of 1 cm*1 cm, and the catalyst loading is unchanged. Without rotating the electrode, we placed a magnetic stirrer to ensure the mass transfer of the electrolyte. The constant current density was kept at 10 mA cm^{-2} for over 36 hours. All the half-cell tests were performed on electrochemical workstations CHI650e and CHI750e. Readers can retrieve all the tested data in the online repository in the directory “Experimental Records and Raw Data”.

Membrane Electrode Assembly Test in a Single Cell

The preparation of the Membrane Electrode Assembly (MEA) begins with the formulation of the ink. The procedure is as follows: 100 mg of 60 wt. % Pt/C catalyst is weighed and dispersed in ultrapure water. Acetone and Nafion D520 solutions are then added to the dispersion. Subsequently, the ink is stirred in an ice-water bath for 12 hours. After ultrasonic dispersion in an ultrasonic cleaner for 30 minutes, the ink is set aside for spray-coating on the cathode side for the HER. Similarly, for the anode side of the OER in single-cell tests, an analogous strategy is employed for preparing and dispersing the ink of Ru oxides.

The Catalyst-Coated Membrane (CCM) method is used, where the proton exchange membrane Nafion 115 is laid flat on the operation platform of an ultrasonic spray coater at a temperature of 100 °C. The ink is injected into the coater via a syringe and sprayed onto the membrane in a criss-cross pattern using ultrasonics. The flow rate of the spray is adjusted by regulating the carrier nitrogen gas pressure. The quantity of liquid is controlled by a motor while the distribution of the liquid is further managed by varying the coordinates, motor running speed, nozzle height, and nozzle angle. After coating, the final product is dried for 20 minutes. The same ultrasonic spray-coating process is then applied to the other side with the same parameters. The catalyst loadings are 0.4 mgPt cm^{-2} for the cathode and 1 mg cm^{-2} for the anode, with the overall MEA size of 2.5cm*2.5cm, resulting in a total area of 6.25 cm^2.

It is important to note that in both half-cell and single-cell configurations, the Ru content is not directly calculated but estimated based on the weight of the final product. According to ICP results, the Ru loadings for the final products A~D in the half-cell are estimated to be 0.221, 0.181, 0.2015, 0.163 mgRu cm $^{-2}$, respectively. For the single cell, these values are doubled: 0.442, 0.362, 0.403, 0.326 mgRu cm^{-2}. This use of precious metals is relatively low compared to other works on PEM electrolyzer MEAs (*123*) in the literature.

For the anode and cathode, the Ti fiber felt used previously for the half-cell stability test and carbon fiber paper (Freudenberg) with a thickness of 250 μm are used as porous transport layers (PTLs), respectively. The PTLs are hot-pressed with the MEA at 140 ℃ under a pressure of 6.0 MPa. The hot-pressed samples are then placed between two serpentine flow field plates and sealed with PTFE gaskets.

Before each test of the single cell, 80 °C deionized (DI) water (conductivity $\sigma \leq 1.0$ μS cm^{-1}) is supplied to the anode of the electrolyzer at a flow rate of 20.0 mL min^{-1} for eight hours. Subsequently, the electrolyzer is operated at a constant electrolysis voltage of 1.6 V until the current fluctuation is less than 1.0 mA per minute, ensuring proper hydration and stability of the MEA and activation procedure. Then, polarization curves are recorded in constant current mode, with steps of 0.1 A cm^{-2} when the current density exceeds 0.1 A cm^{-2}. More details, such as the instrument models, the MEA stability test method, and the electrochemical impedance spectroscopy (EIS) measurement can be found in our recent work on the poisoning effect of Ti ions in porous transport layers on PEM electrolyzer MEAs (*124*).

The chemicals used and corresponding suppliers are listed below:

$Zn(NO_3)_2 \cdot 6H_2O$ Sinopharm Chemical Reagent Co., Ltd.
$Fe(NO_3)_3 \cdot 9H_2O$ Sinopharm Chemical Reagent Co., Ltd.
$Co(NO_3)_2 \cdot 6H_2O$ Sinopharm Chemical Reagent Co., Ltd.
$Ni(NO_3)_2 \cdot 6H_2O$ Sinopharm Chemical Reagent Co., Ltd.
$Sc(NO_3)_3 \cdot 6H_2O$ Shandong Desheng New Material Co.
$Cu(NO_3)_2 \cdot 3H_2O$ Macklin
$Ga(NO_3)_3 \cdot 9H_2O$ Sinopharm Chemical Reagent Co., Ltd.
$Y(NO_3)_3 \cdot 6H_2O$ Shandong Desheng New Material Co.
$Zr(NO_3)_4 \cdot 6H_2O$ Macklin
$NbCl_5$ Macklin
VCl_3 jkchemical
$MoCl_3$ jkchemical
$Cr(NO_3)_3 \cdot 9H_2O$ Sinopharm Chemical Reagent Co., Ltd.
$Mn(NO_3)_2 \cdot 2H_2O$ Macklin
$RuCl_3.xH_2O$ Macklin
$CdCl_2 \cdot 5H_2O$ Macklin
$In(NO_3)_3$ Macklin
$RhCl_3 \cdot 3H_2O$ Macklin
$LaCl_3$ Macklin
$PrCl3 \cdot 6H_2O$ Shandong Desheng New Material Co.
$NdCl_3$ Shandong Desheng New Material Co.
$PmCl_3$ Shandong Desheng New Material Co.
$SmCl_3$ Shandong Desheng New Material Co.
$EuCl_3$ Shandong Desheng New Material Co.
$GdCl_3$ Shandong Desheng New Material Co.

$ErCl_3$ Shandong Desheng New Material Co.
$TmCl_3$ Shandong Desheng New Material Co.
$YbCl_3 \cdot H_2O$ Shandong Desheng New Material Co.
WCl_6 Aladdin
$ReCl_3$ Aladdin
$H2IrCl_6 \cdot 6H_2O$ Aladdin
$AuCl_3$ Aladdin
$Pb(NO_3)_2$ Sinopharm Chemical Reagent Co., Ltd.
$BaCO_3$ Macklin
$SrCO_3$ Sigma Aldrich
Na_2CO_3 Sinopharm Chemical Reagent Co., Ltd.
K_2CO_3 Sinopharm Chemical Reagent Co., Ltd.
$CaCO_3$ Sinopharm Chemical Reagent Co., Ltd.
MgCl2 Sinopharm Chemical Reagent Co., Ltd.
Li_2CO_3 Sinopharm Chemical Reagent Co., Ltd.
$SeCl_2$ jkchemical
$Al(NO_3)_3$ Sinopharm Chemical Reagent Co., Ltd.
Ethanol Sinopharm Chemical Reagent Co., Ltd.
H_2SO_4 Aladdin
Ultrapure water Nanjing Peiyin Instrument Co.
Isopropanol Sinopharm Chemical Reagent Co., Ltd.
Nafion perfluorinated resin solution (5 wt. % in isopropanol) Dupont

Table S3 Variable ranges and constant settings during GA search process.

Feature Name (Unit)	Variable Range (constant settings)
Metal_Dopant_1（1~4 represent the proportion in precursor from high to low）	71 different metal elements
Metal_Dopant_2	71 different metal elements or none
Metal_Dopant_3	71 different metal elements or none
Metal_Dopant_4	71 different metal elements or none
Metal_Dopant_1 Proportion in Precursor（at. %; refers to that in total four types of metal）	50~100
Metal_Dopant_2 Proportion in Precursor（at. %）	0~50
Metal_Dopant_3 Proportion in Precursor（at. %）	0~33.33
Metal_Dopant_4 Proportion in Precursor（at. %）	0~25
Hydrothermal Temperature (℃) (or precursor mixing)	25~60
Hydrothermal Time (min) (or precursor mixing)	360~1,440
Hydrothermal Still/Stirring (0/1) (or precursor mixing)	0: still incubation; 1: stirring or sonication
Hydrothermal Strong Reductant in Liquid (0/1) (or precursor mixing)	0: False; 1: True
Hydrothermal Weak Reductant in Liquid (0/1) (or precursor mixing)	Constant; 0: False
Mixed in Solid or Liquid (0/1)	0: False (liquid mixing or hydrothermal); 1: True (ball milling)
Annealing Temperature (℃)	Constant; set to 400 and 500 manually
Annealing Time (min)	Constant; 360
Annealing Still/Stirring (0/1)	Constant; 0: False
Annealing Atmosphere Inert (0/1)	Constant; 0: False
Annealing Atmosphere Reducing (0/1)	Constant; 0: False
Post-processing Acid Wash, etc. (after annealing; 0/1)	0: False; 1: True
Catalyst Loading (mg cm^{-2})	Constant; 0.5
Support Material Loading (mg cm^{-2})	Constant; 0
Support is not Carbon (support material, TiOx, etc.; 0/1)	Constant; 0: False
Electrode Type_Glassy Carbon/Carbon Paper or Ti Mesh (0/1)	Constant; 0: Glassy Carbon
LSV Scanning Speed (mV s^{-1})	Constant; 10
Electrolyte Proton Concentration (M)	Constant; 1

Note:
It is noteworthy that in the GA search process, each of the two (database-based committees) ×2 (400 ℃ or 500 ℃) ×2 (Weighted: Maximum Uncertainty or Lowest Predicted Overpotential) =eight types of suggestions which are randomly obtained 48 times per iteration. From these 48 suggestions, one-sixth, i.e., eight, are randomly selected further for experimental synthesis and testing. This means each iteration should have 8*8=64 data points. However, in the first to third iterations, some samples synthesized according to the ML committee exhibited poor OER performance and almost no catalytic activity, and the polarization curves could not reach 10 mA cm^{-2}. This is why in the online repository's experimental data records, as readers can see in **Fig. 4G**, only 34, 39, and 52 data points are available for the first, second, and third iterations, respectively, because the remaining data points among the 64 samples were unusable (due to poor performance). By the fourth iteration, all 64 ML-recommended synthesized samples could at least measure η_{10}. From this perspective, the proportion of effective experimental engineering parameter suggestions from the ML committee increased from 53% to 61%, 81%, and finally 100% in the fourth iteration, reflecting the ML committee's increasing ability to effectively guide experiments in the active learning loop. For the fifth iteration, it was no longer necessary to continue the DASH iteration; therefore, we only used the ML committee to search for the lowest overpotential, resulting in 32 outcomes (excluding the prediction of maximum uncertainty from the first four iterations). We found that all 32 ML-recommended synthesis formulations could successfully test the η_{10} data.
Moreover, as mentioned in main text, while we have confirmed through data mining that Ru is the promising element, we have also set an additional constraint in the GA searching process that Ru must be included as one of the four elements in the selection group. To be noted, Ru is not forced to be the primary metal, but is free to be placed from the first to the fourth place in the dopant order. This would significantly reduce the searching space, and the recipes given by our workflow are likely to be more meaningful and show OER activity in experimental synthesis and evaluations. For more details and parameter settings, please refer to the script in this section, available in the "Active Learning Loop&GA Prediction" directory of our GitHub repository. Also, the full record of the 5 batches of the 320 experimentation trials could be obtained from the online repository "Experimental Records and Raw Data/ AL Full Experimental Records.xlsx".

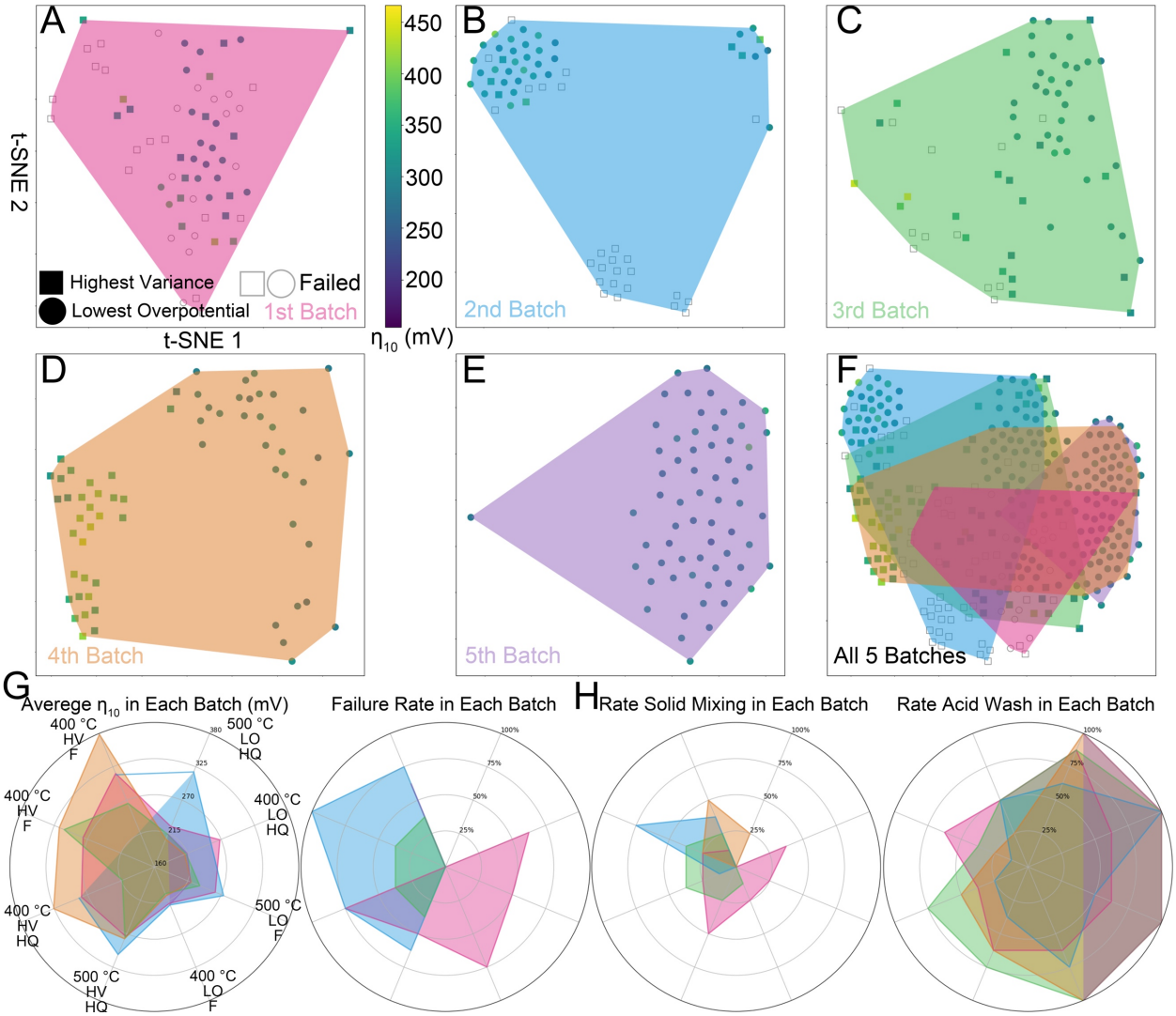

Fig. S18 Exploration and outcomes of AL-guided experimentation batches using t-SNE and performance metrics. (A)-(F) t-SNE plot of the samples in each experimentation batch of the AL-guided experimentation exploration section. Square marks represent 50% of the 64 experimental trials in each batch, which were allocated to recipes suggested by the ML committee for maximizing variance, targeting high uncertainty regions. Circle marks denote the remaining 50% budget, focusing on minimizing overpotential, aiming for superior performance outcomes. All 320 data points, comprising 64 trials per batch over 5 batches (with 258 successful trials, as shown in **Fig. 4G**, and 62 failures), were processed using consistent t-SNE dimensionality reduction settings to ensure a fair comparison. (G) is a web/radar plot that breaks down the average η_{10} values measured and failure rates for each batch across eight different sub-categories described in the **Methods** section. "LO" and "HV" are used as abbreviations for "Lowest Overpotential" and "Highest Variance" respectively; "F" and "HQ" are used to indicate whether the committee started from the full dataset or the high-quality dataset. Similarly, (H) is a plot that shows in each batch, the rate percentages in different subcategories that have chosen to adopt solid mixing precursor (instead of mixing precursor in liquid phase) or chosen acid wash as post-processing after annealing.

Note:
Through the above **fig. S18A-D**, we first use t-SNE to project sample points into a two-dimensional space for visualization, based on their 54-dimensional encoded inputs (**Fig. SN 1-1** in **Supplementary Note 1**). In the 1st batch in **fig. S18A**, we observe that failed samples, represented by gray hollow markers, are uniformly intermixed with successful samples, making separation challenging. Hence, in the 1st batch, the ML committee's prediction made are validated by experimentation relatively poorly. However, when proceeding to the 2nd and the 3rd batch, it is clear that the failed samples are gradually clustered together and separated from the successful samples especially the samples with 50% budget spent on exploitation for lowest overpotential. Proceeding to the 4th batch (**fig. S18D**), the clustering differences between the samples for exploitation and exploration are further clearly separated, with the former obviously having lower overpotentials (judged by colormap). Finally in **fig. S18F**, we could observe through the iterations, how each batch evolves themselves. The majority of failed samples are for exploration, namely with the highest variance, these points generally locate themselves in the bottom-middle corner, and also extend partially toward the center and upper right areas. Interestingly, we could observe that in the 4th batch, the ML committee has learned to avoid such zones, by placing samples with the lowest overpotential on the right canvas, and the highest variance on the left canvas, leaving a big blank in the middle to avoid failure zone. Finally, in the 5th batch, as all our budget is used for exploitation to give us the best samples with the lowest overpotential values, the ML committee learns to locate the points in a relatively small region in the middle right corner, which likely correspond to the possible optimums. This visualization provides deep insights into the robustness of our strategy, demonstrating how the approach evolves iteratively to avoid "dead zones" and strategically focuses on promising regions, validating the effectiveness of our method.
We also use radar plots to further break down our observations into subcategories as shown in **fig. S18G**. The η_{10} values for samples aimed at exploring the highest variance (represented by the four directions in the left half of the radar plot) are significantly higher than those aimed at achieving the lowest overpotential (the four directions in the right half), showing a clear distribution pattern. Over iterations, while uncertainty-aiming samples are getting larger average η_{10} values, the trend for lowest overpotential-aiming samples are in the opposite direction, as we have presented in the violin plots of **Fig. 4G**. This indicates that through the iteration process, our ML agent has effectively learned both how to optimize our target function and more effectively explore uncharted area with the same amount of budget. However, it should also be noted that although failure mostly happens for highest variance samples, its failure rate is decreasing (failure rate is 0% for 4th batch). This further validates the effectiveness of our ML committee; it would soon learn to avoid waste budget on meaningless regions.
Finally, through **fig. S18H**, we checked certain intuitive features in the encodings. Two typical ones are whether to choose mixing precursors in solid phase, and whether to apply acid wash post-processing process after annealing. For the former, it is observed that the percentage of choosing this synthesis technique changes significantly over iterations. The ML committee gradually learns that solid-phase precursor mixing is not preferred for pursuing the lowest overpotential, resulting in all samples in the 5th batch using liquid-phase precursor mixing. As for applying acid wash, the trend is opposite: after the first 2 batches, all the samples aiming to achieve the lowest overpotential would choose to apply acid wash after annealing. In the 4th and the 5th batch it is 100%. This observation is consistent with field knowledge. Liquid-phase mixing facilitates better homogeneity and uniformity in catalyst precursors, leading to materials

with more consistent particle size and dispersion, which enhance catalytic performance (*125, 126*). Similarly, acid washing enhances catalytic effectiveness by removing impurities and unstable species of oxides, thereby increasing the exposure of active sites and improving the material's surface area (*127*). In all, we could use this as a secondary proof that the ML committee has learned through feedback of some chemistry and material common sense to better fulfill its tasks.

The full record of the 5 batches of the 320 experimentation trials could be obtained from online repository directory “Experimental Records and Raw Data/ AL Full Experimental Records.xlsx”. Related details of implementation are provided through **Supplementary Note Discussion SND 3-2** in **Supplementary Note 3**.

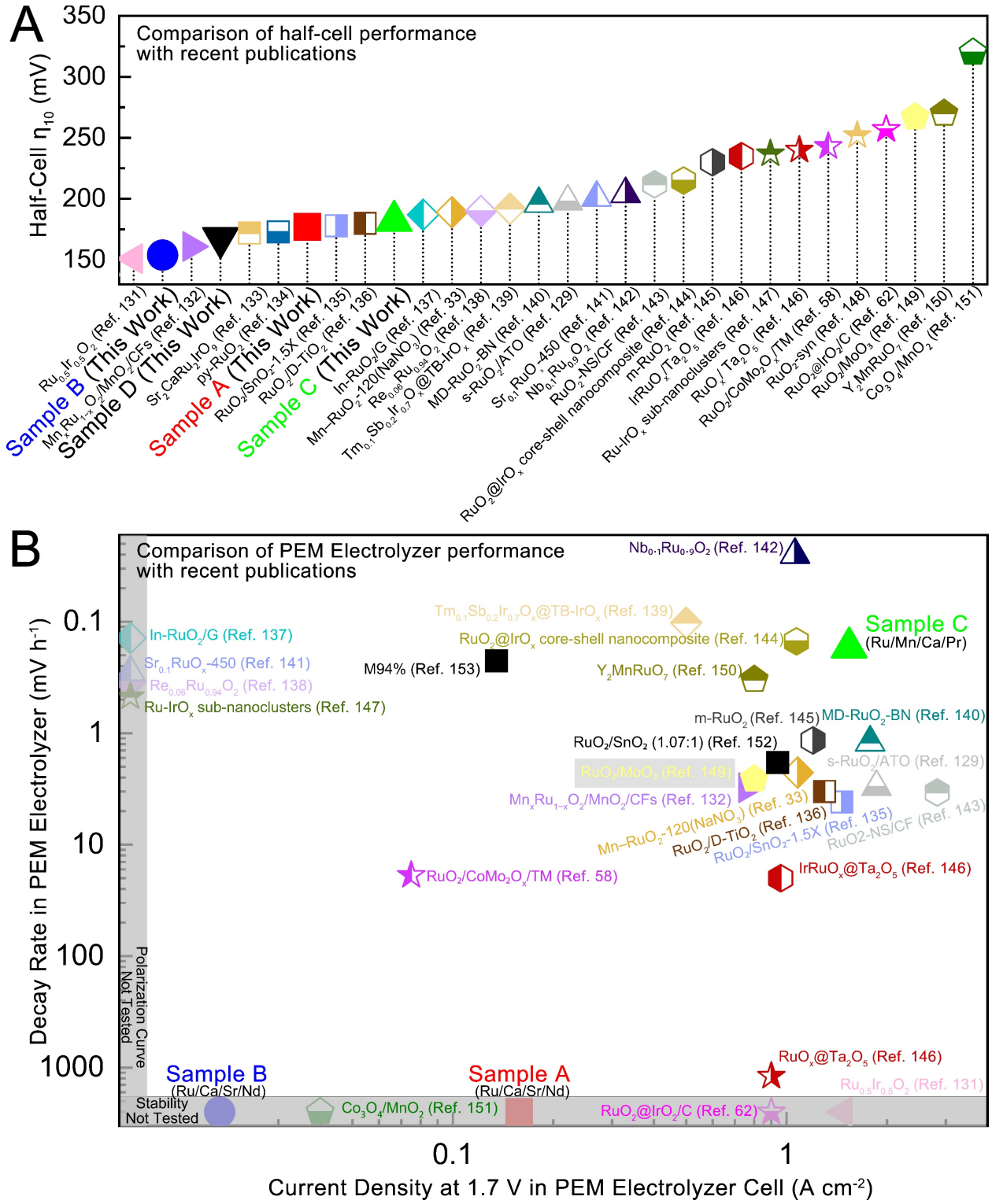

Fig. S19 Performance comparison of OER electrocatalyst samples with recent literature data. (A) Comparison of the samples obtained through this work's multi-ML framework: A, B, C, and D, with recent literature data. (B) similar comparison in PEM electrolyzer with recent literature data in both decay rates and current densities. Original data for (A) and (B) are available in **Table S4** below**.**

Table S4 Summary of recent literature performances of acidic OER electrocatalysts in both half-cell and PEM electrolyzer full cell (Qualitative assessments of cost and synthetic complexity: "Cost" and "Complexity", are categorized into three levels: Low, Medium, and High. These assessments are based on relative comparisons informed by common practices and insights from the field, detailed further in Supplementary Note 5).

Sample Name	Half-Cell η_{10} (mV)	Current Density at 1.7 V in PEM Electrolyzer Cell (A cm^{-2})	Decay Rate in PEM Electrolyzer (mV h^{-1})	(Constant Current) Stability Testing Time in PEM Electrolyzer (h)	Cost	Compl-exity	Publication Year/In our ML Dataset	Ref.
CTr	84	-	-	-	High	High	2022/Yes	*(128)*
s-RuO_2/ATO (pH=2)	89	-	-	-	Low	Medium	2022/Yes	*(129)*
n-RuO_2/ATO (pH=2)	113	-	-	-	Low	High	2022/Yes	*(129)*
α-Fe_2O_3–NiO/CNT	128	-	-	-	Low	High	2022/Yes	*(130)*
$K_{0.05}Sr_{0.95}RuO_3$	138	-	-	-	Medium	Medium	2022/Yes	*(65)*
$Ru_{0.5}Ir_{0.5}O_2$	151	1.48	-	-	Medium	Medium	2023/No	*(131)*
B	**154**	**0.02**	**-**	**-**	**Low**	**Low**	**2023 Jan.**	***This Work***
$Mn_xRu_{1-x}O_2/MnO_2$/CFs	161	0.763	3.08	24	Medium	High	2024/No	*(132)*
D	**168**	**-**	**-**	**-**	**Low**	**Low**	**2023 Jan.**	***This Work***
$Sr_2CaRu_2IrO_9$	172	-	-	-	Medium	High	2024/No	*(133)*
py-RuO_2	173	-	-	-	Low	Low	2023/No	*(134)*
A	**177**	**0.158**	**-**	**-**	**Low**	**Low**	**2023 Jan.**	***This Work***
RuO_2/SnO_2-1.5X	178	1.465	4.14	29	Low	High	2023/No	*(135)*
RuO_2/D-TiO_2	180	1.3	3.33	6	High	Medium	2022/No	*(136)*
C	**182**	**1.54**	**0.17**	**125**	**Low**	**Low**	**2023 Jan.**	***This Work***
In-RuO_2/G	187	-	0.14	350	Low	Medium	2024/No	*(137)*
Mn–RuO_2-120($NaNO_3$)	189	1.08	2.25	90	Medium	Medium	2024/No	*(33)*
$Re_{0.06}Ru_{0.94}O_2$	190	-	0.35	200	High	Low	2023/No	*(138)*
$Tm_{0.1}Sb_{0.2}Ir_{0.7}O_x$@TB-$IrO_x$	192	0.5	0.102	500	High	Medium	2024/No	*(139)*
MD-RuO_2-BN	196	1.78	1.21	24	Medium	Medium	2024/No	*(140)*
s-RuO_2/ATO	198	1.86	3.03	38	Low	Medium	2022/Yes	*(129)*
$Sr_{0.1}RuO_x$-450	201	-	0.283	240	High	Low	2024/No	*(141)*
$Nb_{0.1}Ru_{0.9}O_2$	204	1.06	0.025	360	High	Low	2023/No	*(142)*
RuO_2-NS/CF	212	2.827	3.4	10	Medium	Medium	2021/No	*(143)*
RuO_2@IrO_x core-shell nanocomposite	215	1.07 (extrapolated)	0.15	300	Medium	Medium	2020/No	*(144)*
m-RuO_2	230	1.2	1.16	100	High	Low	2024/No	*(145)*

$IrRuO_x/Ta_2O_5$	235	0.96	20	1	Medium	Low	2024/No	*(146)*
Ru-IrO_x sub-nanoclusters	237	-	0.47	150	Medium	Low	2024/No	*(147)*
RuO_x/ Ta_2O_5	240	0.9	1193	1	Low	Low	2024/No	*(146)*
$RuO_2/CoMo_2O_x/TM$	243	0.075	18.8	40	Low	Medium	2024/No	*(58)*
RuO_2-syn	252	-	-	-	High	Medium	2024/No	*(148)*
$RuO_2@IrO_2/C$	257	0.9	-	-	Medium	Medium	2023/No	*(62)*
RuO_2/MoO_3	267	0.8	2.58	12	Low	Medium	2023/No	*(149)*
Y_2MnRuO_7	270	0.8	0.33	350	Medium	High	2023/No	*(150)*
Co_3O_4/MnO_2	320	0.04	-	-	Low	Low	2024/No	*(151)*
RuO_2/SnO_2 (1.07:1)	-	0.94	1.83	235	Medium	Medium	2014/No	*(152)*
M94%	-	0.135	0.224	1140	Medium	Medium	2024/No	*(153)*

Supplementary Discussion S3

Comparison with Recent Reports

As we have summarized in the above **Table S4** and **fig. S18**, a comprehensive comparison of both activity and stability in both half-cell and PEM electrolyzer full cell tests is given. In **fig. S18A**, we managed to collect the η_{10} values from publications published mostly in recent 2 years (2023~2024). As a matter of fact, these data (except for Ref. (*129*)) have not been included in the dataset for the supervised data mining and later the active learning stage. And to be noted, our final samples A~D were discovered in early 2023. Hence, we could tell that, in terms of half-cell performances, our samples A~D are still in the state-of-the-art tier compared with those recorded in the publications after nearly two years, with the overpotential of sample B reaching as low as 154 mV, and that of sample C still competitive at 182 mV.

Moreover, testing acidic OER electrocatalysts within a PEM electrolyzer cell as we have done in **Fig. 4H-I** is crucial because it evaluates their performance under realistic operating conditions, including factors like mass transport, ion conductivity, and mechanical stability. While RDE half-cell tests provide initial insights into catalytic activity, they often fail to replicate the complex environment of a full PEM electrolyzer. Consequently, catalysts that perform well in RDE tests may exhibit reduced efficiency or durability when subjected to the actual conditions of a PEM electrolyzer. Therefore, comprehensive testing in a full-cell setup is essential to accurately assess the practical viability of OER electrocatalysts. We proceed with the comparison and visualization in **fig S18B** for the performances in real PEM electrolyzer cells. As the *y* axis stands for averaged decay rate (though testing current density and testing time for constant current ADT might vary, for intuitive comparison, we still choose to use the change in voltage divided by time as a numeric metric) and *x* axis stands for a fair comparison of the current density at 1.7 V. We could find that for the sample that we claimed as the comprehensively best sample, sample C has shown promising overall performance. Although there are still a few state-of-the-art products that surpass ours either in activity or stability, sample C managed itself to stand in the activity-stability multi-target frontier. With a high intrinsic OER activity comparable to most advanced Ru-based samples, sample C also showed great stability that is comparable to Ir-containing products although its ML-obtained recipe does not contain Ir. Other similar Ru-focused reports would show orders of magnitude worse decay rates in comparison. Such a result has strongly proven that the effectiveness of our multi-stage ML strategy has identified a promising candidate comparable with current state-of-the-art human expert designed products.

Though promising, as we have mentioned in the main text, there are still ~0.5% records in terms of η_{10} values that even sample B could not surpass. Some representative entries in our database from corresponding publications (*65, 128-130*) are also included in **Table S4**. as they have been recorded with very low η_{10} values between 60 and 140 mV. These publications warrant careful scrutiny, as they deviate significantly from established thermodynamic and kinetic expectations for OER catalysts in acidic media. Although a nowadays community consensus that through the typical adsorption evolution mechanism, the limitation of OER overpotential would be 370 mV, the lattice oxygen mechanism (LOM) would breach this limitation (*78-83*). However, based on the foundational study by (*154*) Jong et al., there is still a limit of ~100 mV by LOM. This would be due to the inherent energy gap in forming lattice oxygen intermediates, which cannot be entirely minimized even with the optimal catalyst design.

Discussion of Extreme Data Points

We would also like to briefly discuss the limitations of these studies although extremely low overpotentials are reported:

First, the K-doped $SrRuO_3$ system (*65*) claims performance enhancements through potassium doping and crystallographic modifications; however, the corresponding reported complex wet chemistry synthesis involving multiple precise temperature controls raises concerns about reproducibility and scalability. The incorporation of K^+ ions would also likely increase dissolution risk in acidic environments, compromising long-term stability. Similarly, the reduced columbite-tantalite (CTr) catalyst (*128*) reports an overpotential of 84 mV, but the use of hydrofluoric acid and liquid-liquid extraction in its synthesis is both expensive and environmentally hazardous. Unaccounted IR losses and optimized electrolyte conditions may artificially lower the observed overpotential, rather than reflecting true intrinsic activity. The strained s-RuO_2/ATO system (*129*) achieves a 198 mV overpotential through tensile strain induced by rapid quenching, yet requires a sophisticated metal-organic framework precursor and benefits from increased an electrochemical surface area due to ATO substrates, which can overestimate intrinsic activity improvements. Moreover, the ultra-low entries were obtained by s-RuO_2/ATO in this publication under pH=2 condition in more dilute electrolyte. A reasonable suspicion could be measurement artifacts arising from decreased electrolyte conductivity in more dilute acid, which can lead to insufficient iR compensation and artificially low overpotential readings. Additionally, changes in proton concentration at higher pH may temporarily affect reaction kinetics or surface properties, enhancing apparent catalytic activity without reflecting true intrinsic improvements. The α-Fe_2O_3–NiO/CNT composite (*130*), reporting a 128 mV overpotential has a similar issue. It employs Fe and Ni components that are inherently unstable in acid and relies on precise control of multiple synthesis steps that are challenging to reproduce. The use of carbon nanotube substrates may contribute to enhanced conductivity, capacitance and hence apparent activity, masking the true performance of the catalyst.

Moreover, all these samples are not deployed in a real PEM electrolyzer which is agreed upon by domain experts that would be more challenging than half-cell environments. And with ML workflow's guidance in optimizing recipes, we successfully achieved a credible overpotential of 154 mV in η_{10}, and the 182-mV sample C has also proven promising in a real PEM electrolyzer for practical applicability.

However, from a ML perspective, including these potentially optimistic or questionable data points in our training dataset is acceptable. Even though there is inevitable variance in publication quality and the presence of outliers, our extensive dataset—carefully constructed from over 500 peer-reviewed experimental studies—allows the model to capture nuanced patterns in material synthesis, composition, and structure-property relationships. We have implemented standard procedures for preprocessing, such as addressing missing values and ensuring consistency across the dataset, as we mentioned in **Supplementary Note 1**. Moreover, ML models are inherently robust against noise and can generalize beyond individual inconsistencies through statistical averaging and pattern recognition across multiple parameters. Our past publications built on comprehensive publication datasets have validated the effectiveness of such a methodology multiple times in various similar systems (*27, 123, 155*). While some reported overpotentials may be artificially low to an unusual degree, as we've just discussed, due to unreported testing conditions or measurement artifacts, they still encode valuable information about structural features, electronic properties, and synthesis conditions that contribute to catalytic activity. By systematically including these data points, the model has the ability to effectively filter out experimental artifacts and learn genuine design principles. While

acknowledging the presence of variability and potential outliers within our dataset, the extensive size and careful curation allow our models to extract meaningful patterns. The inclusion of a broad range of data points enhances the models' ability to generalize and predict catalyst performance effectively. Another point to emphasize is that we recognize uncontrolled data may introduce biases. To mitigate this, we employed ensemble learning, committee methods, and cross-validation techniques, which reduce the impact of any single data point or anomalous study on the overall model performance.

In all, we should emphasize the most unshakable fact that the successful prediction and synthesis of catalysts achieving overpotentials as low as 154 mV and 182 mV—promising in multiple frontiers and closely aligned with recent state-of-the-art benchmarks—demonstrate the model's ability to extract meaningful insights even from noisy data, despite certain data variability. Our ML-guided approach thus balances optimal activity with practical reliability, reinforcing the validity of including a diverse range of data in our dataset and underscoring the model's effectiveness in navigating variable experimental conditions to produce catalysts with real, robust performance. Supported by comprehensive stability verification in both half-cell and single-cell configurations, our catalyst design possibly represents a realistic advancement over these human-expert-crafted state-of-the-art samples.

Discussion of Future Industrial Deployment

Finally, for scalability based on synthesis processes, we applied a straightforward one-step mixing and one-step annealing synthesis approach that requires no expensive niche precursors, ensuring high reproducibility, cost-effectiveness, and environmental friendliness. By utilizing readily available metal precursors and common solvents like water and ethanol while avoiding hazardous chemicals, this method is both simple and scalable. The straightforward nature of the process enhances consistency, a critical factor for industrial applications. Potential challenges for scaling up, such as ensuring uniform mixing and consistent thermal conditions across larger batches, are standard engineering issues that might be addressed through well-established industrial solutions like large-scale mixers and controlled atmosphere furnaces, reinforcing the feasibility of large-scale implementation.

To further explore scalability, we plan to conduct pilot-scale synthesis experiments aimed at controlled batch expansion. These trials will involve increasing batch sizes while striving to maintain uniformity in composition and microstructure. Leveraging a mid-scale production line provided by our industrial collaborator, we intend to assess the consistency and reproducibility of the catalyst at intermediate scales. Additionally, we will scale up the synthesis process for preliminary tests in miniaturized electrolyzer stacks, which will simulate industrial conditions while addressing safety concerns such as hydrogen and oxygen crossover. These tests are expected to play a critical role in evaluating catalyst performance in realistic setups and ensuring process viability for industrial adoption.

Looking ahead, we anticipate addressing challenges such as maintaining consistent phase distribution, optimizing heat transfer for larger batches, and preventing contamination during upscaling. Future efforts will also focus on improving MEA assembly for higher current densities, enhancing long-term catalyst stability, and mitigating challenges like ensuring uniform mixing and thermal conditions in larger-scale synthesis batches. Furthermore, we plan to incorporate process automation and advanced quality control techniques into our scale-up strategies to meet industrial standards. These combined efforts will aim to bridge the gap between lab-scale synthesis and full industrial deployment, facilitating a seamless transition from research innovation to practical applications.

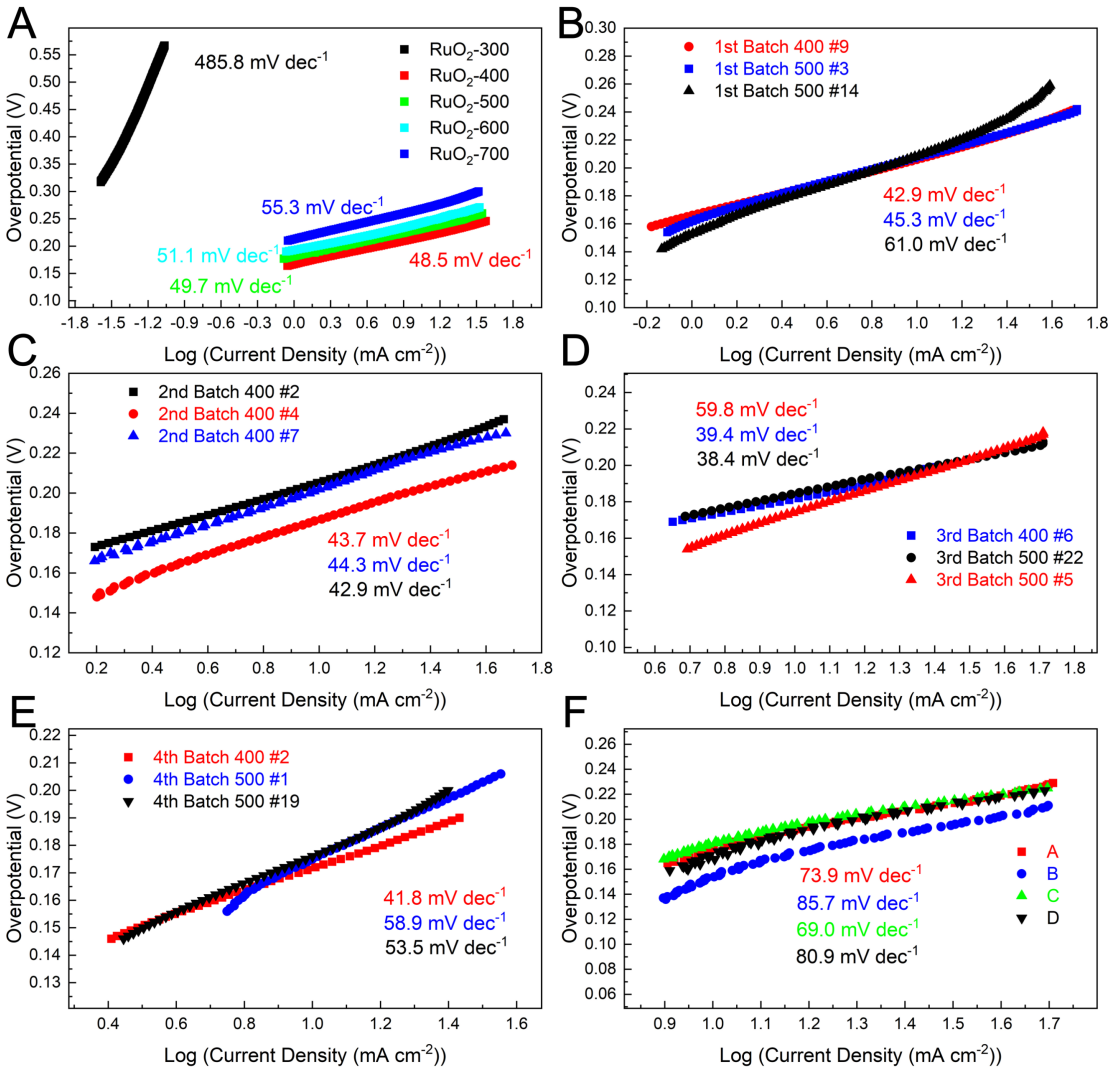

Fig. S20 Tafel plots and kinetic insights into OER electrocatalyst performance across experimental batches. **(A)-(F)** are Tafel plots (around 10 mA cm^{-2}) corresponding to the samples in **Fig. 4**. It could be found that in batches 2, 4, and 5, the Tafel slopes of the samples are not in consistent order of their η_{10} values. The discrepancy between the Tafel slopes in the OER catalysts arises from various factors. Different catalytic mechanisms can lead to a catalyst with a low overpotential while exhibiting a higher Tafel slope, reflecting diverse reaction kinetics. The Tafel slope, indicative of surface-reaction kinetics, contrasts with the overpotential, which relates to the number of active sites. A catalyst with many active sites might not have optimal reaction rates at these sites, resulting in a higher Tafel slope. Additionally, the electrode surface's microstructure and physical properties, along with experimental conditions like pH and temperature, can affect these measurements. This highlights the need for a multi-dimensional approach in evaluating and designing electrocatalysts that considers both the quantity and quality of active sites and their performance under varying conditions. Based on further results in **fig. S21** and **fig. S22**, we could derive that although A, B, and D have advantages on the surface area and the exposure of active sites, which lead to their better overpotential, their kinetics is inferior compared to C. C has a better Tafel slope and specific current density per ECSA, indicating that it has better intrinsic OER activity. $Decade^{-1}$, dec^{-1}.

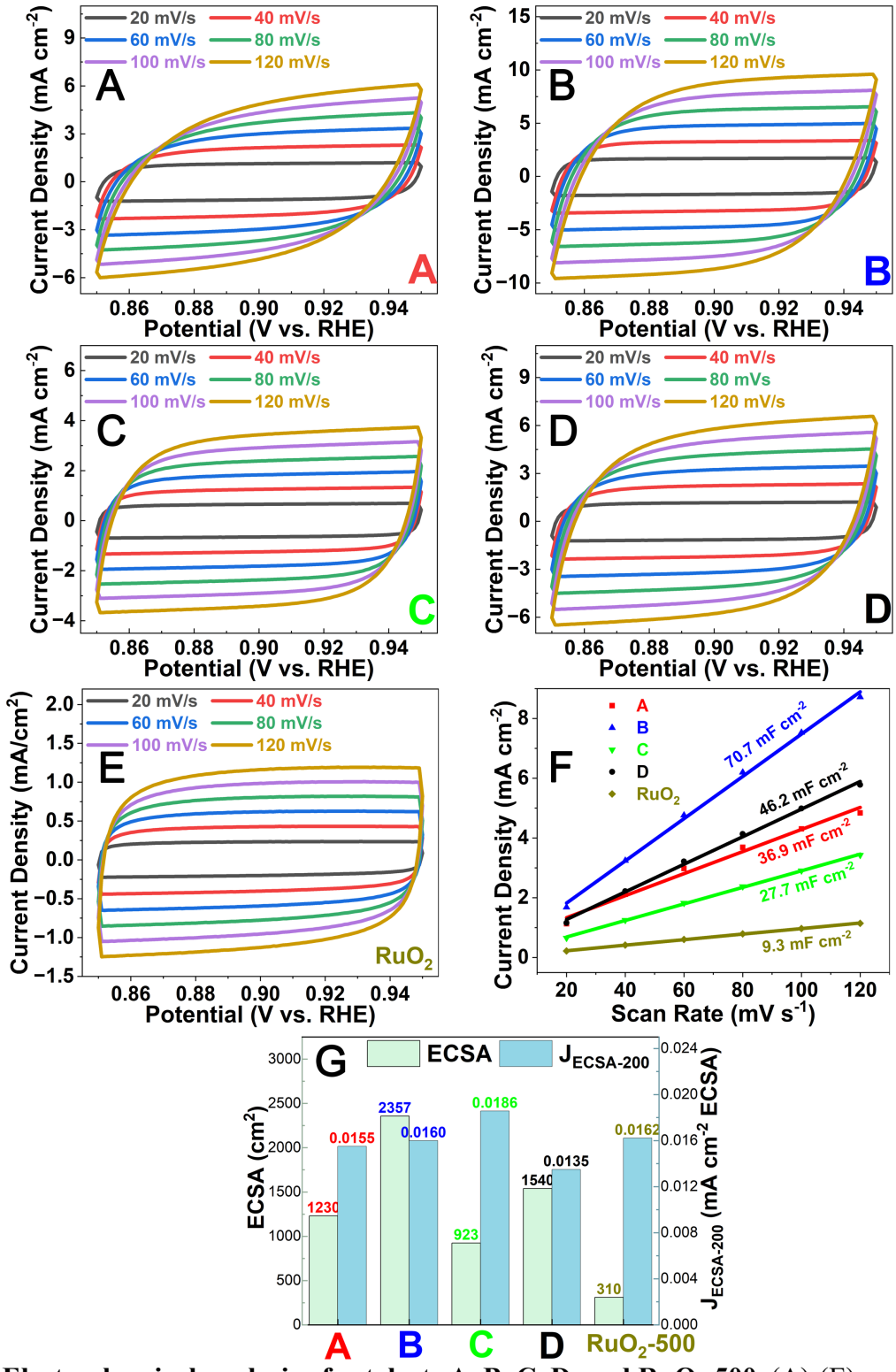

Fig. S21 Electrochemical analysis of catalysts A, B, C, D, and RuO_2-500. (A)-(E) Electrochemical cyclic voltammetry scans recorded for A, B, C, D, and RuO_2-500. Scan rates are 20, 40, 60, 80, 100, and 120 mV/s, respectively. (F) Linear fitting of the capacitive currents versus cyclic voltammetry scans for these catalysts. (G) The calculated ECSA and specific current density per ECSA at η=200 mV ($J_{ECSA-200}$) values for A, B, C, D, and RuO_2-500.

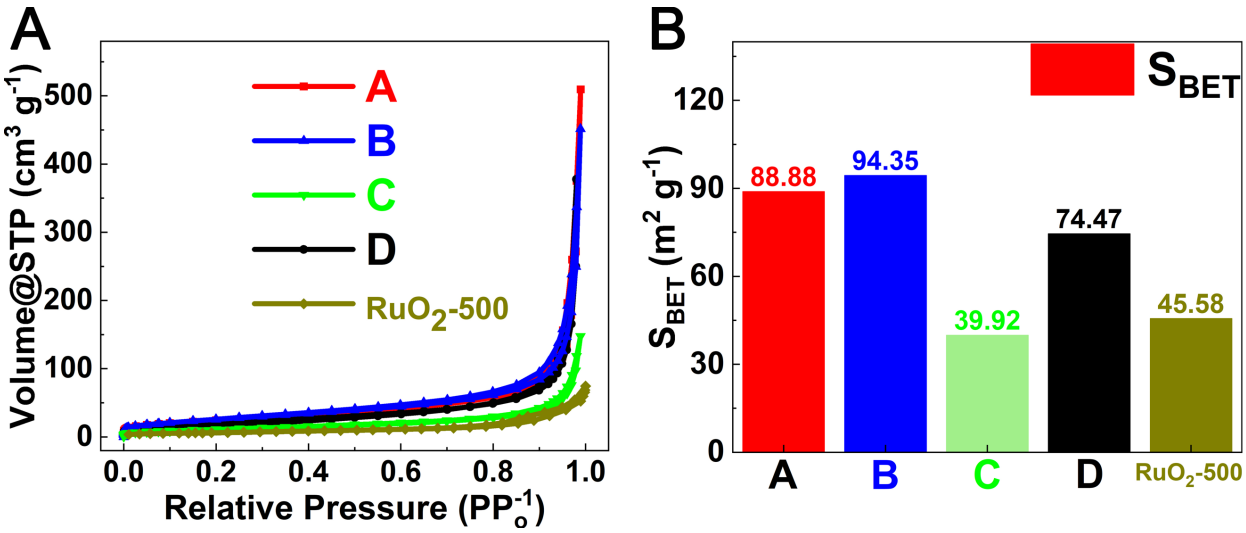

Fig. S22 BET analysis of catalysts A, B, C, D, and RuO_2-500. (A) Typical N_2 adsorption–desorption isotherms for A, B, C, D, and RuO_2-500. (B) Summary of the BET surface area for A, B, C, D, and RuO_2-500.

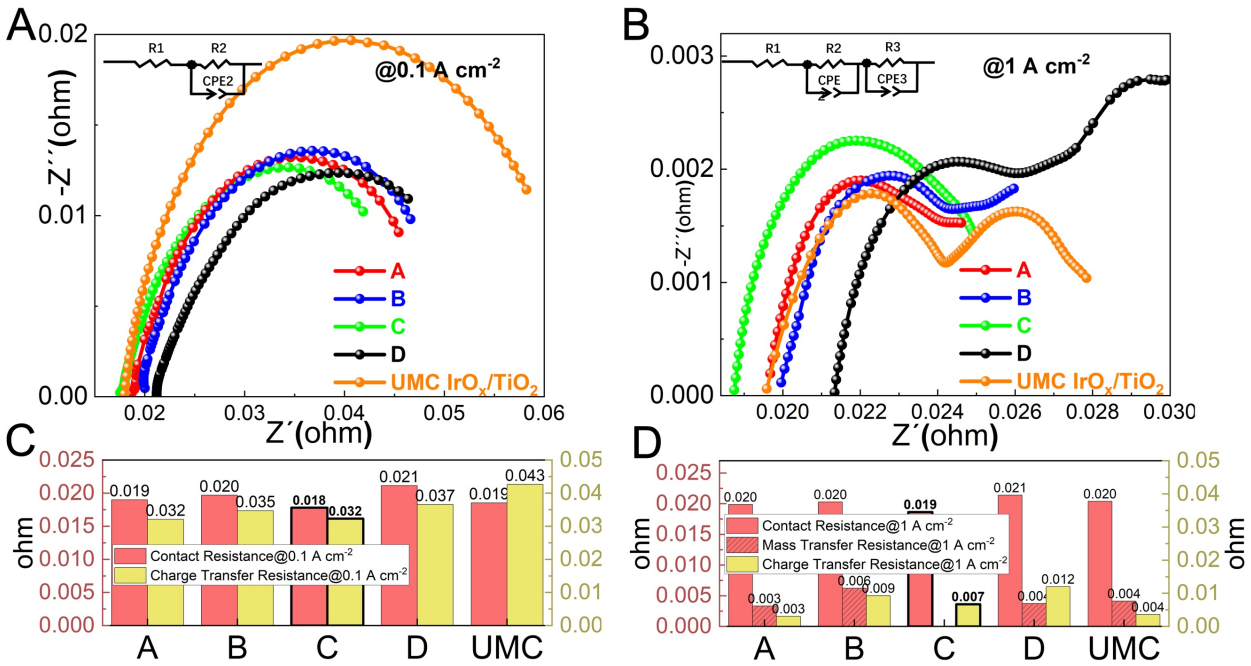

Fig. S23 Electrochemical impedance spectroscopy analysis of MEA samples. (A) and (B) EIS spectra of the MEA samples measured in **Fig. 4H**, at 0.1 and 1 A cm^{-2} current densities, respectively, with their schematic equivalent circuits. (C) and (D) are the analyzed resistance components corresponding to (A) and (B).

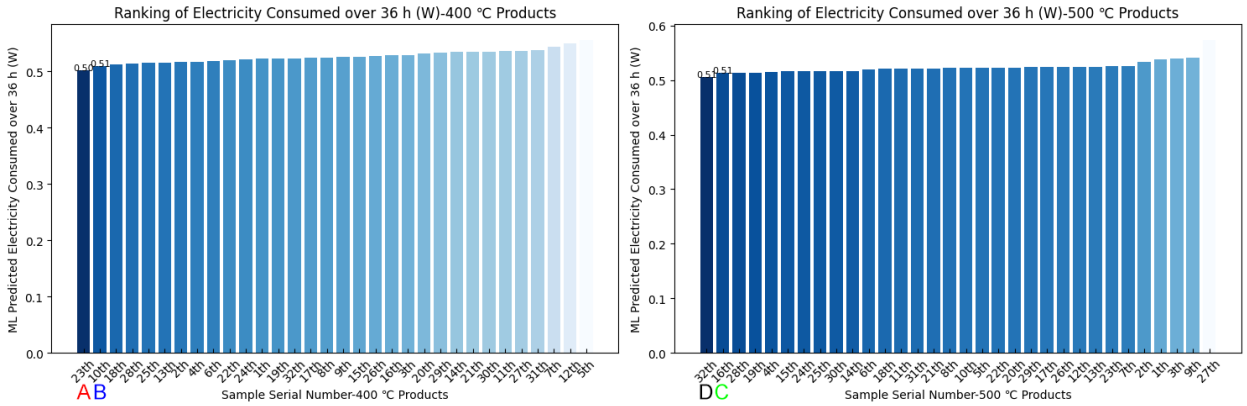

Fig. S24 ML committee predictions of long-term electrocatalyst performance. Results from the direct use of the high-quality domain knowledge-based ML committee to predict the long-term performances of the electrocatalysts. Here, we enter the final samples information in the fifth batch as the input for the stability prediction models to predict the total needed electricity in 36 h while electrolyzing at a constant current density of 10 mA cm^{-2}. We also use a very simple hypothesis: the average voltage decay rate is constant; namely, the voltage needed to maintain the electrolysis current density will only increase linearly with time (overpotential becomes larger over time). As a final result, we found that samples A~D, which had the lowest overpotential, were still predicted to decay at the lowest rate, thus consuming the least amount of electricity in a practical situation. Corresponding script is in directory online: “Half-Cell Stability Quick Predict”.

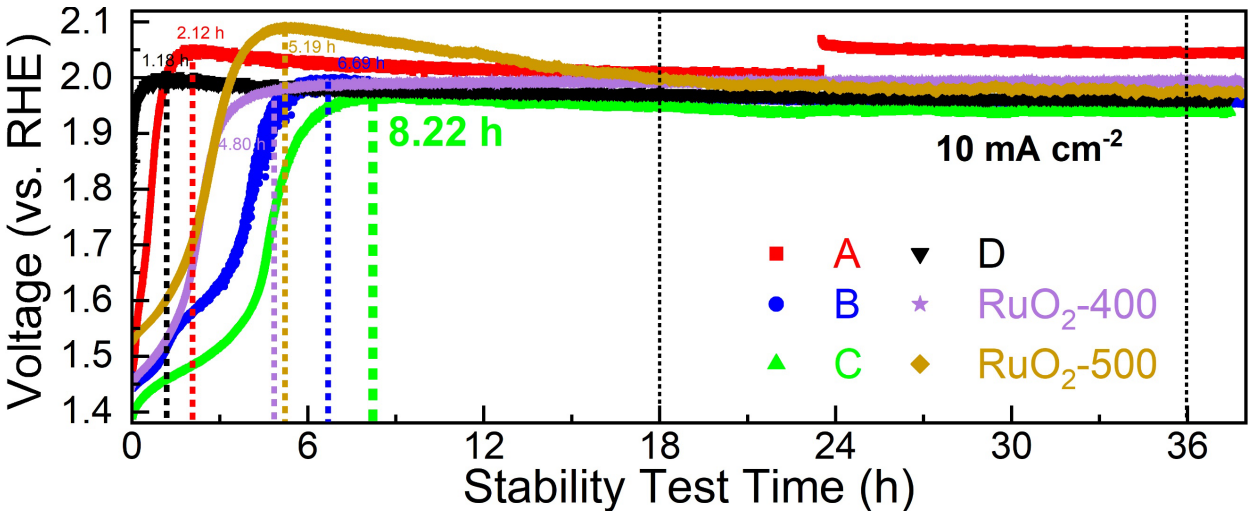

Fig. S25 The stability test in the half-cell of different samples. The dashed line indicates when the voltage is recorded to reach the maximum values. Sample C took 8.22 hours, while other samples generally failed quickly. Moreover, the final voltage of sample C is also lower.

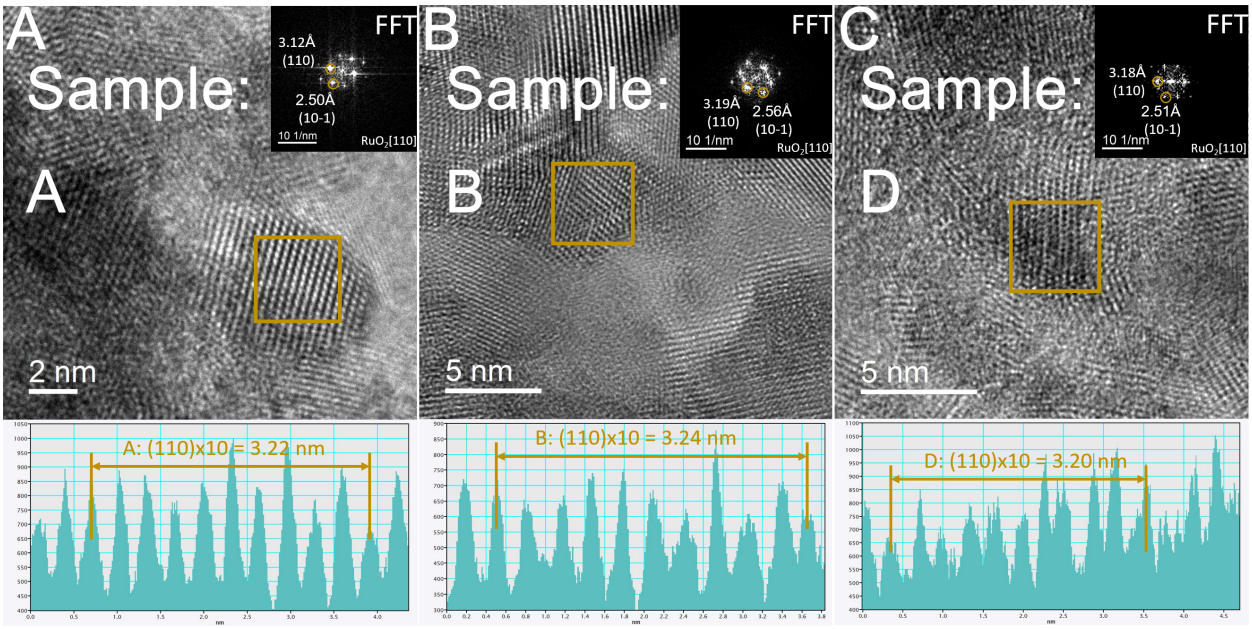

Fig. S26 High-resolution TEM analysis of samples A, B, and D. Similar to **Fig. 5A-B**, here we present the high-resolution TEM images, selected area FFT diffraction patterns, and corresponding statistical analysis of the average interplanar spacing. (A) for sample A; (B) sample B; (C) sample D.

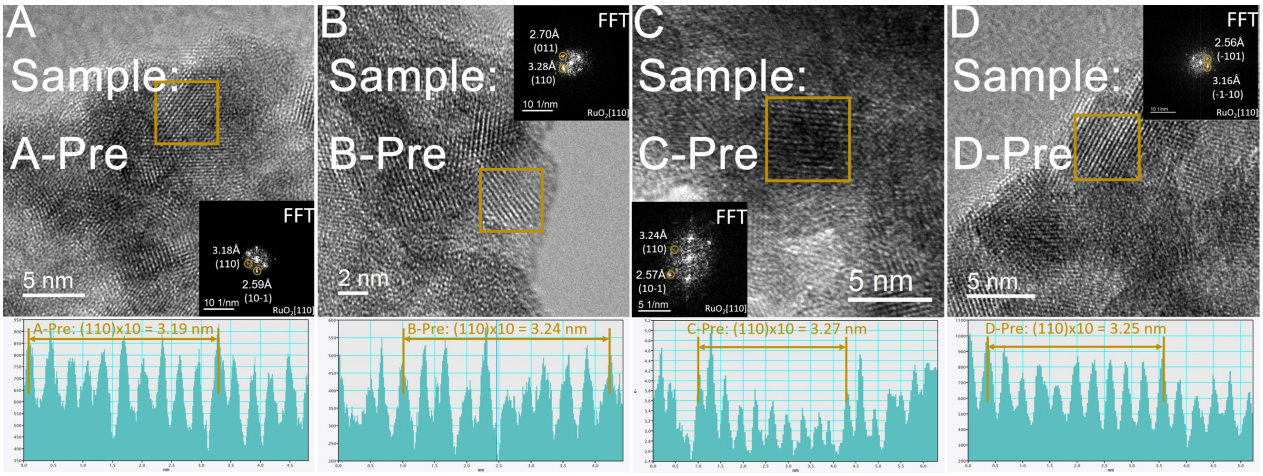

Fig. S27 High-resolution TEM analysis of pre-treated samples A-Pre, B-Pre, C-Pre, and D-Pre. High-resolution TEM images, selected area FFT diffraction patterns, and corresponding statistical analysis of the average interplanar spacing. (A) for sample A-Pre; (B): sample B-Pre; (C) sample C-Pre; (D): sample D-Pre.

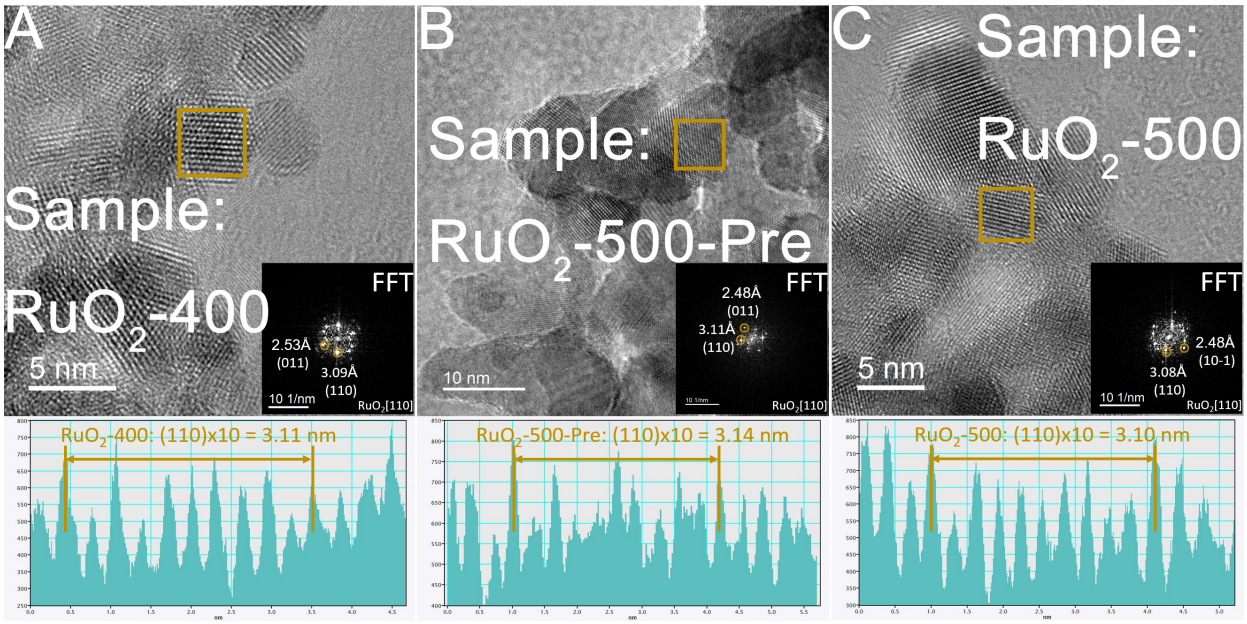

Fig. S28 High-resolution TEM analysis of RuO_2 samples. High-resolution TEM images, selected area FFT diffraction patterns, and corresponding statistical analysis of the average interplanar spacing. (A) for RuO_2-400; (B) for RuO_2-500-Pre; (C) for RuO_2-500.

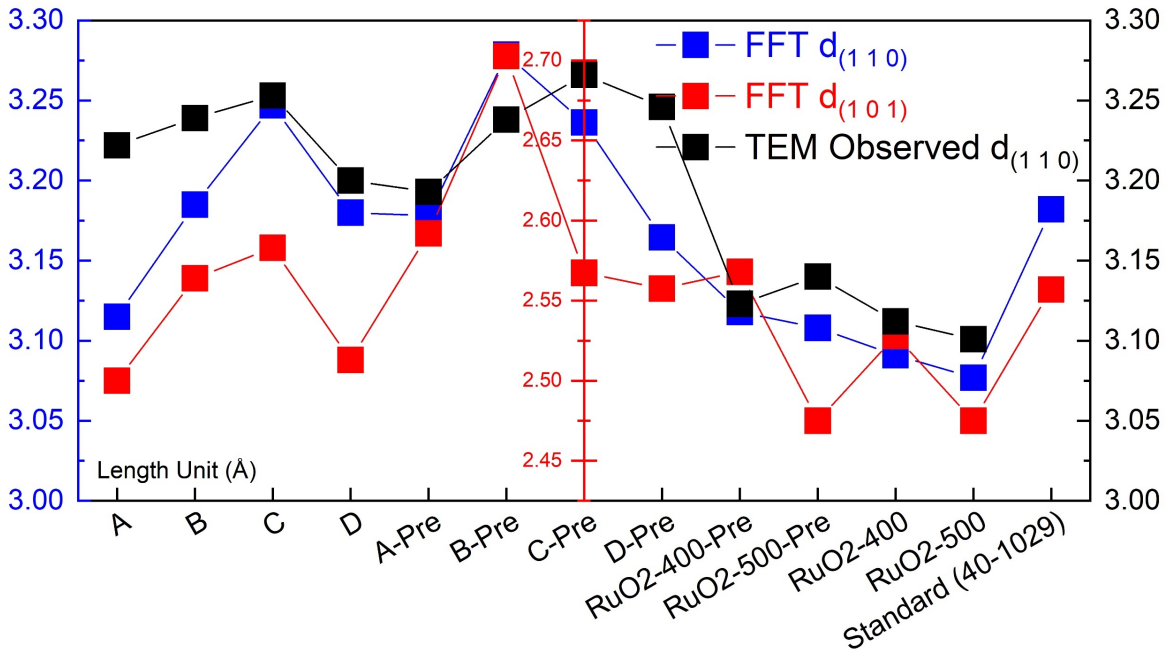

Fig. S29 Statistical analysis of interplanar spacings for RuO_2 crystalline particles. The statistical line graph of the interplanar spacings for the (110) and (101) planes calculated from the inverse space diffraction patterns obtained through selected area FFT transformation, and the average (110) plane spacing directly measured in the selected areas of the TEM images for different samples of RuO_2 crystalline particles.

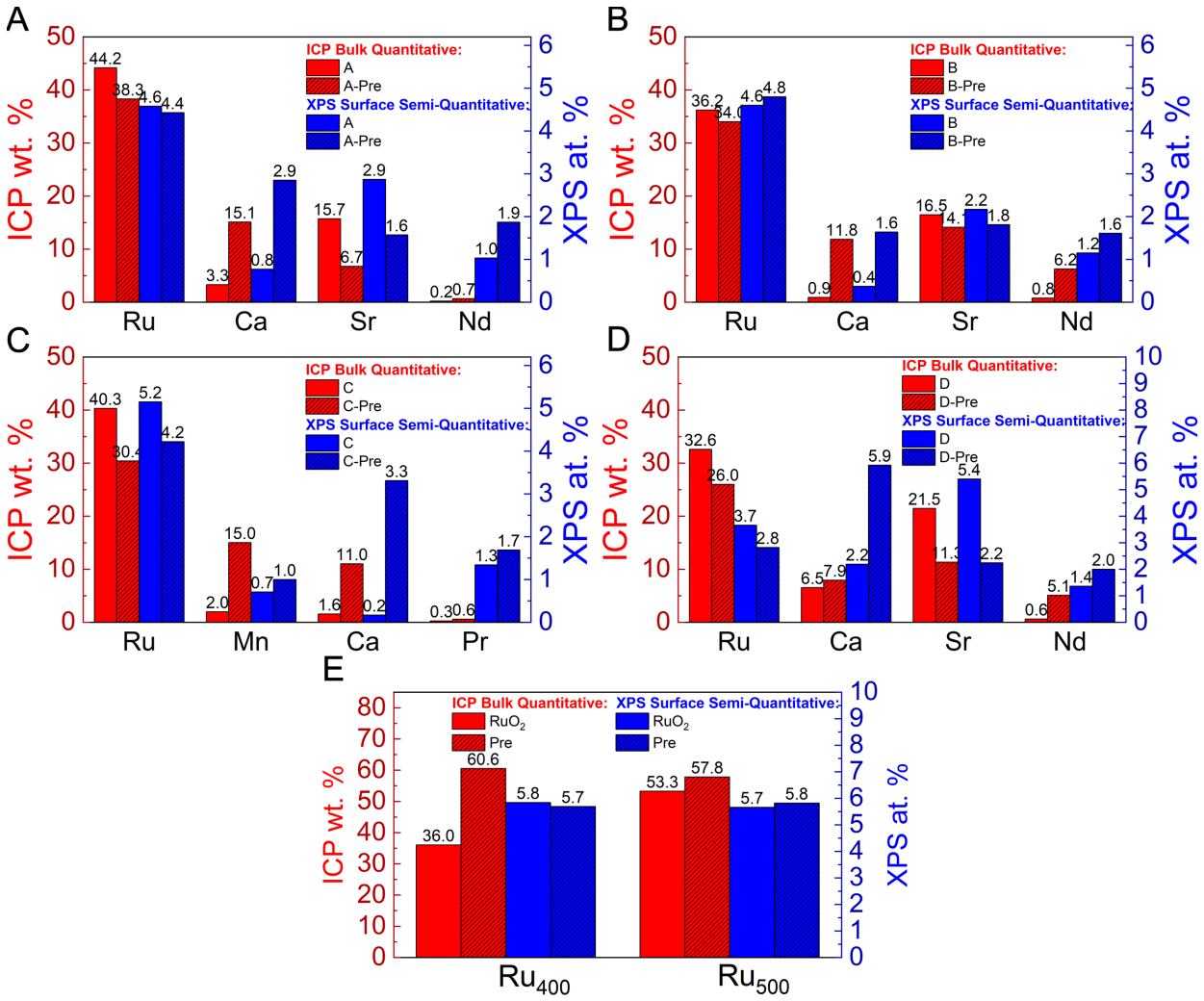

Fig. S30 ICP and XPS characterization statistics. (A)-(E) The bar chart showing the quantitative bulk mass fractions of various metal elements in 12 different samples obtained through ICP testing, and the semi-quantitative surface atomic fractions derived from XPS spectra.

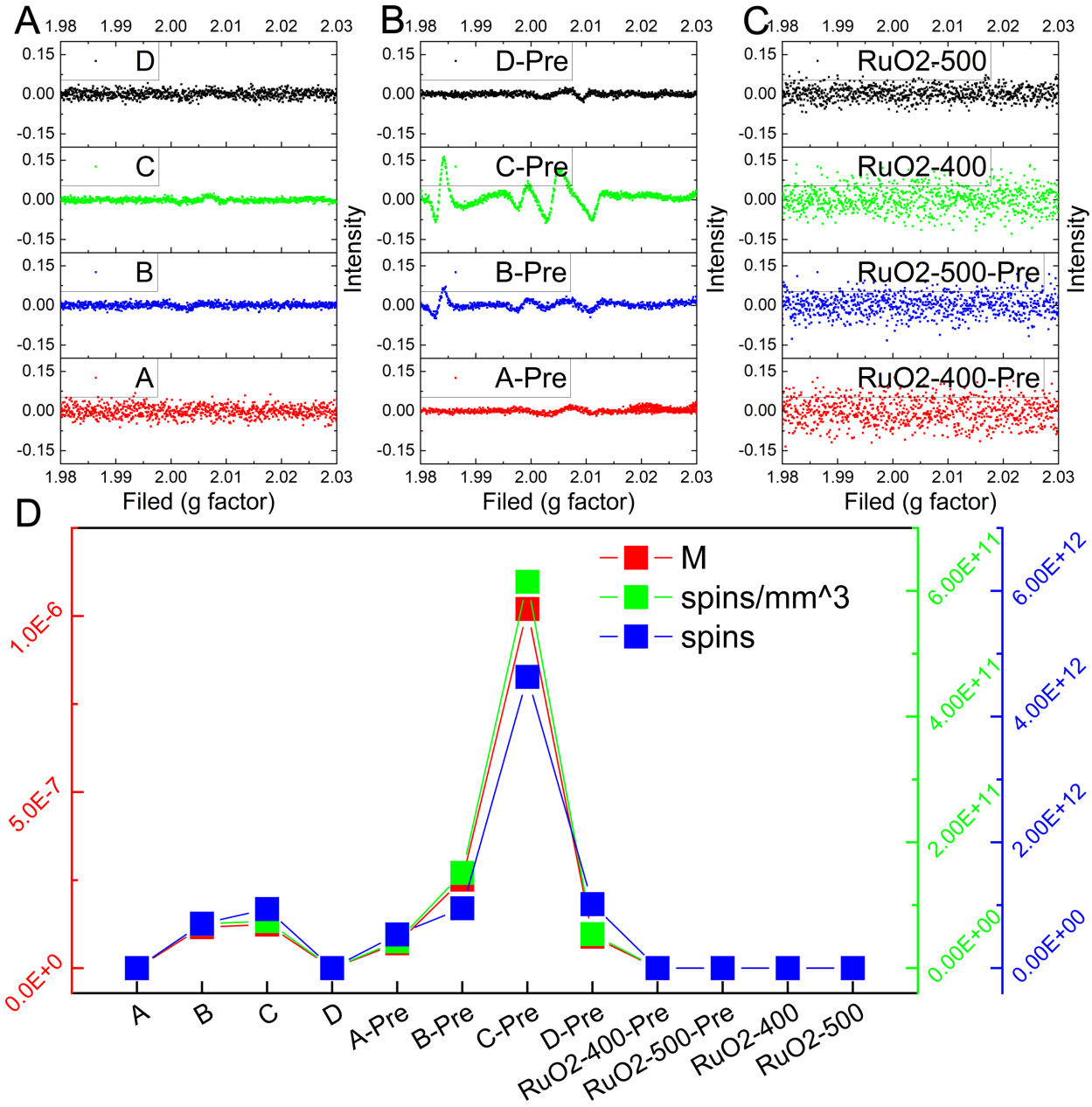

Fig. S31 EPR spectra and magnetic susceptibility analysis of samples. (A)-(C) EPR spectra of 12 different samples, with the g-factor as the horizontal axis. (D) Statistical line graph of magnetic susceptibility (M), in terms of total spins and spins per cubic millimeter (spins/mm^3) for different samples.

The data clearly shows that the C-Pre sample exhibits a high intensity of M, spins per cubic millimeter, and total spins, whereas all other samples exhibit significantly lower signal levels. This observation suggests that C-Pre contains manganese oxides, contributing to its strong magnetism due to the element composition of Ru, Mn, Ca, and Pr. However, upon observing C, the signal significantly diminishes, indicating the successful removal of manganese oxides during the acid wash process. Consequently, the remaining Mn element in C is inferred to be doped into the lattice of the primary RuO_2 matrix.

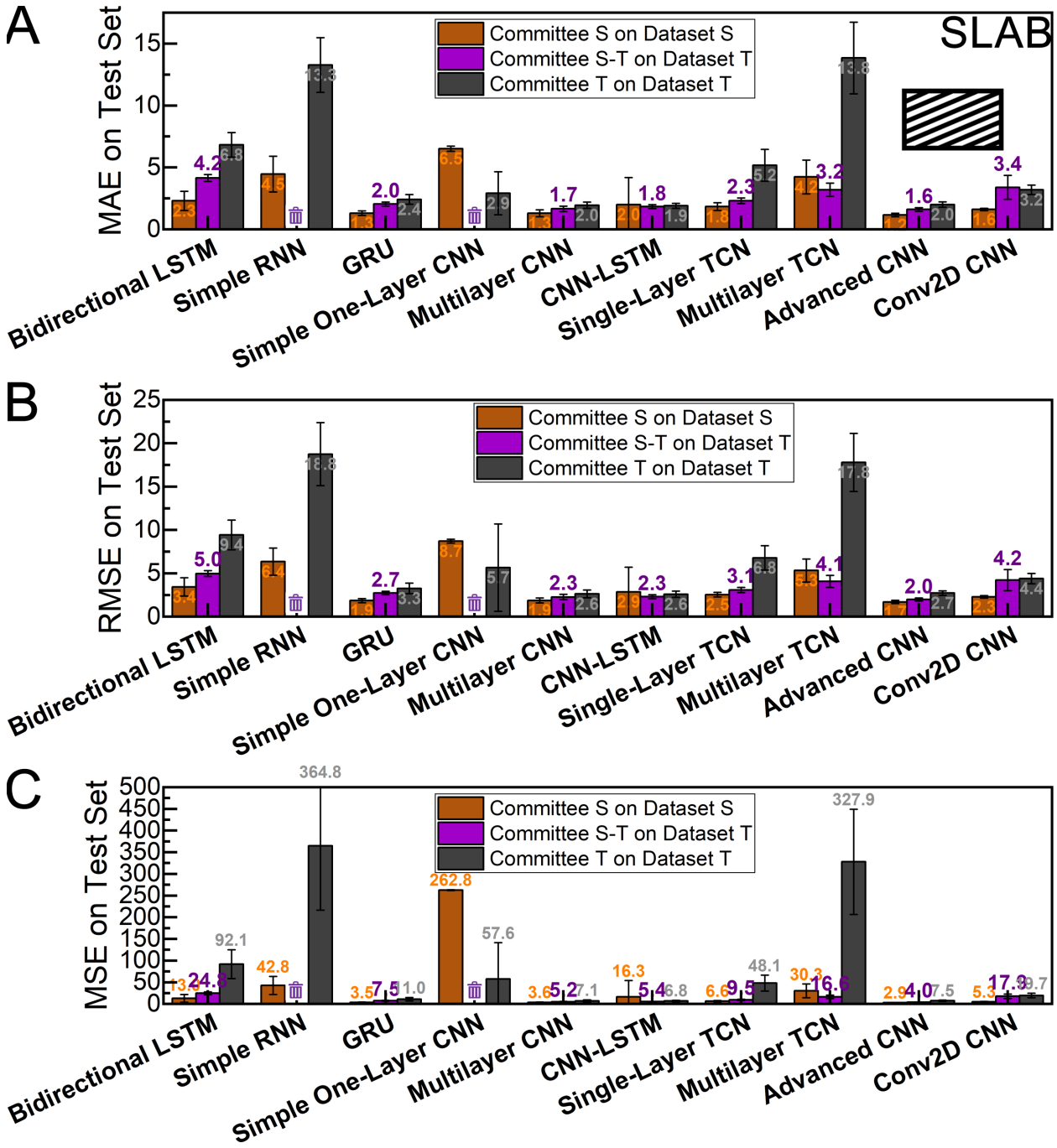

Fig. S32 Summary of the regression performance metrics of the committee predicting the energy of the slab. (A-C) are histograms to visualize the difference between different committee members on different datasets.

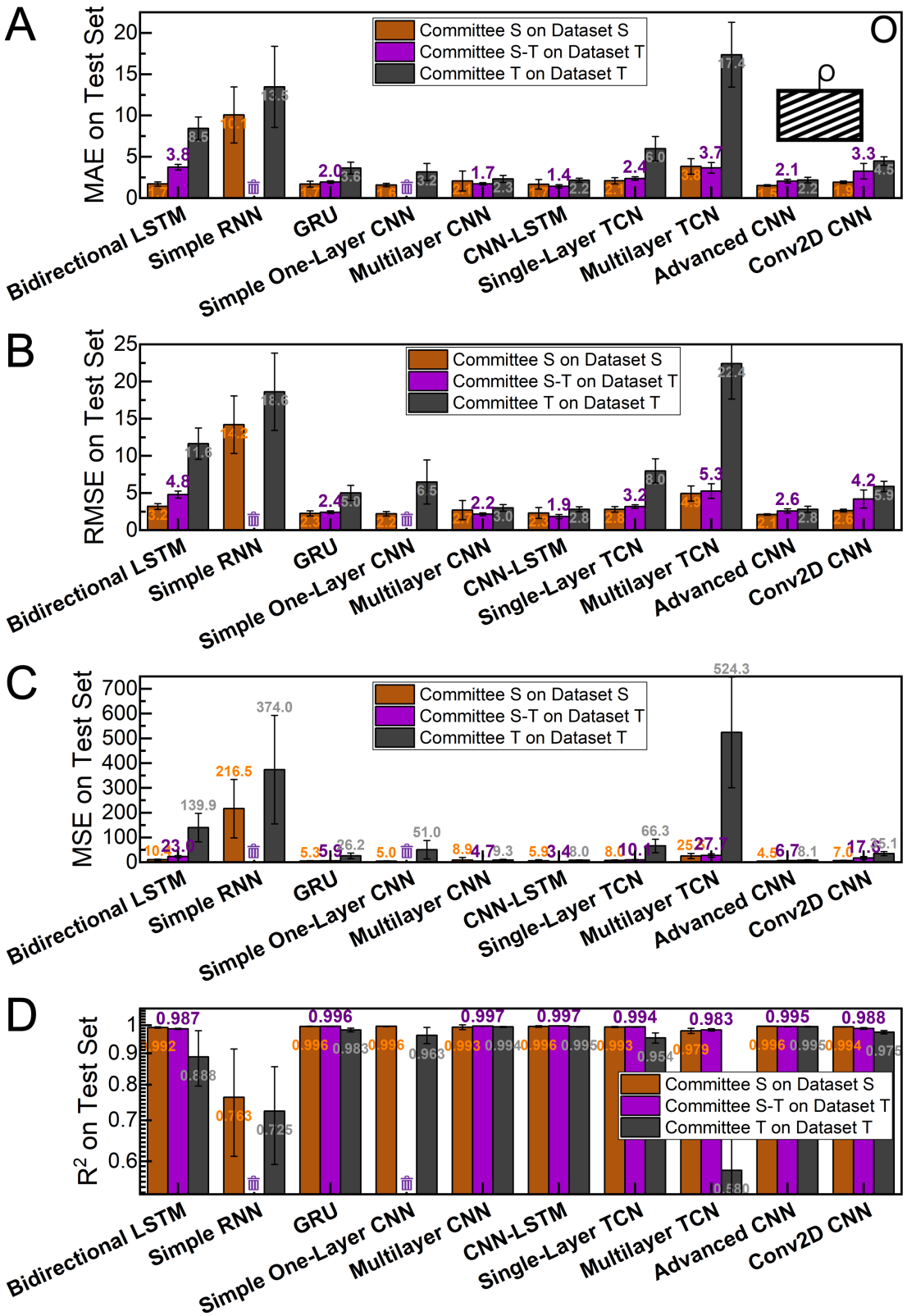

Fig. S33 Summary of the regression performance metrics of the committee predicting the energy of the slab with O species adsorbed. (A-D) are histograms to visualize the difference between different committee members on different datasets.

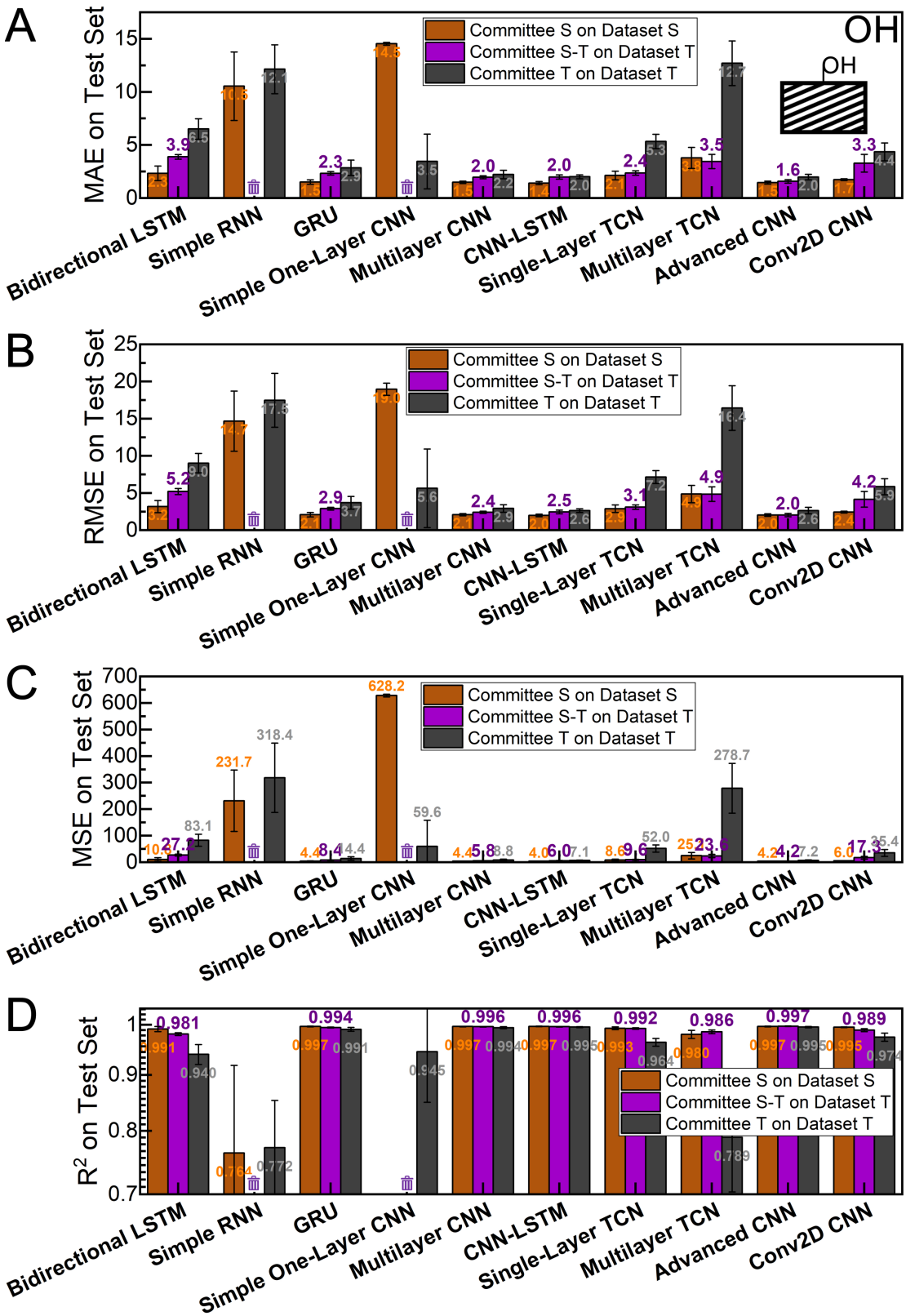

Fig. S34 Summary of the regression performance metrics of the committee predicting the energy of the slab with OH species adsorbed. (A-D) are histograms to visualize the difference between different committee members on different datasets.

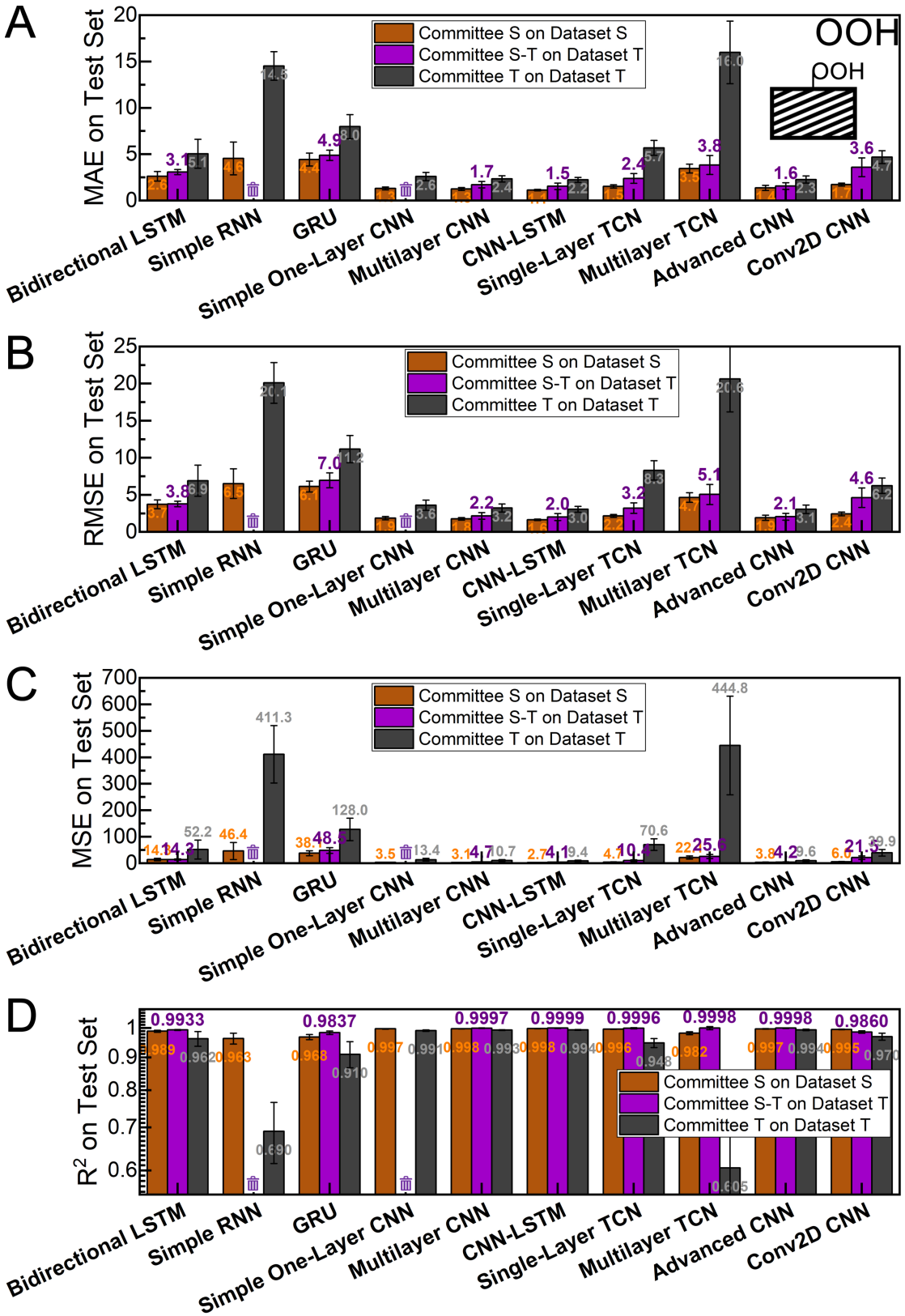

Fig. S35 Summary of the regression performance metrics of the committee predicting the energy of the slab with OOH species adsorbed. (A-D) are histograms to visualize the difference between different committee members on different datasets.

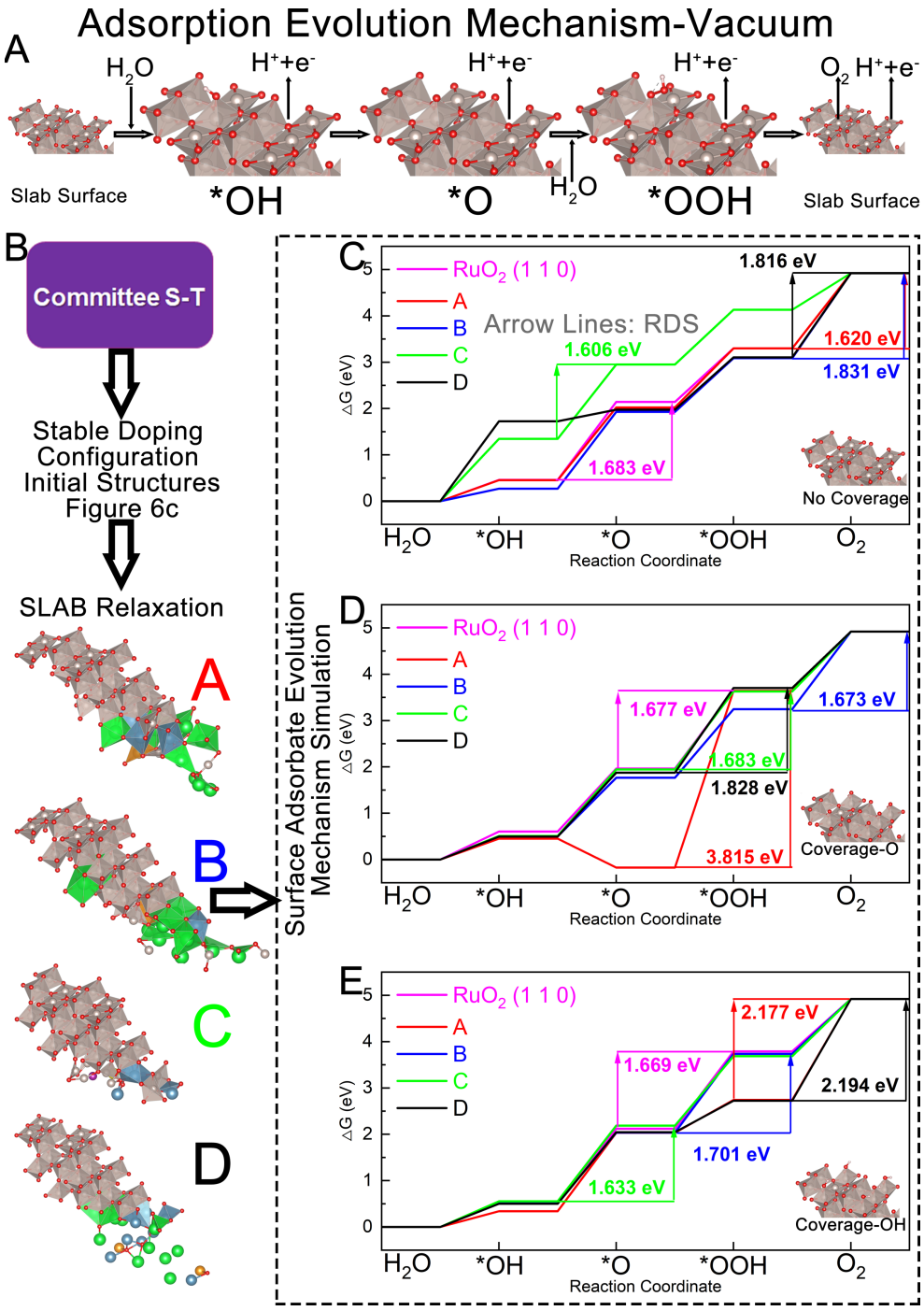

Fig. S36 OER reaction pathways and relaxed structures of samples A–D under the adsorption evolution mechanism (AEM). (A) Schematic illustration of the standard OER reaction pathway based on the AEM in vacuum. (B) Relaxed crystal structures of sample A~D corresponding to the doping structures obtained by GA search presented in **Fig. 6C**. (C) The comparison of OER and reaction pathways on the surface corresponding to the configurations of structures with a clean surface, namely, no additional species covered. Similarly, (D) and (E) are the corresponding results when the O and OH species have covered the nearing unsaturated coordinated Ru sites, respectively, as shown in the schematics. **Arrowed** lines are used to highlight the rate determining step (RDS) in the reactions.

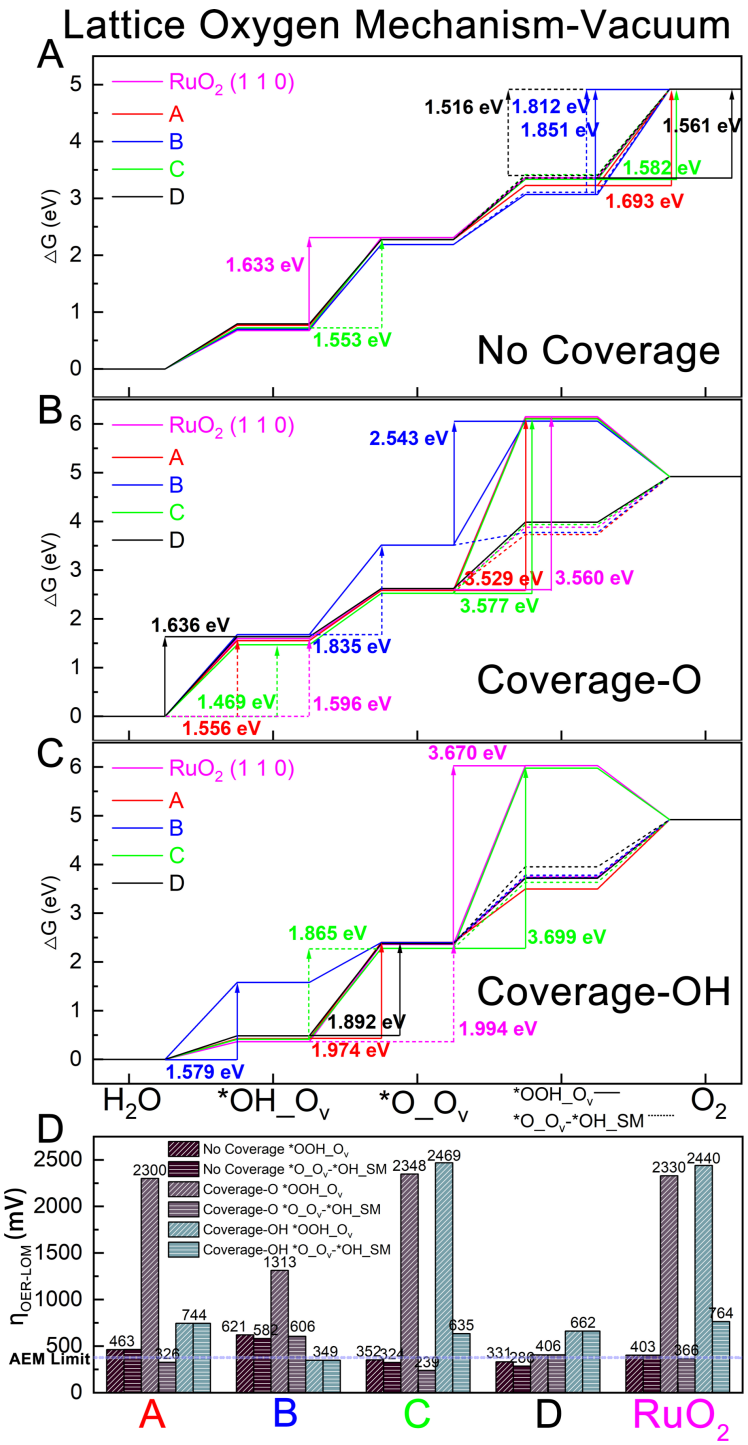

Fig. S37 Comparison of lattice oxygen mechanism (LOM) pathways under different surface coverage conditions in vacuum. (A)-(C) Comparison of reaction pathway under lattice oxygen mechanism with different surface coverage scenarios under default vacuum. The solid lines represent the oxygen vacancy site mechanism, and the dashed lines represent the adjacent single metal involved mechanism. The differences between the two LOM pathways lies in the configuration of the *OOH adsorbate (*86*). Noted as *OOH_O_v for the former, and *O_O_v-*OH_SM for the latter. (D) Summary of the theoretical overpotential under LOM with different surface coverage conditions.

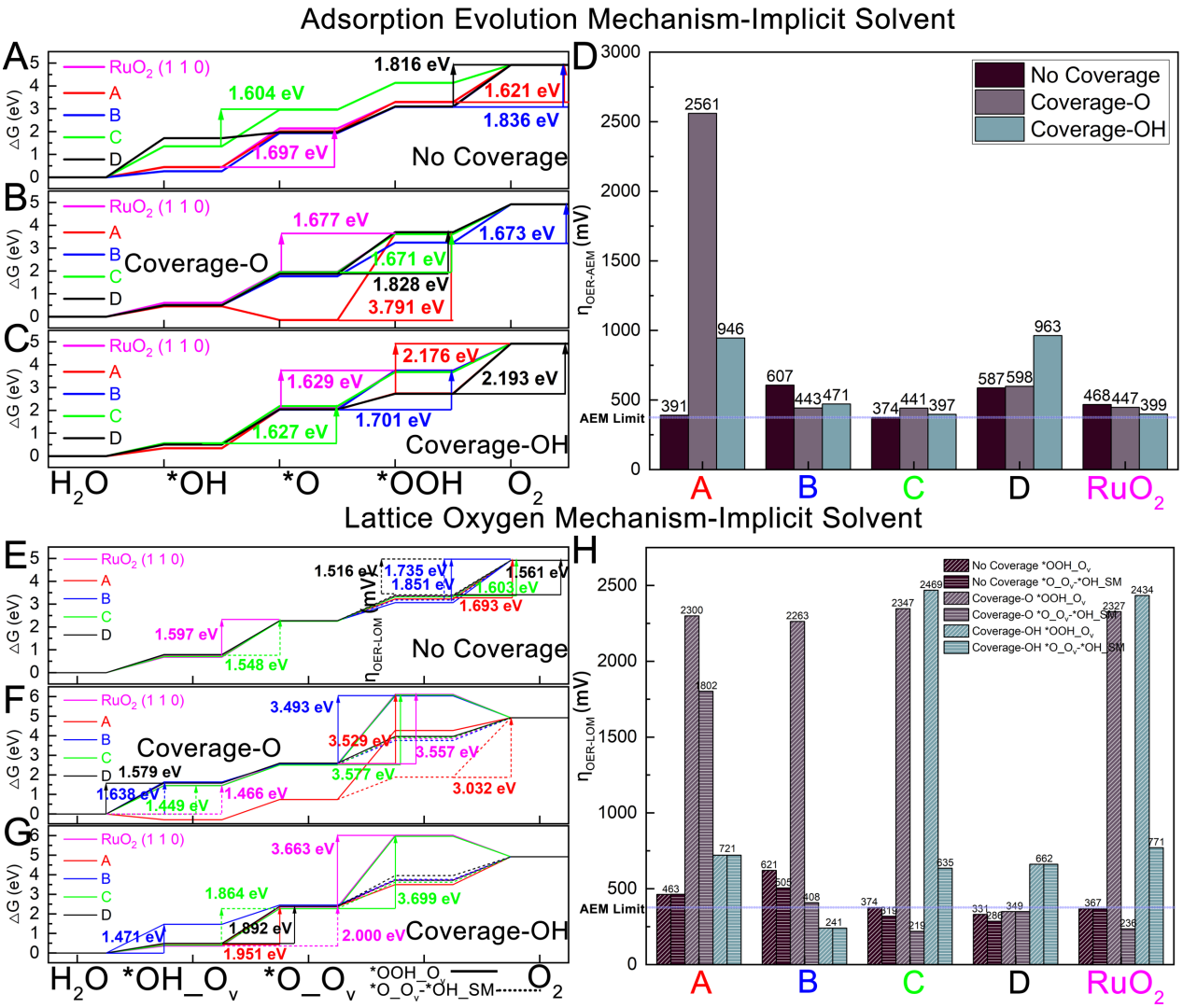

Fig. S38 Reaction pathways and overpotentials under AEM and LOM with implicit solvent field of water. (A)-(C) Comparison of reaction pathway and (d) summary of theoretical overpotentials under adsorption evolution mechanism with different surface coverage scenarios and implicit solvent field of water. (E)-(H) are corresponding results through lattice oxygen mechanism with implicit solvent field of water.

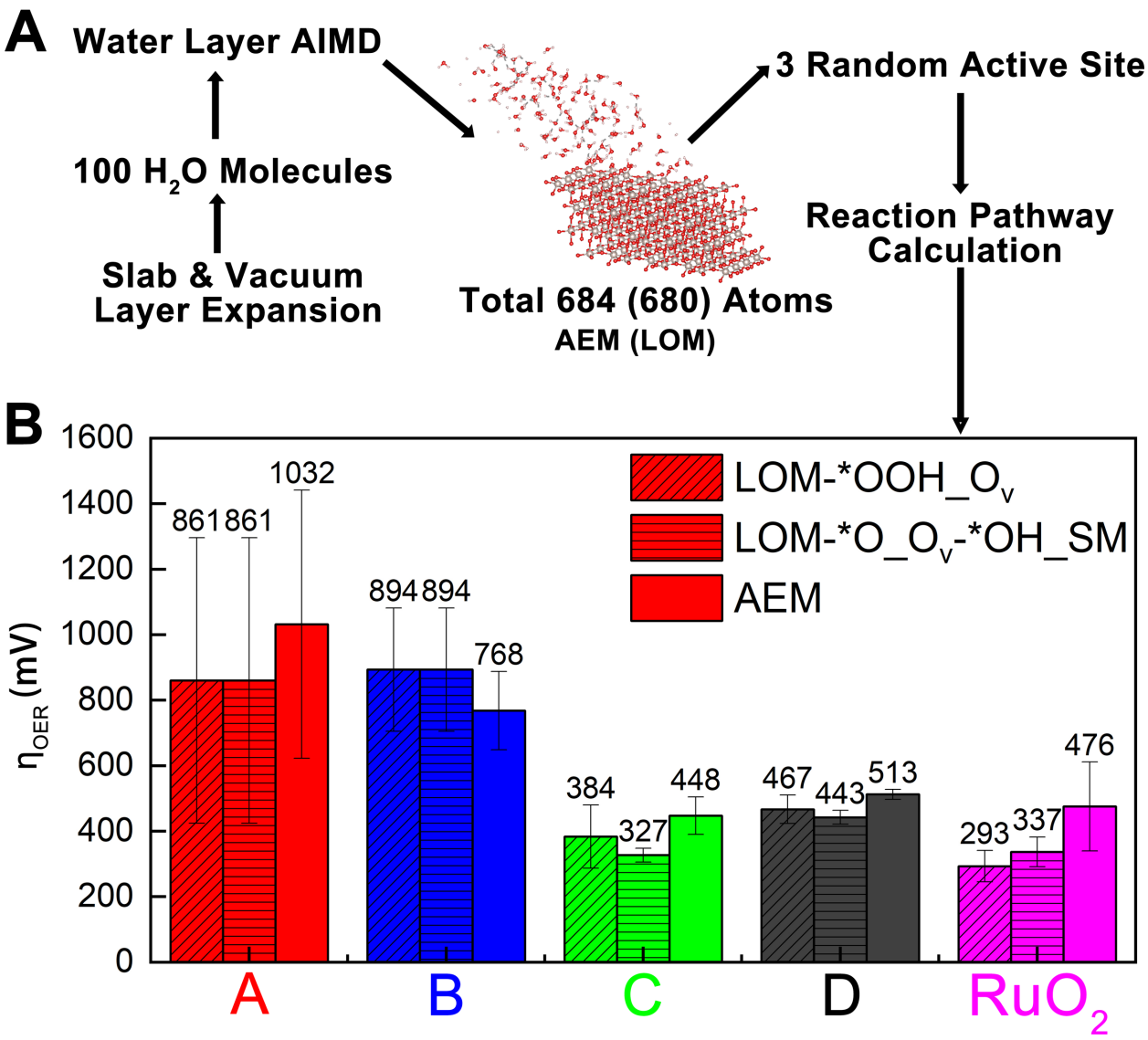

Fig. S39 Ab initio molecular dynamics workflow and explicit solvent field simulation results for OER overpotentials. (A) Schematic of the workflow of ab initio molecular dynamics process. (B) the histogram with error bars showing averaged OER overpotential values in this explicit solvent field simulation condition.

Note:

Based on **fig. S37** and **fig. S38**, we infer that all samples may achieve overpotentials below the conventional AEM threshold of 370 mV under certain surface coverage conditions. The observed patterns are complex yet suggestive of the lower overpotentials measured in experiments. Notably, sample C appears to have the potential to initiate the LOM pathway in two of the surface coverage scenarios (though OH-coverage scenario is hard for C), whereas the other samples show this potential in only one. Nevertheless, it is essential to acknowledge the discrepancies between experimental measurements and DFT simulations in the current studies. Although trends are generally consistent qualitatively, recent studies that include both experimental and DFT analyses (*86-91*) report a recurring phenomenon: experimentally measured overpotential values are often lower than theoretically obtained ones, even when simulating the LOM pathway. This discrepancy can be attributed in part to the simplified models

commonly employed in DFT (*84*), which may overlook critical surface features such as dynamic reconstructions and defect sites that can influence activity. Furthermore, DFT simulations often use approximate scaling relationships between adsorbate binding energies; these relationships may not be entirely accurate for transition-metal oxides, particularly under different applied potentials or electrochemical environments (*85*). Lastly, the lack of accurate environmental modeling in DFT, including solvent interactions, temperature effects, and pH variations, can lead to deviations from actual experimental values (*51*). These environmental effects can play a crucial role in real systems, lowering overpotentials by stabilizing certain intermediates and influencing reaction kinetics in ways that are challenging to capture in conventional DFT simulations. We can gain a glimpse of it through our results that surface coverage would largely vary and change the reaction pathways. However, C has shown comprehensively the best activity in most circumstances.

As we further conduct these AEM and LOM simulations in implicit solvent field, **fig. S38** provides the results that are highly consistent in trends with only minor changes in overpotential values, which further supports our claim. We also did a simplified explicit solvent simulation as a more realistic representation of the real OER process. We started with further expanding the samples' slabs in 2 by 2, ending up with 384 (380 for LOM) atoms large slab. We then created randomly a water layer through 100 water molecules on the surface. 2 ps of AIMD under 300K is performed for the relaxation of the water molecules into proper position and configurations. Then the system is fixed as to represent a more realistic OER reaction surface. Similar to previous simulations, we then randomly picked 3 active sites for doing the same AEM and LOM reaction pathway simulations to obtain the theoretical overpotential values. The corresponding simulation results in **fig. S39** indicated that though there are unignorable differences in local microenvironments, C and RuO_2 seem to still hold in average lowest overpotentials through different pathways. All the comprehensive simulations have strongly supported our experimental observation trend of intrinsic OER activity. While further advancements in computational methods, environmental models, and multi-scale approaches may help bridge the gap between experimental and theoretical overpotential values, the current level of consistency is sufficient to validate and guide experimental observations. We want to emphasize again that the calculation is based on an ideal model, ignoring some details, but it can discover trends and offer a guiding role. The introduction of different elements to regulate the electronic state of the active site and the synergistic effect is not an easy target for regular theoretical calculations, especially for our complex system with up to 4 metal elements.

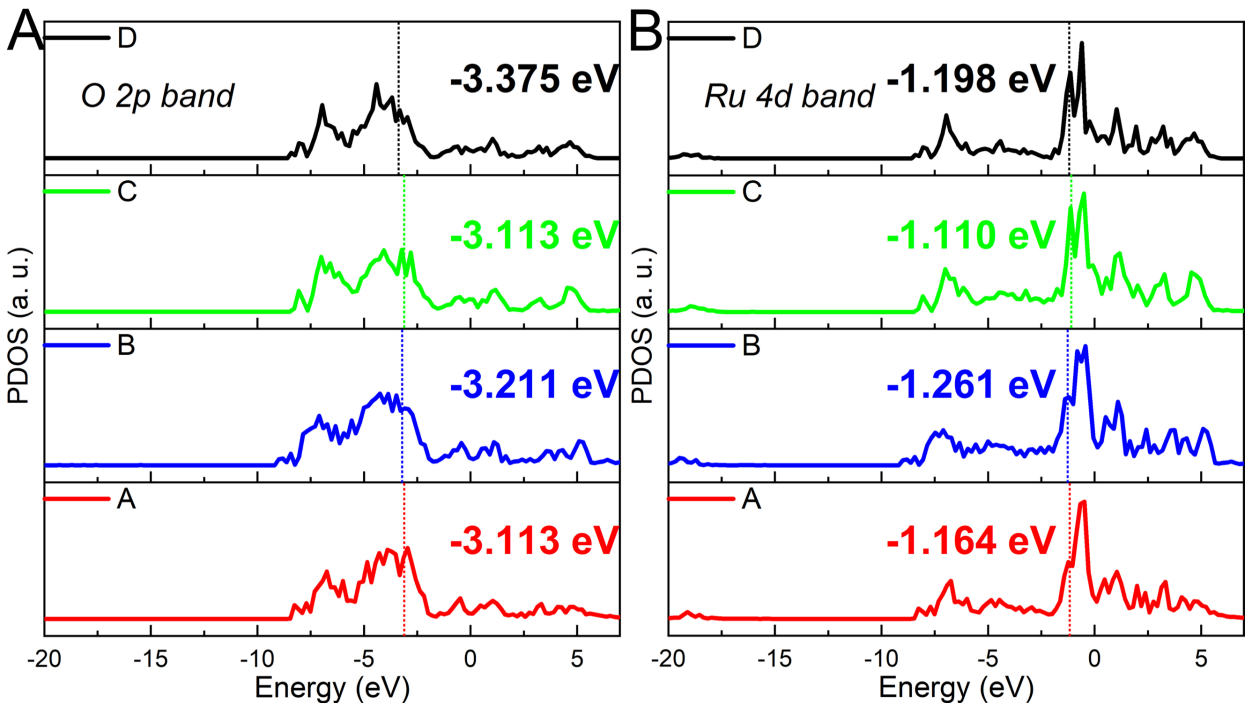

Fig. S40 Density of states (DOS) analysis of O 2p and Ru 4d bands in different samples. (A) Density of states plots of the O 2p band of different samples, (B) Density of states plots of the Ru 4d band of different samples.

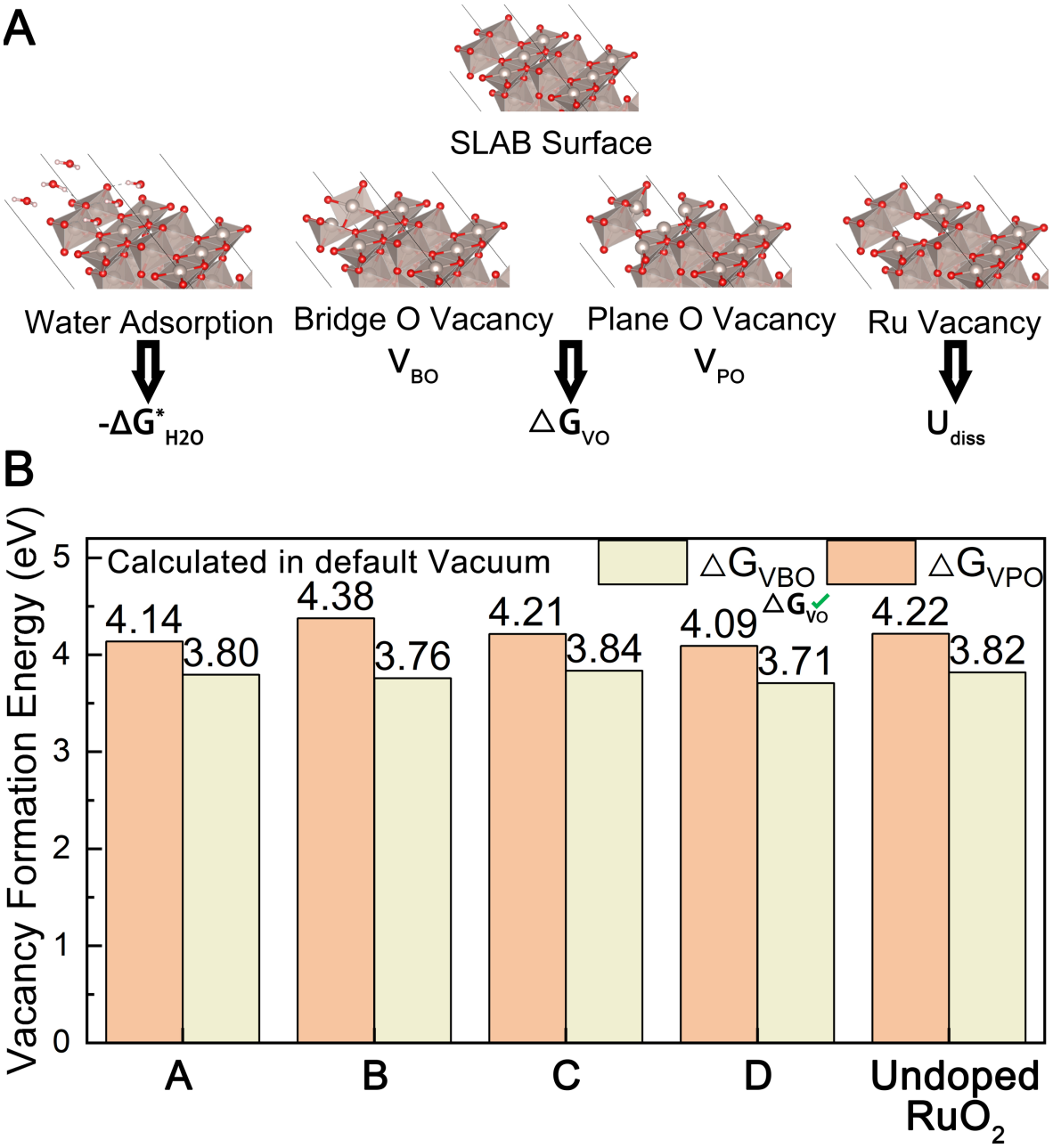

Fig. S41 O vacancy formation energies for different samples under vacuum. (A) Schematic of how different descriptors for theoretical stability was computed by surface manipulation, such as removing O and Ru atoms or the adsorption of water molecules. (B) Summary bar plots of the vacancy formation energy of different samples. The calculation is done in common default vacuum.

Note: As we can observe from (b), forming the plane O vacancy will always require more energy compared to forming the bridge O vacancy. Hence, we could determine that the O vacancy formation energy in our case is on bridge O, namely, V_O=V_{BO}. This is also consistent with the previous study presented by Hao et al. (*100*)

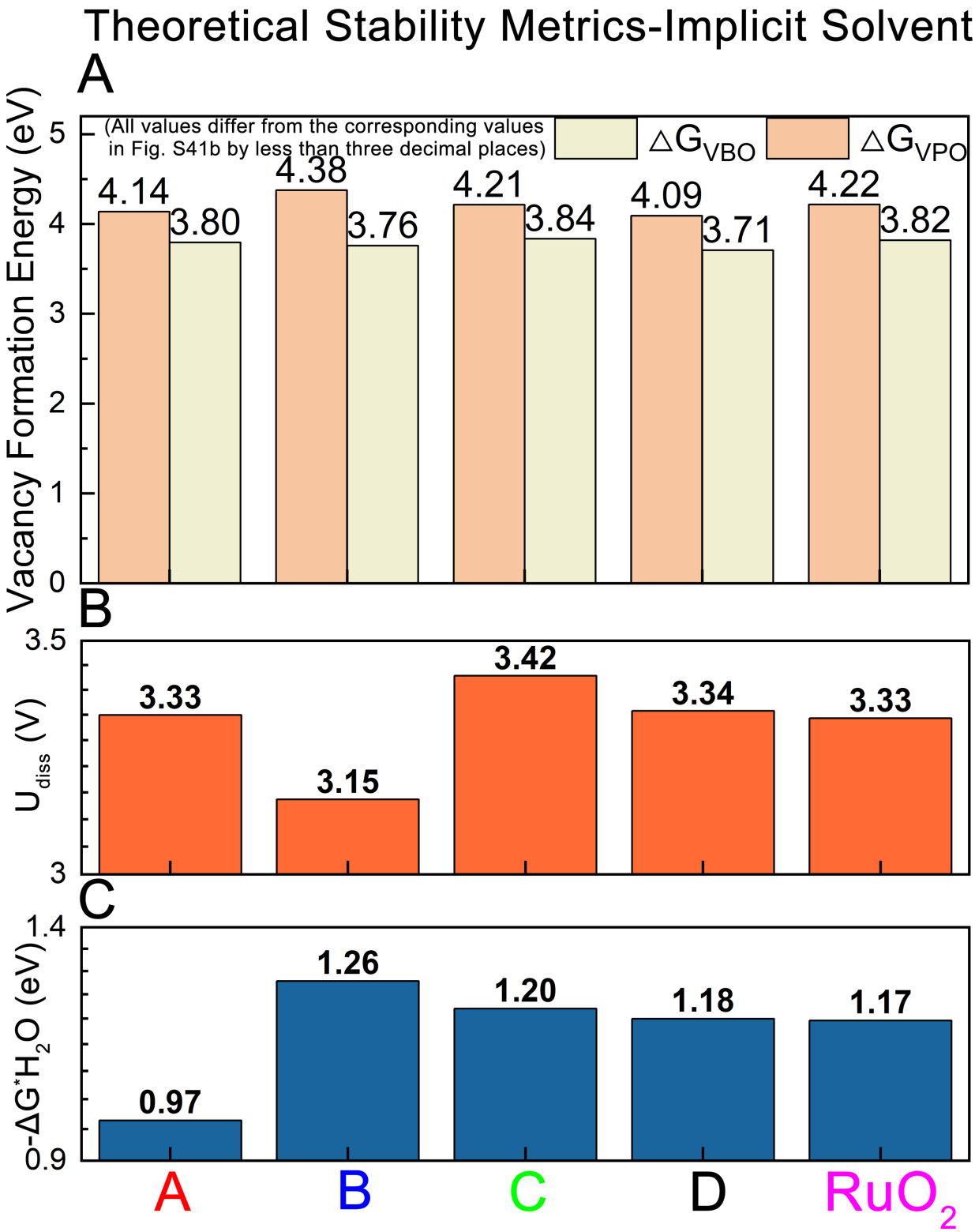

Fig. S42 Theoretical stability metrics calculated under an implicit solvent field. Theoretical stability metrics calculated in implicit solvent field corresponding to those calculated in default vacuum by **fig. S41B** and **Fig. 6E**: (A) $\triangle G_{VO}$ (the value differences are less than 0.001 hence the plot seems exactly the same) (B) U_{diss}. (C) $-\triangle G^{*}_{H2O}$

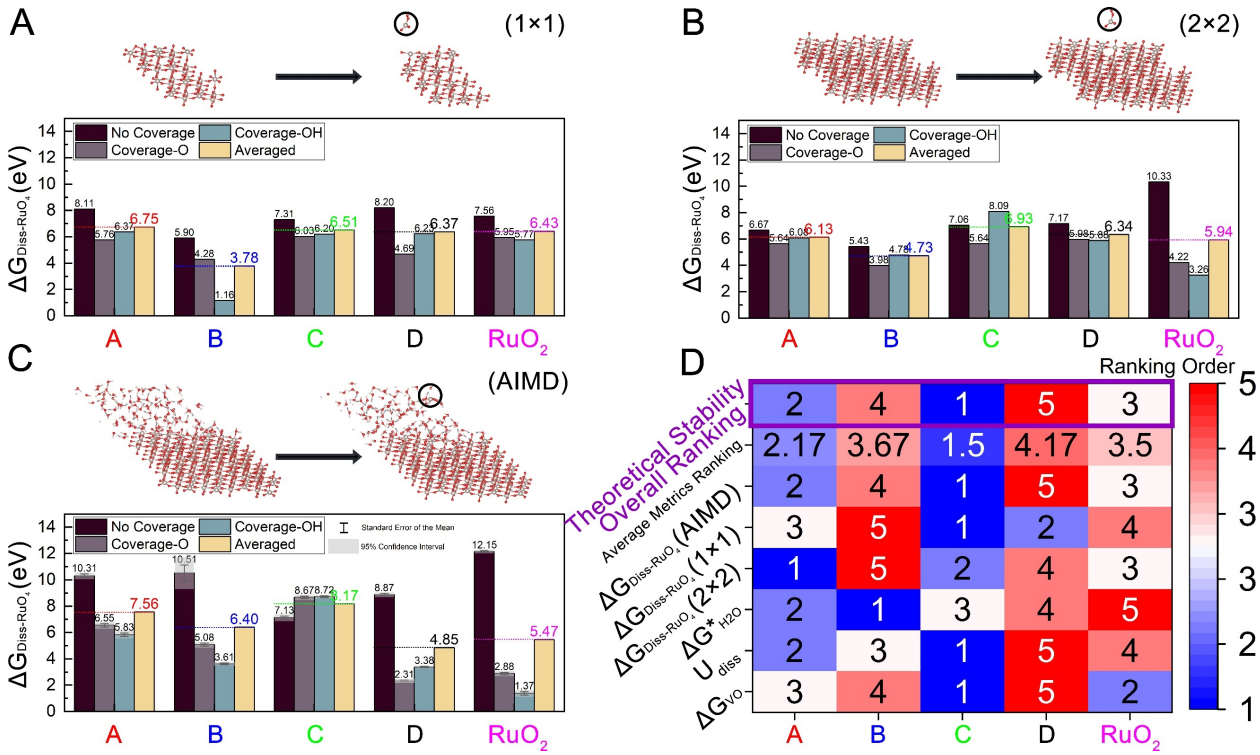

Fig. S43 Summary of free-energy barriers for the leaching of RuO_4 species ($\triangle G_{Diss\text{-}RuO4}$) simulated under various surface coverage scenarios and environments. (A) Free-energy barriers $\triangle G_{Diss\text{-}RuO4}$ in standard 1×1 slabs across different surface coverage scenarios in a vacuum. (B) Free-energy barriers $\triangle G_{Diss\text{-}RuO4}$ in expanded 2×2 slabs, identical to those used in fig. S39 for AEM/LOM pathway simulations (under AIMD optimized water solvent layer), under various surface coverage scenarios in a vacuum. (C) Statistical distribution (standard error and 95% confidence interval) and mean $\triangle G_{Diss\text{-}RuO4}$ values derived from AIMD simulations using the same expanded 2×2 slabs as in (B). The AIMD settings, including explicit water molecule counts and runtime, mirror those employed in the AEM/LOM pathway investigation as presented in fig. S39. The free-energy differences were computed using the final 200-fs timeframe sequence after equilibrium (<=0.0005 eV deviance per atom) was reached, with statistical metrics accompanying the mean values. (D) Heatmap summarizing the ranking of samples across various stability metrics ($\triangle G_{VO}$, U_{diss}, $-\triangle G^*_{H2O}$, and three $\triangle G_{Diss\text{-}RuO4}$) and their averaged rankings. The final overall ranking based on averaged ranking order is highlighted in the purple frame.

Note:
In panels (A)-(C), the black circles emphasize that we simulated the leaching of RuO_4 species originally located near an O vacancy that triggers the LOM pathway, as previously reported *(91, 103)*. Across samples, the energy barriers for RuO_4 leaching were observed to vary with surface coverage. Specifically, $\triangle G_{Diss\text{-}RuO4}$ values were generally lower under O and OH coverage than on clean, uncoated surfaces, a trend that was further accentuated in AIMD simulations with explicit solvation environments. Notably, AIMD results showed that for samples like D and undoped RuO_2, the energy barriers for RuO_4 leaching under O and OH coverage decreased significantly, while the barriers under clean surface conditions increased. Conversely, sample C exhibited a unique behavior: its $\triangle G_{Diss\text{-}RuO4}$ values were higher under O and OH coverage than

under clean surface conditions in AIMD simulations. Moreover, sample C demonstrated the lowest variability across coverage scenarios and ranked highest when averaging all coverage scenarios in defending against Ru leaching when evaluated under AIMD conditions.

Panel (D) presents a comprehensive summary of sample rankings across stability metrics we could collect. The general consistent trends among $\triangle G_{VO,}$ $U_{diss,}$ $-\triangle G^{*}_{H2O,}$ and three $\triangle G_{Diss\text{-}RuO4}$ metrics underscore the robustness of our findings. The averaged rankings place the samples in the following order: C > A > undoped RuO_2 > B > D, which aligns perfectly with the AIMD results for RuO_4 leaching simulations. These findings highlight the high fidelity of AIMD in capturing nuanced stability behaviors.

Furthermore, the close alignment of the $\triangle G_{VO}$ and U_{diss} rankings with the AIMD and overall ranking order—differing by only one position—underscores their reliability as cost-effective and approximate stability indicators compared to the more comprehensive AIMD results. This might also explain why they are widely adopted in the field *(73, 98–102)*.

In conclusion, while further mechanistic studies could expand upon these insights, our extended and comprehensive simulations robustly corroborate the experimental observations. Sample C unequivocally emerges as the optimal candidate for long-term stability, considering all evaluated perspectives.

REFERENCES AND NOTES

1. Y. Wang, Y. H. Pang, H. Xu, A. Martinez, K. S. Chen, PEM Fuel cell and electrolysis cell technologies and hydrogen infrastructure development - A review. *Energy Environ. Sci.* **15**, 2288–2328 (2022).

2. Z. C. Chen, L. Guo, L. Pan, T. Q. Yan, Z. X. He, Y. Li, C. X. Shi, Z. F. Huang, X. W. Zhang, J. J. Zou, Advances in oxygen evolution electrocatalysts for proton exchange membrane water electrolyzers. *Adv. Energy Mater.* **12**, 2103670 (2022).

3. T. Reier, H. N. Nong, D. Teschner, R. Schlögl, P. Strasser, Electrocatalytic oxygen evolution reaction in acidic environments–reaction mechanisms and catalysts. *Adv. Energy Mater.* **7**, 1601275 (2017).

4. L. An, C. Wei, M. Lu, H. W. Liu, Y. B. Chen, G. G. Scherer, A. C. Fisher, P. X. Xi, Z. C. J. Xu, C. H. Yan, Recent development of oxygen evolution electrocatalysts in acidic environment. *Adv. Mater.* **33**, e2006328 (2021).

5. Y. Y. Feng, S. Si, G. Deng, Z. X. Xu, Z. Pu, H. S. Hu, C. B. Wang, Copper-doped ruthenium oxide as highly efficient electrocatalysts for the evolution of oxygen in acidic media. *J. Alloys Compd.* **892**, 162113 (2022).

6. G. H. Moon, Y. Wang, S. Kim, E. Budiyanto, H. Tuysuz, Preparation of practical high-performance electrodes for acidic and alkaline media water electrolysis. *ChemSusChem* **15**, e202102114 (2022).

7. J. He, W. Q. Li, P. Xu, J. M. Sun, Tuning electron correlations of RuO_2 by co-doping of Mo and Ce for boosting electrocatalytic water oxidation in acidic media. *Appl. Catal. B Environ.* **298**, 120528 (2021).

8. T. Kwon, A. Yu, S. J. Kim, M. H. Kim, C. Lee, Y. Lee, Au-Ru alloy nanofibers as a highly stable and active bifunctional electrocatalyst for acidic water splitting. *Appl. Surf. Sci.* **563**, 150293 (2021).

9. W. Jin, H. B. Wu, W. Q. Cai, B. H. Jia, M. Batmunkh, Z. X. Wu, T. Y. Ma, Evolution of interfacial coupling interaction of Ni-Ru species for pH-universal water splitting. *Chem. Eng. J.* **426**, 130762 (2021).

10. Y. B. Wang, S. Hou, R. P. Ma, J. D. Jiang, Z. P. Shi, C. P. Liu, J. J. Ge, W. Xing, Modulating crystallinity and surface electronic structure of IrO_2 via gadolinium doping to promote acidic oxygen evolution. *ACS Sustain. Chem. Eng.* **9**, 10710–10716 (2021).

11. L. G. Li, P. T. Wang, Z. F. Cheng, Q. Shao, X. Q. Huang, One-dimensional iridium-based nanowires for efficient water electrooxidation and beyond. *Nano Res.* **15**, 1087–1093 (2022).

12. I. G. Kim, A. Lim, J. H. Jang, K. Y. Lee, I. W. Nah, S. Park, Leveraging metal alloy-hybrid support interaction to enhance oxygen evolution kinetics and stability in proton exchange membrane water electrolyzers. *J. Power Sources* **501**, 230002 (2021).

13. H. Hu, F. M. D. Kazim, Z. H. Ye, Y. H. Xie, Q. Zhang, K. G. Qu, J. X. Xu, W. W. Cai, S. L. Xiao, Z. H. Yang, Electronically delocalized Ir enables efficient and stable acidic water splitting. *J. Mater. Chem. A* **8**, 20168–20174 (2020).

14. Y. F. Sun, S. Dai, High-entropy materials for catalysis: A new frontier. *Sci. Adv.* **7**, eabg1600 (2021).

15. T. Loffler, A. Ludwig, J. Rossmeisl, W. Schuhmann, What makes high-entropy alloys exceptional electrocatalysts? *Angew. Chem. Int. Ed. Engl.* **60**, 26894–26903 (2021).

16. A. Amiri, R. Shahbazian-Yassar, Recent progress of high-entropy materials for energy storage and conversion. *J. Mater. Chem. A* **9**, 782–823 (2021).

17. C. Hu, K. Yue, J. Han, X. Liu, L. Liu, Q. Liu, Q. Kong, C. W. Pao, Z. Hu, K. Suenaga, D. Su, Q. Zhang, X. Wang, Y. Tan, X. Huang, Misoriented high-entropy iridium ruthenium oxide for acidic water splitting. *Sci. Adv.* **9**, eadf9144 (2023).

18. K. Miao, W. Jiang, Z. Chen, Y. Luo, D. Xiang, C. Wang, X. Kang, Hollow-structured and polyhedron-shaped high entropy oxide toward highly active and robust oxygen evolution reaction in a full pH range. *Adv. Mater.* **36**, e2308490 (2024).

19. H. Zhu, Z. Zhu, J. Hao, S. Sun, S. Lu, C. Wang, P. Ma, W. Dong, M. Du, High-entropy alloy stabilized active Ir for highly efficient acidic oxygen evolution. *Chem. Eng. J.* **431**, 133251 (2022).

20. R. Ding, Y. Chen, Z. Rui, K. Hua, Y. Wu, X. Li, X. Duan, J. Li, X. Wang, J. Liu, Machine learning utilized for the development of proton exchange membrane electrolyzers. *J. Power Sources* **556**, 232389 (2023).

21. M. Kim, Y. Kim, M. Y. Ha, E. Shin, S. J. Kwak, M. Park, I. D. Kim, W. B. Jung, W. B. Lee, Y. Kim, H. T. Jung, Exploring optimal water splitting bifunctional alloy catalyst by pareto active learning. *Adv. Mater.* **35**, e2211497 (2023).

22. B. Weng, Z. Song, R. Zhu, Q. Yan, Q. Sun, C. G. Grice, Y. Yan, W. J. Yin, Simple descriptor derived from symbolic regression accelerating the discovery of new perovskite catalysts. *Nat. Commun.* **11**, 3513 (2020).

23. W. T. Hong, R. E. Welsch, Y. Shao-Horn, Descriptors of oxygen-evolution activity for oxides: A statistical evaluation. *J. Phys. Chem. C* **120**, 78–86 (2015).

24. Y. M. Sun, H. B. Liao, J. R. Wang, B. Chen, S. N. Sun, S. J. H. Ong, S. B. Xi, C. Z. Diao, Y. H. Du, J. O. Wang, M. B. H. Breese, S. Z. Li, H. Zhang, Z. C. J. Xu, Covalency competition dominates the water oxidation structure-activity relationship on spinel oxides. *Nat. Catal.* **3**, 554–563 (2020).

25. S. Back, K. Tran, Z. W. Ulissi, Toward a design of active oxygen evolution catalysts: Insights from automated density functional theory calculations and machine learning. *ACS Catal.* **9**, 7651–7659 (2019).

26. N. J. van Eck, L. Waltman, Software survey: VOSviewer, a computer program for bibliometric mapping. *Scientometrics* **84**, 523–538 (2010).

27. R. Ding, X. Wang, A. Tan, J. Li, J. Liu, Unlocking new insights for electrocatalyst design: A unique data science workflow leveraging internet-sourced big data. *ACS Catal.* **13**, 13267–13281 (2023).

28. N. A. Tapan, M. E. Günay, R. Yildirim, Constructing global models from past publications to improve design and operating conditions for direct alcohol fuel cells. *Chem. Eng. Res. Des.* **105**, 162–170 (2016).

29. E. Can, R. Yildirim, Data mining in photocatalytic water splitting over perovskites literature for higher hydrogen production. *Appl. Catal. B Environ.* **242**, 267–283 (2019).

30. I. C. Man, H. Y. Su, F. Calle-Vallejo, H. A. Hansen, J. I. Martinez, N. G. Inoglu, J. Kitchin, T. F. Jaramillo, J. K. Norskov, J. Rossmeisl, Universality in oxygen evolution electrocatalysis on oxide surfaces. *ChemCatChem* **3**, 1159–1165 (2011).

31. T. Reier, M. Oezaslan, P. Strasser, Electrocatalytic oxygen evolution reaction (OER) on Ru, Ir, and Pt catalysts: A comparative study of nanoparticles and bulk materials. *ACS Catal.* **2**, 1765–1772 (2012).

32. M. E. C. Pascuzzi, J. P. Hofmann, E. J. M. Hensen, Promoting oxygen evolution of IrO2 in acid electrolyte by Mn. *Electrochim. Acta* **366**, 137448 (2021).

33. C. Zheng, B. Huang, X. Liu, H. Wang, L. Guan, Mn-doped RuO 2 nanocrystals with abundant oxygen vacancies for enhanced oxygen evolution in acidic media. *Inorg. Chem. Front.* **11**, 1912–1922 (2024).

34. M. Ji, X. Yang, S. Chang, W. Chen, J. Wang, D. He, Y. Hu, Q. Deng, Y. Sun, B. Li, J. Xi, T. Yamada, J. Zhang, H. Xiao, C. Zhu, J. Li, Y. Li, RuO 2 clusters derived from bulk SrRuO 3: Robust catalyst for oxygen evolution reaction in acid. *Nano Res.* **15**, 1959–1965 (2022).

35. L. C. Seitz, C. F. Dickens, K. Nishio, Y. Hikita, J. Montoya, A. Doyle, C. Kirk, A. Vojvodic, H. Y. Hwang, J. K. Norskov, T. F. Jaramillo, A highly active and stable IrO x/SrIrO3 catalyst for the oxygen evolution reaction. *Science* **353**, 1011–1014 (2016).

36. S. Wold, K. Esbensen, P. Geladi, Principal component analysis. *Chemom. Intell. Lab. Syst.* **2**, 37–52 (1987).

37. L. van der Maaten, G. Hinton, Visualizing data using t-SNE. *J. Mach. Learn. Res.* **9**, 2579–2605 (2008).

38. S. Kee, E. Del Castillo, G. Runger, Query-by-committee improvement with diversity and density in batch active learning. *Inf. Sci.* **454**, 401–418 (2018).

39. H. Aziz, B. de Keijzer, in *31st International Symposium on Theoretical Aspects of Computer Science (STACS)* (Schloss Dagstuhl – Leibniz-Zentrum für Informatik, 2014), pp. 99–111.

40. J. H. Friedman, B. E. Popescu, Predictive learning via rule ensembles. *Ann. Appl. Stat.* **2**, 916–954 (2008).

41. B. M. Greenwell, pdp: An R package for constructing partial dependence plots. *R J.* **9**, 421–436 (2017).

42. H. Sun, W. Jung, Recent advances in doped ruthenium oxides as high-efficiency electrocatalysts for the oxygen evolution reaction. *J. Mater. Chem. A* **9**, 15506–15521 (2021).

43. J. Bai, W. Zhou, J. Xu, P. Zhou, Y. Deng, M. Xiang, D. Xiang, Y. Su, RuO_2 catalysts for electrocatalytic oxygen evolution in acidic media: Mechanism, activity promotion strategy and research progress. *Molecules* **29**, 537 (2024).

44. J. Hao, Z. Zhuang, K. Cao, G. Gao, C. Wang, F. Lai, S. Lu, P. Ma, W. Dong, T. Liu, M. du, H. Zhu, Unraveling the electronegativity-dominated intermediate adsorption on high-entropy alloy electrocatalysts. *Nat. Commun.* **13**, 2662 (2022).

45. L. Zhao, S.-G. Park, B. Magyari-Köpe, Y. Nishi, Dopant selection rules for desired electronic structure and vacancy formation characteristics of TiO_2 resistive memory. *Appl. Phys. Lett.* **102**, 083506 (2013).

46. H.-W. Lv, H.-B. Zhao, X.-Y. Peng, Z.-G. Ye, Q.-B. Huang, X.-T. Yuan, D.-S. Li, Z. Jin, Rhenium-boosted electrocatalytic activity and durability of pyrolytic IrO_2 for acidic oxygen evolution. *Rare Metals* **43**, 6758–6764 (2024).

47. S. R. Ede, Z. Luo, Tuning the intrinsic catalytic activities of oxygen-evolution catalysts by doping: A comprehensive review. *J. Mater. Chem. A* **9**, 20131–20163 (2021).

48. G. H. Kim, Y. S. Park, J. Yang, M. J. Jang, J. Jeong, J.-H. Lee, H.-S. Park, Y. H. Park, S. M. Choi, J. Lee, Effects of annealing temperature on the oxygen evolution reaction activity of copper–cobalt oxide nanosheets. *Nanomaterials* **11**, 657 (2021).

49. L. G. M. Pettersson, A. Nilsson, A molecular perspective on the d-band model: Synergy between experiment and theory. *Top. Catal.* **57**, 2–13 (2014).

50. J. Hu, A. Al-Salihy, B. Zhang, S. Li, P. Xu, Mastering the D-band center of iron-series metal-based electrocatalysts for enhanced electrocatalytic water splitting. *Int. J. Mol. Sci.* **23**, 15405 (2022).

51. T. Naito, T. Shinagawa, T. Nishimoto, K. Takanabe, Recent advances in understanding oxygen evolution reaction mechanisms over iridium oxide. *Inorg. Chem. Front.* **8**, 2900–2917 (2021).

52. Z. Wu, L. Jiang, Q. Dong, Q. Gao, J. Cai, X. Cheng, Effect and mechanism of rare Earth and alkaline Earth metals on the high-temperature stability of activated alumina. *Front. Mat.* **10**, 1103590 (2023).

53. Y. Liu, H. Huang, L. Xue, J. Sun, X. Wang, P. Xiong, J. Zhu, Recent advances in the heteroatom doping of perovskite oxides for efficient electrocatalytic reactions. *Nanoscale* **13**, 19840–19856 (2021).

54. H. Sun, X. Xu, G. Chen, Z. Shao, Perovskite oxides as electrocatalysts for water electrolysis: From crystalline to amorphous. *Carbon Energy* **6**, e595 (2024).

55. J. Sengupta, R. K. Sahoo, C. D. Mukherjee, Effect of annealing on the structural, topographical and optical properties of sol–gel derived ZnO and AZO thin films. *Mater. Lett.* **83**, 84–87 (2012).

56. D. Yadav, R. Gahlawat, R. Shukla, A comprehensive analysis of the impact of annealing temperature variation on the structural, optical, morphological, magnetic, and photocatalytic properties of $CoFe_2O_4$ nanoparticles. *Ionics* **30**, 6559–6574 (2024).

57. S. B. Attanayake, A. Chanda, T. Hulse, R. Das, M.-H. Phan, H. Srikanth, Competing magnetic interactions and field-induced metamagnetic transition in highly crystalline phase-tunable iron oxide nanorods. *Nanomaterials* **13**, 1340 (2023).

58. Y. Wang, H. Pan, Z. Liu, P. Kang, $RuO_2/CoMo_2O_x$ catalyst with low ruthenium loading for long-term acidic oxygen evolution. *Trans. Tianjin Univ.* **30**, 395–405 (2024).

59. X. Zhang, Y. Liu, X. Ma, X. Liu, R. Zhang, Y. Wang, Metal–support interaction of carbon–based electrocatalysts for oxygen evolution reaction. *Nanoenergy Adv.* **3**, 48–72 (2023).

60. D. Coertzen, R. J. Kriek, P. B. J. Levecque, A. Falch, Vulcan carbon as support for sputtered oxygen evolution electrocatalysts. *Electrocatalysis* **10**, 604–612 (2019).

61. L. Lahn, A. M. Mingers, A. Savan, A. Ludwig, O. Kasian, Low Ti Additions to stabilize Ru-Ir electrocatalysts for the oxygen evolution reaction. *ChemElectroChem* **11**, e202300399 (2024).

62. X. Teng, J. Gao, Z. Yang, X. Liang, X. Wu, J. Yun, J. Zhang, $RuO_2@IrO_2/C$ core-shell structure catalyst for efficient and durable acidic oxygen evolution. *Catalysts* **13**, 1456 (2023).

63. Z. J. Xu, T. D. Nguyen, G. G. Scherer, A facile synthesis of size-controllable IrO2 and RuO2 nanoparticles for the oxygen evolution reaction. *Electrocatalysis* **7**, 420–427 (2016).

64. G. C. da Silva, N. Perini, E. A. Ticianelli, Effect of temperature on the activities and stabilities of hydrothermally prepared IrO_x nanocatalyst layers for the oxygen evolution reaction. *Appl. Catal. B Environ.* **218**, 287–297 (2017).

65. I. Rodríguez-García, D. Galyamin, L. Pascual, P. Ferrer, M. A. Peña, D. Grinter, G. Held, M. Abdel Salam, M. Mokhtar, K. Narasimharao, M. Retuerto, S. Rojas, Enhanced stability of SrRuO3 mixed oxide via monovalent doping in $Sr_{1-x}K_xRuO_3$ for the oxygen evolution reaction. *J. Power Sources* **521**, 230950 (2022).

66. B.-J. Kim, D. F. Abbott, X. Cheng, E. Fabbri, M. Nachtegaal, F. Bozza, I. E. Castelli, D. Lebedev, R. Schäublin, C. Copéret, T. Graule, N. Marzari, T. J. Schmidt, Unraveling

thermodynamics, stability, and oxygen evolution activity of strontium ruthenium perovskite oxide. *ACS Catal.* **7**, 3245–3256 (2017).

67. M. Retuerto, L. Pascual, F. Calle-Vallejo, P. Ferrer, D. Gianolio, A. G. Pereira, A. Garcia, J. Torrero, M. T. Fernandez-Diaz, P. Bencok, M. A. Pena, J. L. G. Fierro, S. Rojas, Na-doped ruthenium perovskite electrocatalysts with improved oxygen evolution activity and durability in acidic media. *Nat. Commun.* **10**, 2041 (2019).

68. M. Ji, X. Yang, S. Chang, W. Chen, J. Wang, D. He, Y. Hu, Q. Deng, Y. Sun, B. Li, J. Xi, T. Yamada, J. Zhang, H. Xiao, C. Zhu, J. Li, Y. Li, RuO_2 clusters derived from bulk $SrRuO_3$: Robust catalyst for oxygen evolution reaction in acid. *Nano Res.* **15**, 1959–1965 (2022).

69. S. Chen, H. Huang, P. Jiang, K. Yang, J. Diao, S. Gong, S. Liu, M. Huang, H. Wang, Q. Chen, Mn-Doped RuO_2 nanocrystals as highly active electrocatalysts for enhanced oxygen evolution in acidic media. *ACS Catal.* **10**, 1152–1160 (2020).

70. K. Wang, Y. Wang, B. Yang, Z. Li, X. Qin, Q. Zhang, L. Lei, M. Qiu, G. Wu, Y. Hou, Highly active ruthenium sites stabilized by modulating electron-feeding for sustainable acidic oxygen-evolution electrocatalysis. *Energy Environ. Sci.* **15**, 2356–2365 (2022).

71. W. Li, R. Liu, G. Yu, X. Chen, S. Yan, S. Ren, J. Chen, W. Chen, C. Wang, X. Lu, Rationally construction of Mn-doped RuO_2 nanofibers for high-activity and stable alkaline ampere-level current density overall water splitting. *Small* **20**, e2307164 (2024).

72. W. Xu, H. Huang, X. Wu, Y. Yuan, Y. Liu, Z. Wang, D. Zhang, Y. Qin, J. Lai, L. Wang, Mn-doped Ru/RuO_2 nanoclusters@CNT with strong metal-support interaction for efficient water splitting in acidic media. *Compos. Part B Eng.* **242**, 110013 (2022).

73. M. Umer, S. Umer, M. Zafari, M. Ha, R. Anand, A. Hajibabaei, A. Abbas, G. Lee, K. S. Kim, Machine learning assisted high-throughput screening of transition metal single atom based superb hydrogen evolution electrocatalysts. *J. Mater. Chem. A* **10**, 6679–6689 (2022).

74. G. R. Schleder, A. C. M. Padilha, C. M. Acosta, M. Costa, A. Fazzio, From DFT to machine learning: Recent approaches to materials science–A review. *J. Phys. Mater.* **2**, 032001 (2019).

75. S. Gao, H. Zhen, B. Wen, J. Ma, X. Zhang, Exploring the physical origin of the electrocatalytic performance of an amorphous alloy catalyst via machine learning accelerated DFT study. *Nanoscale* **14**, 2660–2667 (2022).

76. Z. Li, D. Hoiem, Learning without forgetting. *IEEE Trans. Pattern Anal. Mach. Intell.* **40**, 2935–2947 (2018).

77. G. T. K. K. Gunasooriya, J. K. Nørskov, Analysis of acid-stable and active oxides for the oxygen evolution reaction. *ACS Energy Lett.* **5**, 3778–3787 (2020).

78. A. Grimaud, O. Diaz-Morales, B. Han, W. T. Hong, Y. L. Lee, L. Giordano, K. A. Stoerzinger, M. T. M. Koper, Y. Shao-Horn, Activating lattice oxygen redox reactions in metal oxides to catalyse oxygen evolution. *Nat. Chem.* **9**, 457–465 (2017).

79. S. Xin, Y. Tang, B. Jia, Z. Zhang, C. Li, R. Bao, C. Li, J. Yi, J. Wang, T. Ma, Coupling adsorbed evolution and lattice oxygen mechanism in Fe-Co$(OH)_2$/Fe_2O_3 heterostructure for enhanced electrochemical water oxidation. *Adv. Funct. Mater.* **33**, 2305243 (2023).

80. S. Zhu, L. Song, Z. Xu, F. Chen, H. Tao, X. Tang, Y. Wang, Theoretical and experimental aspects of electrocatalysts for oxygen evolution reaction. *Chemistry* **30**, e202303672 (2024).

81. X. Liu, Z. He, M. Ajmal, C. Shi, R. Gao, L. Pan, Z.-F. Huang, X. Zhang, J.-J. Zou, Recent advances in the comprehension and regulation of lattice oxygen oxidation mechanism in oxygen evolution reaction. *Trans. Tianjin Univ.* **29**, 247–253 (2023).

82. M. Chatenet, B. G. Pollet, D. R. Dekel, F. Dionigi, J. Deseure, P. Millet, R. D. Braatz, M. Z. Bazant, M. Eikerling, I. Staffell, P. Balcombe, Y. Shao-Horn, H. Schafer, Water electrolysis: From textbook knowledge to the latest scientific strategies and industrial developments. *Chem. Soc. Rev.* **51**, 4583–4762 (2022).

83. J. Song, C. Wei, Z. F. Huang, C. Liu, L. Zeng, X. Wang, Z. J. Xu, A review on fundamentals for designing oxygen evolution electrocatalysts. *Chem. Soc. Rev.* **49**, 2196–2214 (2020).

84. S. Divanis, A. M. Frandsen, T. Kutlusoy, J. Rossmeisl, Lifting the discrepancy between experimental results and the theoretical predictions for the catalytic activity of RuO_2(110) towards oxygen evolution reaction. *Phys. Chem. Chem. Phys.* **23**, 19141–19145 (2021).

85. S. Divanis, T. Kutlusoy, I. M. Ingmer Boye, I. C. Man, J. Rossmeisl, Oxygen evolution reaction: A perspective on a decade of atomic scale simulations. *Chem. Sci.* **11**, 2943–2950 (2020).

86. Y. Wang, R. Yang, Y. Ding, B. Zhang, H. Li, B. Bai, M. Li, Y. Cui, J. Xiao, Z. S. Wu, Unraveling oxygen vacancy site mechanism of Rh-doped RuO_2 catalyst for long-lasting acidic water oxidation. *Nat. Commun.* **14**, 1412 (2023).

87. S. Y. Hao, H. Y. Sheng, M. Liu, J. Z. Huang, G. K. Zheng, F. Zhang, X. N. Liu, Z. W. Su, J. J. Hu, Y. Qian, L. N. Zhou, Y. He, B. Song, L. C. Lei, X. W. Zhang, S. Jin, Torsion strained iridium oxide for efficient acidic water oxidation in proton exchange membrane electrolyzers. *Nat. Nanotechnol.* **16**, 1371–1377 (2021).

88. Z. P. Shi, Y. Wang, J. Li, X. Wang, Y. B. Wang, Y. Li, W. L. Xu, Z. Jiang, C. P. Liu, W. Xing, J. J. Ge, Confined Ir single sites with triggered lattice oxygen redox: Toward boosted and sustained water oxidation catalysis. *Aust. Dent. J.* **5**, 2164–2176 (2021).

89. A. M. Harzandi, S. Shadman, A. S. Nissimagoudar, D. Y. Kim, H. D. Lim, J. H. Lee, M. G. Kim, H. Y. Jeong, Y. Kim, K. S. Kim, Ruthenium core–shell engineering with nickel single atoms for selective oxygen evolution via nondestructive mechanism. *Adv. Energy Mater.* **11**, 2003448 (2021).

90. D. A. Kuznetsov, M. A. Naeem, P. V. Kumar, P. M. Abdala, A. Fedorov, C. R. Muller, Tailoring lattice oxygen binding in ruthenium pyrochlores to enhance oxygen evolution activity. *J. Am. Chem. Soc.* **142**, 7883–7888 (2020).

91. N. Yao, H. Jia, J. Zhu, Z. Shi, H. Cong, J. Ge, W. Luo, Atomically dispersed Ru oxide catalyst with lattice oxygen participation for efficient acidic water oxidation. *Chem* **9**, 1882–1896 (2023).

92. L. Giordano, K. Akkiraju, R. Jacobs, D. Vivona, D. Morgan, Y. Shao-Horn, Electronic structure-based descriptors for oxide properties and functions. *Acc. Chem. Res.* **55**, 298–308 (2022).

93. J. Kim, P. C. Shih, K. C. Tsao, Y. T. Pan, X. Yin, C. J. Sun, H. Yang, High-performance pyrochlore-type yttrium ruthenate electrocatalyst for oxygen evolution reaction in acidic media. *J. Am. Chem. Soc.* **139**, 12076–12083 (2017).

94. M. A. Hubert, A. M. Patel, A. Gallo, Y. Liu, E. Valle, M. Ben-Naim, J. Sanchez, D. Sokaras, R. Sinclair, J. K. Nørskov, L. A. King, M. Bajdich, T. F. Jaramillo, Acidic oxygen evolution reaction activity–stability relationships in Ru-based pyrochlores. *ACS Catal.* **10**, 12182–12196 (2020).

95. R. Ovcharenko, E. Voloshina, J. Sauer, Water adsorption and O-defect formation on Fe_2O_3 (0001) surfaces. *Phys. Chem. Chem. Phys.* **18**, 25560–25568 (2016).

96. S. Goverapet Srinivasan, R. Shivaramaiah, P. R. Kent, A. G. Stack, R. Riman, A. Anderko, A. Navrotsky, V. S. Bryantsev, A comparative study of surface energies and water adsorption on Ce-bastnasite, La-bastnasite, and calcite via density functional theory and water adsorption calorimetry. *Phys. Chem. Chem. Phys.* **19**, 7820–7832 (2017).

97. R. R. Rao, M. J. Kolb, J. Hwang, A. F. Pedersen, A. Mehta, H. You, K. A. Stoerzinger, Z. Feng, H. Zhou, H. Bluhm, L. Giordano, I. E. L. Stephens, Y. Shao-Horn, Surface orientation dependent water dissociation on rutile ruthenium dioxide. *J. Phys. Chem. C* **122**, 17802–17811 (2018).

98. M. Ha, D. Y. Kim, M. Umer, V. Gladkikh, C. W. Myung, K. S. Kim, Tuning metal single atoms embedded in NxCy moieties toward high-performance electrocatalysis. *Energy Environ. Sci.* **14**, 3455–3468 (2021).

99. J. Greeley, J. K. Nørskov, Electrochemical dissolution of surface alloys in acids: Thermodynamic trends from first-principles calculations. *Electrochim. Acta* **52**, 5829–5836 (2007).

100. S. Hao, M. Liu, J. Pan, X. Liu, X. Tan, N. Xu, Y. He, L. Lei, X. Zhang, Dopants fixation of Ruthenium for boosting acidic oxygen evolution stability and activity. *Nat. Commun.* **11**, 5368 (2020).

101. A. Li, S. Kong, C. Guo, H. Ooka, K. Adachi, D. Hashizume, Q. Jiang, H. Han, J. Xiao, R. Nakamura, Enhancing the stability of cobalt spinel oxide towards sustainable oxygen evolution in acid. *Nat. Catal.* **5**, 109–118 (2022).

102. H.-Y. Su, K. Sun, DFT study of the stability of oxygen vacancy in cubic ABO_3 perovskites. *J. Mater. Sci.* **50**, 1701–1709 (2014).

103. X. Ping, Y. Liu, L. Zheng, Y. Song, L. Guo, S. Chen, Z. Wei, Locking the lattice oxygen in RuO_2 to stabilize highly active Ru sites in acidic water oxidation. *Nat. Commun.* **15**, 2501 (2024).

104. R. Ding, R. Wang, Y. Q. Ding, W. J. Yin, Y. D. Liu, J. Li, J. G. Liu, Designing AI-aided analysis and prediction models for nonprecious metal electrocatalyst-based proton-exchange membrane fuel cells. *Angew. Chem. Int. Ed. Engl.* **59**, 19175–19183 (2020).

105. R. Rodríguez, M. Pastorini, L. Etcheverry, C. Chreties, M. Fossati, A. Castro, A. Gorgoglione, Water-quality data imputation with a high percentage of missing values: A machine learning approach. *Sustainability* **13**, 6318 (2021).

106. C. Li, X. Ren, G. Zhao, Machine-learning-based imputation method for filling missing values in ground meteorological observation data. *Algorithms* **16**, 422 (2023).

107. A. A. Dharmasaputro, N. M. Fauzan, M. Kallista, I. P. D. Wibawa, P. D. Kusuma, in *2021 International Seminar on Machine Learning, Optimization, and Data Science (ISMODE)* (IEEE, 2022), pp. 140–145.

108. A. Merchant, S. Batzner, S. S. Schoenholz, M. Aykol, G. Cheon, E. D. Cubuk, Scaling deep learning for materials discovery. *Nature* **624**, 80–85 (2023).

109. N. J. Szymanski, B. Rendy, Y. Fei, R. E. Kumar, T. He, D. Milsted, M. J. McDermott, M. Gallant, E. D. Cubuk, A. Merchant, H. Kim, A. Jain, C. J. Bartel, K. Persson, Y. Zeng, G.

Ceder, An autonomous laboratory for the accelerated synthesis of novel materials. *Nature* **624**, 86–91 (2023).

110. H. Grosskreutz, S. Rüping, S. Wrobel, in *Joint European Conference on Machine Learning and Knowledge Discovery in Databases* (Springer, 2008), pp. 440–456.

111. X. Miao, Z. Peng, L. Shi, S. Zhou, Insulating high-entropy ruthenium oxide as a highly efficient oxygen-evolving electrocatalyst in acid. *ACS Catal.* **13**, 3983–3989 (2023).

112. J. Kwon, S. Sun, S. Choi, K. Lee, S. Jo, K. Park, Y. K. Kim, H. B. Park, H. Y. Park, J. H. Jang, H. Han, U. Paik, T. Song, Tailored electronic structure of Ir in high entropy alloy for highly active and durable bifunctional electrocatalyst for water splitting under an acidic environment. *Adv. Mater.* **35**, e2300091 (2023).

113. L. Yao, F. Zhang, S. Yang, H. Zhang, Y. Li, C. Yang, H. Yang, Q. Cheng, Sub-2 nm IrRuNiMoCo high-entropy alloy with iridium-rich medium-entropy oxide shell to boost acidic oxygen evolution. *Adv. Mater.* **36**, e2314049 (2024).

114. S. Jo, M. C. Kim, K. B. Lee, H. Choi, L. Zhang, J. I. Sohn, Nonprecious high-entropy chalcogenide glasses-based electrocatalysts for efficient and stable acidic oxygen evolution reaction in proton exchange membrane water electrolysis. *Adv. Energy Mater.* **13**, 2301420 (2023).

115. S.-Q. Chang, C.-C. Cheng, P.-Y. Cheng, C.-L. Huang, S.-Y. Lu, Pulse electrodeposited FeCoNiMnW high entropy alloys as efficient and stable bifunctional electrocatalysts for acidic water splitting. *Chem. Eng. J.* **446**, 137452 (2022).

116. D. Zhang, Y. Shi, X. Chen, J. Lai, B. Huang, L. Wang, High-entropy alloy metallene for highly efficient overall water splitting in acidic media. *Chin. J. Catal.* **45**, 174–183 (2023).

117. Y. Yu, H. Li, J. Liu, W. Xu, D. Zhang, J. Xiong, B. Li, A. O. Omelchuk, J. Lai, L. Wang, High entropy stabilizing lattice oxygen participation of Ru- based oxides in acidic water oxidation. *J. Mater. Chem. A* **10**, 21260–21265 (2022).

118. A. L. Maulana, P. C. Chen, Z. Shi, Y. Yang, C. Lizandara-Pueyo, F. Seeler, H. D. Abruna, D. Muller, K. Schierle-Arndt, P. Yang, Understanding the structural evolution of IrFeCoNiCu high-entropy alloy nanoparticles under the acidic oxygen evolution reaction. *Nano Lett.* **23**, 6637–6644 (2023).

119. J. Ni, Z. Shi, Y. Wang, J. Yang, H. Wu, P. Wang, K. Li, M. Xiao, C. Liu, W. Xing, Suppressing the lattice oxygen diffusion via high-entropy oxide construction towards stabilized acidic water oxidation. *Nano Res.* **17**, 1107–1113 (2024).

120. Z. Jin, J. Lv, H. Jia, W. Liu, H. Li, Z. Chen, X. Lin, G. Xie, X. Liu, S. Sun, H. J. Qiu, Nanoporous Al-Ni-Co-Ir-Mo high-entropy alloy for record-high water splitting activity in acidic environments. *Small* **15**, e1904180 (2019).

121. P. Keller, H.-H. Strehblow, XPS investigations of electrochemically formed passive layers on Fe/Cr-alloys in 0.5 M H_2SO_4. *Corros. Sci.* **46**, 1939–1952 (2004).

122. H. Su, M. A. Soldatov, V. Roldugin, Q. Liu, Platinum single-atom catalyst with self-adjustable valence state for large-current-density acidic water oxidation. *eScience* **2**, 102–109 (2022).

123. R. Ding, Y. Chen, Z. Rui, K. Hua, Y. Wu, X. Li, X. Duan, X. Wang, J. Li, J. Liu, Guiding the optimization of membrane electrode assembly in a proton exchange membrane water electrolyzer by machine learning modeling and black-box interpretation. *ACS Sustain. Chem. Eng.* **10**, 4561–4578 (2022).

124. A. Tan, Y. Zhang, X. Shi, C. Ju, P. Liu, T. Yang, J. Liu, The poisoning effects of Ti-ion from porous transport layers on the membrane electrode assembly of proton exchange membrane water electrolyzers. *Chem. Eng. J.* **471**, 144624 (2023).

125. C.-A. Tao, J.-F. Wang, Synthesis of metal organic frameworks by ball-milling. *Crystals* **11**, 15 (2021).

126. Y. Ye, H. Chen, Y. Ye, H. Zhang, J. Xu, L. Wang, L. Mo, Silica-supported copper (II) oxide cluster via ball milling method for catalytic combustion of ethyl acetate. *Catalysts* **12**, 497 (2022).

127. T. B. Ferriday, S. Nuggehalli Sampathkumar, P. H. Middleton, J. Van Herle, M. L. Kolhe, How acid washing nickel foam substrates improves the efficiency of the alkaline hydrogen evolution reaction. *Energies* **16**, 2083 (2023).

128. P. M. Bacirhonde, N. Y. Dzade, C. Chalony, J. Park, E.-S. Jeong, E. O. Afranie, S. Lee, C. S. Kim, D.-H. Kim, C. H. Park, Reduction of transition-metal columbite-tantalite as a highly efficient electrocatalyst for water splitting. *ACS Appl. Mater. Interfaces* **14**, 15090–15102 (2022).

129. B. Huang, H. Xu, N. Jiang, M. Wang, J. Huang, L. Guan, Tensile-strained RuO_2 loaded on antimony-tin oxide by fast quenching for proton-exchange membrane water electrolyzer. *Adv. Sci.* **9**, e2201654 (2022).

130. T. Niyitanga, H. Kim, Hematite-nickel oxide/carbon nanotube composite catalyst for oxygen evolution reaction. *Mater. Chem. Phys.* **275**, 125266 (2022).

131. W. Zhu, X. Song, F. Liao, H. Huang, Q. Shao, K. Feng, Y. Zhou, M. Ma, J. Wu, H. Yang, H. Yang, M. Wang, J. Shi, J. Zhong, T. Cheng, M. Shao, Y. Liu, Z. Kang, Stable and oxidative charged Ru enhance the acidic oxygen evolution reaction activity in two-dimensional ruthenium-iridium oxide. *Nat. Commun.* **14**, 5365 (2023).

132. X. Wu, C. Lin, W. Hu, C. Fu, L. Tan, H. Wang, F. Meharban, X. Pan, P. Fu, H. D. Um, Q. Xiao, X. Li, M. Yamauchi, W. Luo, Pluralistic electronic structure modulation of ruthenium oxide for enhanced acidic water electrolysis. *Small Struct.* **5**, 2300518 (2024).

133. Y. Wu, T. Xia, L. Yang, F. Guo, W. Jiang, J. Lang, Y. Ma, J. Feng, G. Che, C. Liu, Construction of an oxygen vacancy-enriched triple perovskite oxide electrocatalyst for efficient and stable oxygen evolution in acidic media. *Inorg. Chem. Front.* **11**, 6387–6395 (2024).

134. D. Zhang, M. Li, X. Yong, H. Song, G. I. N. Waterhouse, Y. Yi, B. Xue, D. Zhang, B. Liu, S. Lu, Construction of Zn-doped RuO2 nanowires for efficient and stable water oxidation in acidic media. *Nat. Commun.* **14**, 2517 (2023).

135. B. Huang, Y. Cui, X. Liu, C. Zheng, H. Wang, L. Guan, Dense-packed RuO_2 nanorods with in situ generated metal vacancies loaded on SnO_2 nanocubes for proton exchange membrane water electrolyzer with ultra-low noble metal loading. *Small* **19**, e2301516 (2023).

136. X. Wang, X. Wan, X. Qin, C. Chen, X. Qian, Y. Guo, Q. Xu, W.-B. Cai, H. Yang, K. Jiang, Electronic structure modulation of RuO_2 by TiO_2 enriched with oxygen vacancies to boost acidic O_2 evolution. *ACS Catal.* **12**, 9437–9445 (2022).

137. Y. Wang, X. Lei, B. Zhang, B. Bai, P. Das, T. Azam, J. Xiao, Z. S. Wu, Breaking the Ru−O−Ru symmetry of a RuO_2 catalyst for sustainable acidic water oxidation. *Angew. Chem.* **136**, e202316903 (2024).

138. H. Jin, X. Liu, P. An, C. Tang, H. Yu, Q. Zhang, H.-J. Peng, L. Gu, Y. Zheng, T. Song, K. Davey, U. Paik, J. Dong, S. Z. Qiao, Dynamic rhenium dopant boosts ruthenium oxide for durable oxygen evolution. *Nat. Commun.* **14**, 354 (2023).

139. X. Wu, W. Han, S. Hao, Y. He, L. Lei, X. Zhang, Synergistically optimizing the electrocatalytic performance of IrO 2 with double doping and bi-directional strains for acidic oxygen evolution reaction. *Cat. Sci. Technol.* **14**, 4599–4607 (2024).

140. D. Chen, R. Yu, K. Yu, R. Lu, H. Zhao, J. Jiao, Y. Yao, J. Zhu, J. Wu, S. Mu, Bicontinuous RuO_2 nanoreactors for acidic water oxidation. *Nat. Commun.* **15**, 3928 (2024).

141. B. An, X. Li, Y. Lin, F. Shang, H. He, H. Cai, X. Zeng, W. Wang, S. Yang, B. Wang, Strontium doping RuO2 electrocatalyst with abundant oxygen vacancies for boosting OER performance. *Inorganic Chem Front* 11, 8935–8944 (2024),.

142. H. Liu, Z. Zhang, J. Fang, M. Li, M. G. Sendeku, X. Wang, H. Wu, Y. Li, J. Ge, Z. Zhuang, D. Zhou, Y. Kuang, X. Sun, Eliminating over-oxidation of ruthenium oxides by niobium for

highly stable electrocatalytic oxygen evolution in acidic media. *Aust. Dent. J.* **7**, 558–573 (2023).

143. H. Huang, H. Kim, A. Lee, S. Kim, W.-G. Lim, C.-Y. Park, S. Kim, S.-K. Kim, J. Lee, Structure engineering defective and mass transfer-enhanced RuO_2 nanosheets for proton exchange membrane water electrolyzer. *Nano Energy* **88**, 106276 (2021).

144. H. Lv, S. Wang, J. Li, C. Shao, W. Zhou, X. Shen, M. Xue, C. Zhang, Self-assembled RuO_2@ IrOx core-shell nanocomposite as high efficient anode catalyst for PEM water electrolyzer. *Appl. Surf. Sci.* **514**, 145943 (2020).

145. G. Zhao, W. Guo, M. Shan, Y. Fang, G. Wang, M. Gao, Y. Liu, H. Pan, W. Sun, Metallic Ru-Ru interaction in ruthenium oxide enabling durable proton exchange membrane water electrolysis. *Adv. Mater.* **36**, e2404213 (2024).

146. Y. Liu, M. Zhang, C. Zhang, H. Zhang, H. Wang, An IrRuO x catalyst supported by oxygen-vacant Ta oxide for the oxygen evolution reaction and proton exchange membrane water electrolysis. *Nanoscale* **16**, 9382–9391 (2024).

147. Y. Dong, Y. Li, Y. Lin, A. Chen, M. Deng, L. Zhang, Z. Tian, L. Chen, Atomically dispersed Ru doped on IrO x sub-nanoclusters for enhanced oxygen evolution reaction in acidic media. *J. Mater. Chem. A* **12**, 21905–21911 (2024).

148. F. Ospina-Acevedo, L. A. Albiter, K. O. Bailey, J. F. Godínez-Salomón, C. P. Rhodes, P. B. Balbuena, Catalytic Activity and Electrochemical Stability of Ru_{1-x} M_x O_2 (M= Zr, Nb, Ta): Computational and experimental study of the oxygen evolution reaction. *ACS Appl. Mater. Interfaces* **16**, 16373–16398 (2024).

149. W. Ren, K. Wang, D. Lu, C. Xu, High-stability RuO_2/MoO_3 electrocatalyst for the oxygen evolution reaction in proton-exchange-membrane water Electrolysis. *ACS Appl. Energy Mater* **6**, 12573–12578 (2023).

150. D. Galyamin, J. Torrero, I. Rodríguez, M. J. Kolb, P. Ferrer, L. Pascual, M. A. Salam, D. Gianolio, V. Celorrio, M. Mokhtar, D. Garcia Sanchez, A. S. Gago, K. A. Friedrich, M. A.

Peña, J. A. Alonso, F. Calle-Vallejo, M. Retuerto, S. Rojas, Active and durable R_2MnRuO_7 pyrochlores with low Ru content for acidic oxygen evolution. *Nat. Commun.* **14**, 2010 (2023).

151. J. Wang, Y. Zhang, Y. Wang, J. Cho, T.-S. Chan, Y. Ha, S.-C. Haw, C.-W. Kao, Z. Wang, J. Lei, M. Ju, J. Tang, T. Liu, S. Zhao, Y. Dai, A. Baron-Wiechec, F. R. Chen, W. Wang, C. H. Choi, Z. Shao, M. Ni, Heterostructure boosts a noble-metal-free oxygen-evolving electrocatalyst in acid. *Energy Environ. Sci.* **17**, 5972–5983 (2024).

152. J. Y. Lim, G. Rahman, S. Y. Chae, K. Y. Lee, C. S. Kim, O. S. Joo, Highly stable RuO_2/SnO_2 nanocomposites as anode electrocatalysts in a PEM water electrolysis cell. *Int. J. Energy Res.* **38**, 875–883 (2014).

153. S. Kong, A. Li, J. Long, K. Adachi, D. Hashizume, Q. Jiang, K. Fushimi, H. Ooka, J. Xiao, R. Nakamura, Acid-stable manganese oxides for proton exchange membrane water electrolysis. *Nat. Catal.* **7**, 252–261 (2024).

154. J. S. Yoo, X. Rong, Y. Liu, A. M. Kolpak, Role of lattice oxygen participation in understanding trends in the oxygen evolution reaction on perovskites. *ACS Catal.* **8**, 4628–4636 (2018).

155. R. Ding, Y. Chen, P. Chen, R. Wang, J. Wang, Y. Ding, W. Yin, Y. Liu, J. Li, J. Liu, Machine learning-guided discovery of underlying decisive factors and new mechanisms for the design of nonprecious metal electrocatalysts. *ACS Catal.* **11**, 9798–9808 (2021).